

Disordered Binary Granular Packings in Three Dimensions

Inaugural-Dissertation

zur Erlangung des Doktorgrades
der Mathematisch-Naturwissenschaftlichen Fakultät der
Heinrich-Heine-Universität Düsseldorf

vorgelegt von

Stefan Frank-Richter

aus Datteln

Düsseldorf, Mai 2014

aus dem Institut für Theoretische Physik II: Weiche Materie der Heinrich-Heine-Universität Düsseldorf

Gedruckt mit der Genehmigung der
Mathematisch-Naturwissenschaftlichen Fakultät der
Heinrich-Heine-Universität Düsseldorf

Referent: Professor Doktor Stefan Egelhaaf
Koreferent: Professor Doktor Jürgen Horbach

Tag der mündlichen Prüfung:

Abstract

In this thesis, the mechanical and structural properties of disordered binary granular packings in three dimensions are investigated. Experiments and the associated data analysis techniques are developed and used to extract the essential information from these granular systems.

X-ray tomography is used to monitor granular packings of glass spheres and an image processing algorithm is developed and used to extract the individual particle positions. The pair correlation function $g(r)$ is calculated for these restricted binary mixtures of glass spheres for asymmetrical and weakly asymmetrical mixtures. For all size ratios three clearly distinguishable peaks are observed. The heights and the positions of the peaks depend strongly on the size and mixing ratio of the investigated systems. Furthermore an indication of rattlers is observed by applying the pair correlation function to a compressed granular system. A cartridge for an X-ray radiography device is developed and used in a parabolic flight. In this experiment, monodisperse packings of glass spheres are investigated under microgravity and a novel regime of cooling is observed.

Granular stress-birefringence is developed for three dimensions. A production method is developed for producing stress birefringent spheres. The transition density from a loose to a dense granular packing, the bulk modulus and the inner development of stresses are obtained from the data. For packings with strongly asymmetric packings a jump/peak in the system properties like transition density and bulk modulus is observed. For weakly asymmetric packings no pronounced jump/peak appears in the system properties. In addition, rattlers in a three dimensional monodisperse granular system consisting of stress birefringent particles are observed in a microgravity environment.

Sound transmission in binary granular packings of glass spheres is investigated. A significant increase of the speed of sound is observed for binary mixtures of glass spheres with strongly asymmetric size ratios. The data for weakly asymmetric packings show no pronounced behavior.

Zusammenfassung

In dieser Arbeit werden die mechanischen und strukturellen Eigenschaften von dichten binären ungeordneten Granulatpackungen in drei Dimensionen untersucht. Auswertelgorithmen werden entwickelt und angewendet.

Mit Hilfe der Röntgentomographie werden granulare Packungen rekonstruiert und die Positionen der Teilchen in dem System bestimmt. Sowohl für stark als auch für schwach asymmetrische binäre granulare Packungen werden die strukturellen Eigenschaften mittels der Paarverteilungsfunktion $g(r)$ untersucht. Hier kann gezeigt werden, dass die Paarverteilungsfunktion für binäre granulare Packungen drei Peaks aufweist, die in ihrer Höhe und in ihrem Abstand zueinander stark von den Größen- und Mischungsverhältnissen der untersuchten Packung abhängen. Des Weiteren können Rattler mit Hilfe der Paarverteilungsfunktion identifiziert werden. Ein Einschub für eine Röntgenquelle wird entwickelt und unter Mikrogravitation in einem Parabelflug eingesetzt. In diesem Experiment wird das granulare Kühlen untersucht und es kann ein neuartiges Gebiet bei langsamer Kühlung nachgewiesen werden.

Granulare Spannungsdoppelbrechung wird zur Bestimmung der inneren und äußeren Spannungszustände in einem binären dreidimensionalen granularen System entwickelt. Hierfür werden spannungsdoppelbrechende Kugeln hergestellt, die im Experiment die jeweiligen Spannungszustände wiedergeben. Außerdem ist es mit diesem Experiment möglich, die Übergangsdichte von einer losen zu einer dichten granularen Packung zu bestimmen. In den gemessenen Daten für stark asymmetrische Mischungen kann ein Sprung in den Packungseigenschaften, wie z.B. der Dichte und den inneren Spannungen des Systems, nachgewiesen werden. Diese Technik wird ebenfalls unter Mikrogravitationsbedingungen eingesetzt und es können Rattler im granularen System nachgewiesen werden.

In einem weiteren Experiment wird die Schallgeschwindigkeit in binären granularen Systemen untersucht. In diesem Experiment kann eine deutliche Erhöhung der Schallgeschwindigkeit in den granularen Systemen für stark asymmetrische binäre Mischungen nachgewiesen werden.

Contents

1	Introduction	1
1.1	Granular Matter	1
1.2	Random-Close Packing	2
1.3	Binary Mixtures	4
2	X-ray Tomography and Radiography	6
2.1	Experimental Setup	6
2.1.1	Sample Cell	6
2.1.2	Sample	7
2.1.3	Mixing Procedure	8
2.2	X-ray Tomography	11
2.3	Reconstruction Method	13
2.3.1	Transmission Absorption Image	13
2.3.2	3D Reconstruction	14
2.3.3	Slice Images	16
2.4	3D Position Detection	16
2.5	Determine the Deviation of the Mixing Ratio \hat{x}_B over the Sample Height	18
2.6	Density Consistency Check for φ_{rcp} Packings	19
2.7	Pair Correlation Function $g(r)$	21
2.8	Analysis of the Pair Correlation Function $g(r)$	24
2.9	Rattler Detection via $g(r)$ Calculation	29
2.10	Outlook	30
2.11	Monitoring Three-Dimensional Packings in Microgravity	31
2.11.1	Microgravity	31
2.11.2	X-Ray Radiography	33
3	3D Stress-Birefringence	42
3.1	Theoretical Background and Calibration	42
3.1.1	Stress Birefringent Technique	42
3.1.2	Polariscope	42
3.1.3	Phase Shift $\Delta\phi$ for a Diametrically Loaded Sphere	44

3.1.4	Analytical Calculation and Experiment	49
3.1.5	Stress Optical Calibration	51
3.2	Experimental Concept for the Determination of Mechanical Properties in Bidisperse Granular Packings	54
3.3	Stress Birefringent Materials	54
3.3.1	Particle Production	55
3.3.2	Water Based Production Method	55
3.4	Experimental Setup	61
3.4.1	Operation of Experiment	63
3.4.2	Volume and Intensity Detection	65
3.4.3	Stress-Optical Analysis I	68
3.4.4	Stress-Optical Analysis II	69
3.5	Results	69
3.5.1	Results for Packing Fraction $\varphi_{rcp}(\hat{x}_B)$ Measurements	69
3.5.2	Discussion	73
3.5.3	Results for the Slope η Analysis	73
3.5.4	Results for Bulk Modulus $\kappa(\hat{x}_B)$ Measurements	75
3.5.5	Finite Size Effects	80
3.6	Outlook	82
3.7	Rattler Observation via Rest Acceleration under Microgravity Conditions using Stress Birefringence	83
4	Sound Transmission	85
4.1	Experimental Setup	85
4.1.1	Triaxial Compression Cell	86
4.1.2	Force Loading Mechanism and Pressure Control	88
4.1.3	Measurement Chain	88
4.1.4	Sample and Measurement Preparation	90
4.1.5	Time Of Flight (TOF) Measurement	95
4.2	Sound Transmission Results	97
5	Conclusion	100
6	Summary	105
A	Appendix	107
A.1	Smallest Voids Between Hard Spheres	107
A.2	Working Method for Binarisation and Position Detection of the X-ray Slice Images	108
A.2.1	Program Description nano	108
A.2.2	Program Description dreidposition	110
A.3	Lists of Measurement Results for φ_{rcp} Densities Measured with Stress Birefringent Technique	111

A.4	Lists of Measurement Results for Slope Analysis	113
A.5	Lists of Measurement Results for Bulk Modulus	114
A.6	Lists of Measurement Results for Sound Transmission	116
A.7	Bibliography	117

Chapter 1

Introduction

1.1 Granular Matter

Granular matter can be defined as an agglomeration composed of macroscopic particles where the particle size is large enough to show no thermodynamic motion¹. There are lots of familiar examples for granular matter like sand, powders, grains and boulders which appear in our everyday live. Even the rings of the Saturn can be described as a granular composition. We often don't pay attention to the presence of granular problems such as milling coffee beans to a powder or using an hourglass. But it is remarkable how little such systems are understood. For industrial applications the lack of knowledge about the static and dynamic behavior of granular matter makes it difficult and expensive to deal with this material. For instance mixing two or three different components from a powder reservoir in a pill with a constant concentration, designing a grain silo with the lowest costs or designing a mineral mill.

Another typical granular phenomenon shows up when pouring a pile of sand or grain on a table. During the flow out of the container onto the table the material behaves like a liquid. Hitting the surface it forms a heap and behaves like a solid. These examples show that granular matter has a wide range in length scale and lots of different phenomenological appearances. These arguments indicate the importance and relevance for both scientific research and application.

To gain systematic access to granular systems it is reasonable to distinguish between dense granular packings where static properties dominate the sys-

¹Consider a particle at $T = 300\text{K}$. If you define thermal motion of the particle as negligible when the thermal energy $E_T = \frac{3}{2}k_B T \approx 6.21 * 10^{-21}\text{J}$ is not able to lift the particle higher than $10^{-4} * r$ (r is the radius of the particle), you can define an accumulation of the considered particle as a granular system, when the individual particles have a radius not bigger than $r = \sqrt[4]{\frac{E_T}{\frac{4}{3}\pi r^3 \rho g * 10^{-4}}} \approx 5\mu\text{m}$, with $\rho = 2.5 \frac{\text{g}}{\text{cm}^3}$ for SiO_2 material.

tem and dilute granular systems where dynamical mechanisms dominate the system.

For investigating the dynamics of granular matter it is possible and useful to define analogies to classical liquids or gases such as a granular temperature $T = \frac{3}{2} \langle v^2 \rangle$ with the particle velocity v or a pressure P . For a limited validity it is possible to apply fluid mechanics or kinetic gas equations to describe the dynamics [1]. But one intrinsic property of a granular gas or fluid is dissipation due to inelastic particle-particle collisions which limits the range of application for fluid mechanical or kinetic theories. A granular gas or fluid needs a driving mechanism to constantly inject energy into the system to sustain a steady state (the system is never in a state of thermodynamic equilibrium). Without such a mechanism to excite the grains the energy quickly dissipates and the granular gas or fluid sediments under gravity or forms clusters in microgravity conditions [2]. When the energy is completely lost, a granular gas or liquid comes to rest and behaves like a solid.

1.2 Random-Close Packing

Solid granular systems are called random close packed (rcp) when the particles are on the one hand in a static state with the highest possible packing fraction φ_{rcp} , which is defined by the ratio of volume occupied by particles to the total system volume, and on the other hand have a random position distribution [3]. For well prepared monodisperse particle packings the transition density φ_{rcp} from a loose to a dense system is $\varphi_{rcp} \approx 0.64$. Due to the lack of thermal fluctuations a granular system can stay in metastable states indefinitely and it can remain in that configuration for a long period of time. The two statements above trigger some questions: what does “highest possible packing fraction” for a “random position distribution” mean and what does “well prepared particle packing” mean? To get a universal valid answer it is necessary to well-define the random close packed state of a disordered granular packing. Unfortunately there is no generally accepted definition and computer simulations yield that φ_{rcp} depends on the preparation protocol and varies between $\varphi_{rcp} \approx 0.64$ and $\varphi_{rcp} \approx 0.68$ [4]. A thought experiment further illustrates this packing behavior. When putting monodisperse particles one by one in a container the assembly will create a packing with a long range order such as an fcc-lattice and thereby a packing fraction of $\varphi_{fcc} = \frac{\pi}{3\sqrt{2}} \approx 0.74$. However, when filling all particles together in the container no long-ranged order can be created and the packing fraction will be $\varphi_{rcp} \approx 0.64$. Thus, the reality is somewhere in between and it is not possible to give a definite answer to the question: “What is a random distribution of

particles?” and what is its “highest possible packing fraction”? However, there are some approaches to find a satisfying answer, the loophole for this ill defined problem is to follow a clear and reproducible preparation protocol to get a “well prepared particle packing”. Several experiments, including this thesis, for monodisperse granular assemblies in three dimensions the random close packing transition density φ_{rcp} is found as ≈ 0.64 and the results are stable against small variations in the preparation protocol [5, 6]. Therefore it seems reasonable to investigate random close packing as long as rather “well prepared” preparation protocols are used. However, it is still an open question how to properly define random close packing. As a substitute for a definition the following convention is used in this thesis: random-close packing is that state which is produced by agitating a random assembly of particles until a structure emerges which is mechanically stable against perturbations and able to carry load [4].

This thesis deals with granular static packings which are composed of one or two spherical particles sizes. With three different measurement techniques which all deal with granular material, different packing properties are investigated:

- The first experiment gives a broad overview about density anomalies for different particle size ratios δ (see definition in section 1.3). In particular experiments are performed for $\delta = 0.15$, $\delta = 0.18$, $\delta = 0.28$, $\delta = 0.35$, $\delta = 0.47$, $\delta = 0.55$, $\delta = 0.67$, and $\delta = 0.78$. For packing preparation, glass spheres from the WIWOX GmbH Surface Systems company are used. Furthermore an algorithm is developed and applied to extract center positions for each individual sphere in the packing from X-ray tomography data. The pair correlation function $g(r)$ is calculated for size ratios $\delta = 0.35$, $\delta = 0.55$ and $\delta = 0.7$.

In addition X-ray radiography is used in microgravity for investigating granular cooling.

- The second experiment focuses on measuring the mechanical properties such as the random-close packing (rcp) transition density from a dilute to a dense bidisperse granular system and the inner stress development during compaction of such systems. Packings of strongly and weakly asymmetrical partical sizes are investigated with soft stress-birefringent silicone particles. In particular data are analyzed for size ratios $\delta = 0.18$, $\delta = 0.3$, $\delta = 0.4$ and $\delta = 0.8$.

Stress birefringence is also used in microgravity for detecting rattlers in a monodisperse granular system.

- In the third experiment, sound transmission in granular systems is investigated. Under hydrostatic pressure a sound signal is transmitted through binary mixtures of glass spheres. In this experiment three

different size ratios $\delta = 0.2$, $\delta = 0.3$ and $\delta = 0.5$ have been experimentally performed.

1.3 Binary Mixtures

Systems composed of two different particle sizes are called binary or bidisperse mixtures. For such systems three control parameter are necessary for their description. In this thesis big particle are called A with radius r_A and number of particles n_A and small particle are called B with radius r_B and number of particles n_B . The mixture is then characterized by

- size ratio $\delta = \frac{r_B}{r_A}$. Per definition w.l.o.g. $r_B \leq r_A$.
- volume mixing ratio $\hat{x}_B = \frac{n_B V_B}{n_A V_A + n_B V_B}$.
with $V_A = \frac{4}{3}\pi r_A^3$ and $V_B = \frac{4}{3}\pi r_B^3$.
- packing fraction $\varphi = \frac{n_A V_A + n_B V_B}{V_C}$ with V_C for the container volume.

Binary mixtures seem to influence the properties of granular packings compared to monodisperse systems. For instance, it has been experimentally proven that for binary mixtures in three dimensions a transition density φ_{rcp} can be achieved, which is significantly higher than $\varphi_{rcp} \approx 0.64$ in a monodisperse sample [7]. In this work it is shown that for a granular system with a size ratio $\delta = 0.5$ a maximum of $\varphi_{rcp} \approx 0.66$ is reachable. For $\delta = 0.25$, depending on \hat{x}_B , the maximum increases to a value of $\varphi_{rcp} \approx 0.71$. For both size ratios the measured functions $\varphi_{rcp}(\hat{x}_B)$ start with $\varphi_{rcp}(\hat{x}_B = 0) \approx 0.63$, increases strictly up to a maximum, and then decreases strictly until $\varphi_{rcp}(\hat{x}_B = 1) \approx 0.63$ is reached. These results could be confirmed in the present thesis. This is also what one would naively expect: Mixed granular systems consisting of particles of different sizes can be packed denser than monodisperse samples, since voids between large particles can be filled by smaller particles that fit into the voids (compare Appendix A.1). However, it is also an open question what happens with $\varphi_{rcp}(\hat{x}_B)$ when the small particles in a mixed granular system become bigger than the voids between the big particles. It is an interesting question if the function $\varphi_{rcp}(\hat{x}_B)$ has always the same shape similar to the one described above or if for other size ratios the shape shows a qualitatively different behavior. Furthermore questions arises if other properties of a three dimensional granular packing like the transition behavior from dilute to dense packed granular systems or sound transmission, change with δ and \hat{x}_B .

Experimentally it turns out that the preparation of random close packing in binary granular mixtures is less difficult than in monodisperse systems.

Monodisperse systems tend to crystallize during compression protocols. In bidisperse packings, crystallization is less likely because usually no simple crystal structures such as fcc-lattice are possible. Therefore, slightly bidisperse systems are typically used when investigating random close packing in order to make sure that a disordered state is preserved [8, 9, 10].

Chapter 2

X-ray Tomography and Radiography

2.1 Experimental Setup

The following experiment investigates bidisperse granular packings consisting of glass spheres. To obtain a full 3D position data set for such systems, three steps are necessary:

- sample preparation
- X-ray tomography and 3D reconstruction of the packing
- center point detection of each particle based on the 3D reconstruction data

2.1.1 Sample Cell

A cylindrical plexiglass tube is used as sample cell, because plexiglas has a low coefficient of absorption for X-rays and is therefore almost invisible in the received images. The inner diameter of the tube is 10mm and the outer diameter is 13mm. The plexiglass tube is sealed by polyvinyl chloride (PVC) or aluminum caps (see Fig. 2.1). The caps are also used to fix the sample cell in the three jaw chuck of the X-ray tomograph. The total height of the sample cell is about 50mm with a volume of $\approx 3.93\text{cm}^3$.

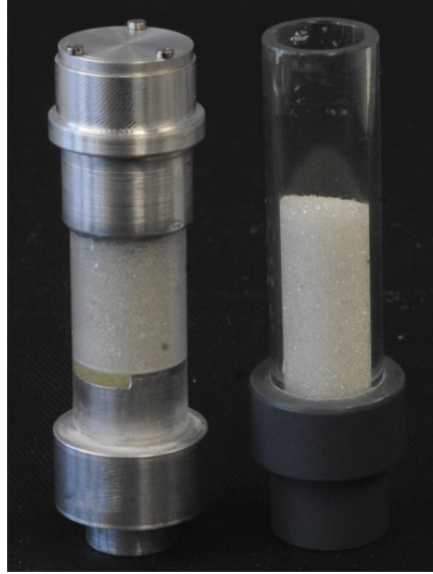


Figure 2.1: Plexiglass tubes with an inner diameter of 10mm and an outer diameter of 13mm. The heights of the sample cells are ≈ 50 mm. Left tube: bottom and top aluminum cap, filled with a binary mixture of glass spheres with size ratio $\delta = 0.55$ ($\varnothing A = 530\mu m$, $\varnothing B = 290\mu m$) and mixing ratio $\hat{x}_B = 0.25$. Right tube: bottom PVC cap and half filled with glass spheres $\varnothing 0.4$ mm (top cap removed).

2.1.2 Sample

The binary mixtures were created by mixing glass spheres which consist of lime-natron glass because of their high coefficient of absorption for X-rays at a wavelength of $\lambda = 10$ nm. Different diameters of the spheres were used, which were obtained via sieving (see Table 2.1).

<i>spheretype</i>	$\varnothing[\mu m]$	$\Delta\varnothing[\mu m]$	$\%_{deviation}$
a	90	± 10	± 11.1
b	112	± 12.5	± 11.2
c	175	± 25	± 14.3
d	218	± 6	± 2.8
e	290	± 10	± 3.4
f	412	± 12.5	± 3
g	530	± 30	± 5.7
h	615	± 15	± 2.4

Table 2.1: Used sizes of glass spheres obtained via sieving.

Table 2.2 shows the size ratios δ which can be mixed from the sphere types listed in Table 2.1.

	a	b	c	d	e	f	g	h
a	1	0.8	0.51	0.41	0.31	0.22	0.17	0.15*
b		1	0.64	0.51	0.39	0.27	0.21	0.18*
c			1	0.8	0.6	0.42	0.33	0.28*
d				1	0.75	0.53	0.41	0.35*
e					1	0.7*	0.55*	0.47*
f						1	0.78*	0.67*
g							1	0.86
h								1

Table 2.2: Possible size ratios δ mixable with the spheres listed in table 2.1. The size ratios δ marked with "*" are the basis for investigation in this experiment. In particular it is $\delta = 0.15$, $\delta = 0.18$, $\delta = 0.28$, $\delta = 0.35$, $\delta = 0.47$, $\delta = 0.55$, $\delta = 0.67$, $\delta = 0.7$ and $\delta = 0.78$.

The size ratios δ marked with "*" in Table 2.2 are used for the setup in this experiment. Specifically $\delta = 0.15$, $\delta = 0.18$, $\delta = 0.28$, $\delta = 0.35$, $\delta = 0.47$, $\delta = 0.55$, $\delta = 0.67$, $\delta = 0.7$ and $\delta = 0.78$ were utilized.

2.1.3 Mixing Procedure

During the mixing procedure it is important to avoid the following three major error sources:

- Care must be taken to ensure that the packing is not crystallizing during the preparation. Especially for $\hat{x}_B \approx 0$ or $\hat{x}_B \approx 1$ this could be the case.
- Separation of the two sphere types needs to be prevented. This is more likely for smaller than for larger size ratios.
- During the filling process it is essential that the mixing ratio \hat{x}_B stays constant over the entire height of the sample cell.

Crystallization can be avoided by protecting the sample cell from violent shocks and severe vibration after filling, so that there is not enough energy for the particles to rearrange their structure.

The separation of components in two or multi component mixtures with low size ratios δ is gravitationally driven [11]. Hence, a mixing procedure via shaking or vibrating is not desired, because a separation of the entire or even part of the sample cell cannot unambiguously be avoided. Furthermore, it is impossible to get a homogeneously mixed sample with a constant mixing ratio over the entire height of the sample cell by simply shaking the sample tube.

To prepare granular binary mixtures under gravitational conditions and to

avoid the error sources described above, a mixing apparatus is developed in order to mix the volume flows of two particle sizes.

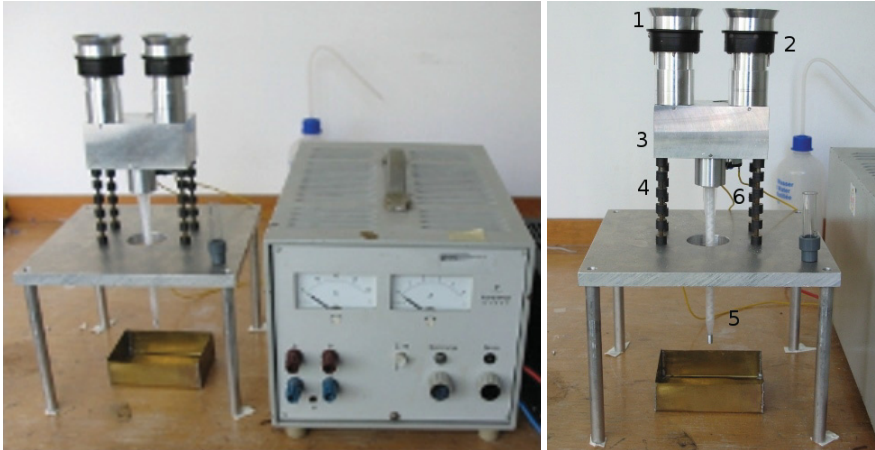


Figure 2.2: Mixing apparatus for binary mixtures under gravitational conditions. Left picture: mixing apparatus with power supply; Right picture: mixing apparatus with (1) filling funnel, (2) aperture with variable opening, (3) mixing hopper, (4) vibration damper, (5) mixing nozzle, (6) vibration motor



Figure 2.3: Mixing nozzle: plastic tube containing an interrupted helical particle rotating device. The tube has a length of $\approx 200\text{mm}$ and a diameter of $\varnothing \approx 6\text{mm}$.

The pictures in Fig. 2.2 show that the mixing apparatus contains two separated filling funnels in which the glass spheres can be filled. At the bottom

of each funnel an aperture is installed, which allows to control the flow rate of the particles via changing the opening diameter of the apertures (these apertures are adapted from camera lenses). The two particle flows are combined in a mixing hopper which has a common outlet. The actual mixing happens in the mixing nozzle (see Fig. 2.3). The mixing nozzle is a plastic tube, which contains an interrupted helical particle rotating device. The incoming particles are mixed in three steps, which are repeated several times

1. The combined particle flow is separated into two volume flows.
2. The separated flows are rotated 180 degrees via an interrupted helical particle rotating device.
3. The two rotated particle flows are then combined again and this procedure is repeated several times.

On exiting the nozzle the mixed particle flow fills into the sample cell. To avoid particle jamming in the filling funnels and/or mixing nozzle, the whole apparatus vibrates during the filling process. The vibration is generated by an eccentric vibration motor (see (6) in Fig. 2.2). The damper (see (4) in Fig. 2.2) ensures that a minimum of vibration can be transmitted to the sample cell during the mixing process to avoid any possible packing influence.



Figure 2.4: Mixing nozzle outlet with the sample cell.

This apparatus allows for producing granular binary mixtures satisfying the boundary conditions described above.

2.2 X-ray Tomography

The raw data for the 3D volume reconstruction of binary mixtures is obtained by using X-ray tomography [12, 13, 14, 15]. The Nanotom 160 NF tomograph from Phoenix X-ray Systems which was in use for the measurements has a voltage range of 0-160 kV and a current range of 0-0.16 μA . This corresponds to a maximal output power of 25.6 Watt. The detector that was used is a digital flat sensor from HAMAMATSU. It consists of 2400 x 2400 pixel with $50 \times 50 \mu m$ per pixel. The path from the X-ray source to the detector is approximately 500mm and the free useable space is 300mm in the beam direction and 130mm perpendicular to the beam direction. In addition, the X-ray tomograph has a 360 degree rotary object stage with a three jaw chuck. The detector has a bit depth of 12-bit and creates with EDR (Extended Dynamic Range) images with a depth of 16-bit.

With the used sample cell it is possible to achieve a resolution of $4.48 \mu m$. Consequently the sample is illuminated at a height of about 11 mm and thus has a volume of about $700 mm^3$. This volume contains a total number of detectable particles from around 3500 (for $615 \mu m$ particles) to around 300000 (for $90 \mu m$ particles) depending on the size ratio δ and the mixing ratio \hat{x}_B . The working principle of the Nanotom is displayed in Fig. 2.5.

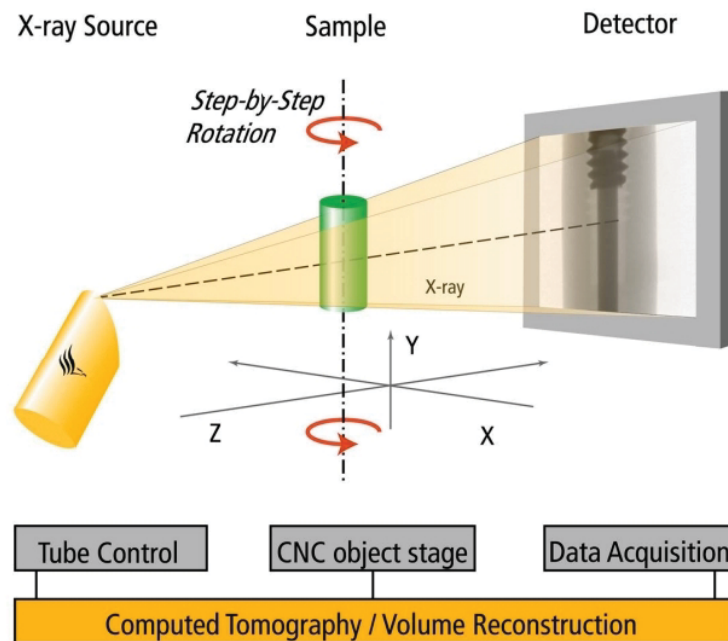


Figure 2.5: Schematic of X-ray tomography: X-ray source (left), divergent beam through the sample cell (middle) and detector (right) (©)phoenix|x-ray Systems GmbH.

The X-ray beam illuminates the sample and a two dimensional transmission absorption image is captured by the detector. The CNC object stage rotates the sample step by step and the images are taken for each step. The Nanotom is a full-protection device and therefore it is not necessary to take any additional precautionary measures. Pictures 2.6 and 2.7 display the set up of the Nanotom.

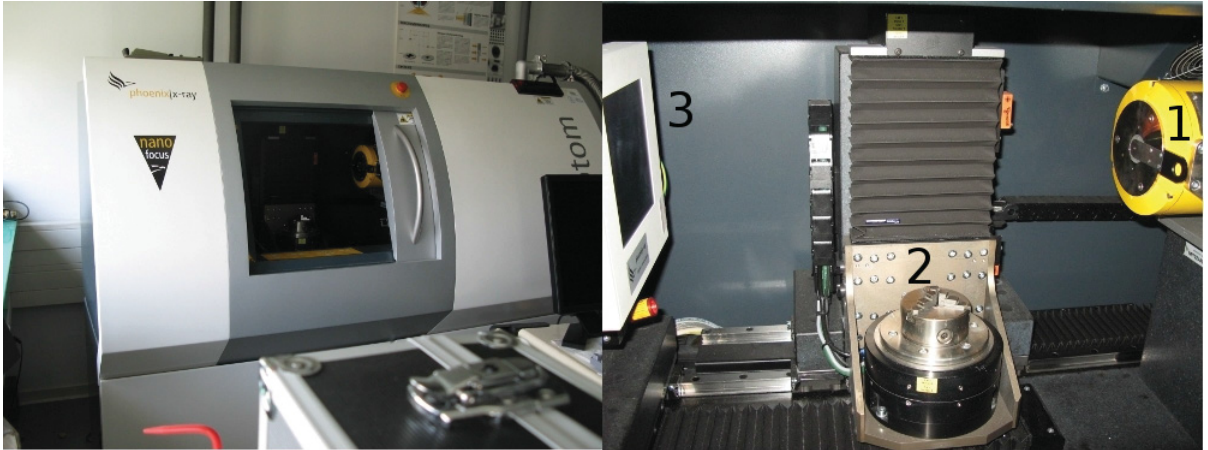


Figure 2.6: X-ray tomography device. Left picture: Nanotom with radiation protection shell. Right picture: inner structure with (1) X-ray source, (2) CNC object stage and (3) detector

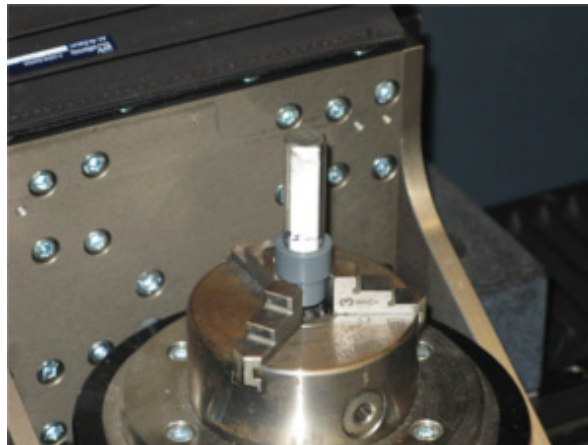


Figure 2.7: CNC rotation table with three jaw chuck and a sample cell filled with glass spheres

2.3 Reconstruction Method

2.3.1 Transmission Absorption Image

To produce optimal projection images with the Nanotom (see Fig. 2.8), it is necessary to adjust the correct ratio between the X-ray source and the absorption profile of the detector depending on the sample in the beam. In the optimization trials of the current experiment the optimal parameter setup had a voltage of 100 kV , a current of 120 μA , and an exposure time of 5000 ms.

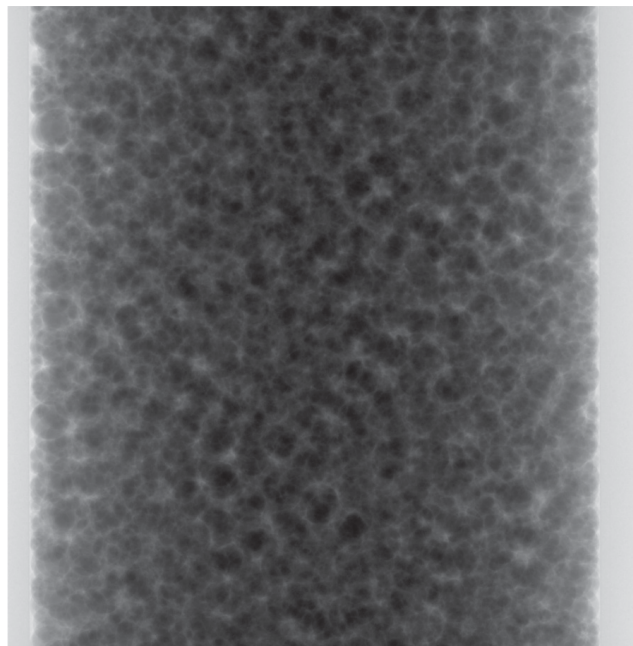


Figure 2.8: Typical absorption image made by the Nanotom. The image shows a granular packing of glass spheres in the sample cell with a size ratio of $\delta = 0.35$ and a mixing ratio of $x_B = 0.72$. The big spheres have a diameter of $\varnothing \approx 615\mu\text{m}$ and the small spheres have a diameter of $\varnothing \approx 218\mu\text{m}$

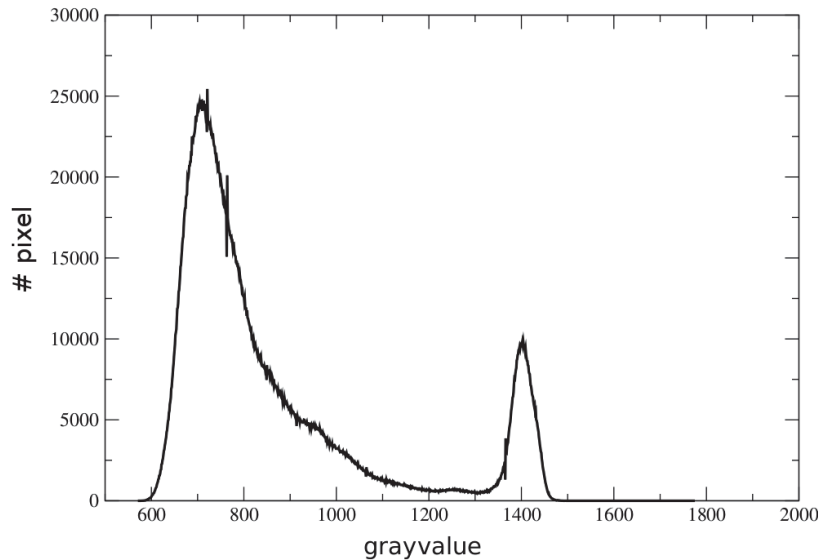


Figure 2.9: Histogram of image 2.8. Energy absorption of the particles is represented by the left peak and absorption of the sample tube is represented by the right peak in the histogram (16-bit depth see text).

Fig. 2.9 illustrates the absorbed beam intensity. It shows that the detected beam intensity is not running out of the detector range during measurement. In the middle of the sample cell the X-ray absorption has its maximum and the corresponding histogram (see Fig. 2.8) has its highest peak with a gray value of ≈ 700 . For more eccentric positions of the cell the absorption is smaller and the histogram reveals higher gray values. The second peak identifies the absorption of the sample tube and has a gray value of 1400. To improve the quality of the projection image and to minimize side effects like afterglow of the detector, it has proven to be helpful to skip the measurements of the first two images at the beginning of each rotation step and to average over three images afterwards. For a full 360° 3D volume reconstruction it is necessary to take 800 images ($0.45^\circ/\text{step}$), which leads to a total measuring time of about 5 hours and 30 minutes.

2.3.2 3D Reconstruction

Based on the projection images described in the previous subsection a 3D reconstruction of the three dimensional volume is generated. Due to the loss of depth information in the projection images, it is necessary to use the 360°

rotation information to reconstruct the sample into a three dimensional image. The mathematical tool that can be used to obtain the three dimensional image is the Radon transformation [16]. The reconstruction process of the images is largely automated and take several corrections like artifacts or a divergent beam line into account. In Fig. 2.10 and 2.11 are representatives of a 3D reconstructed granular binary mixture consisting of glass spheres.

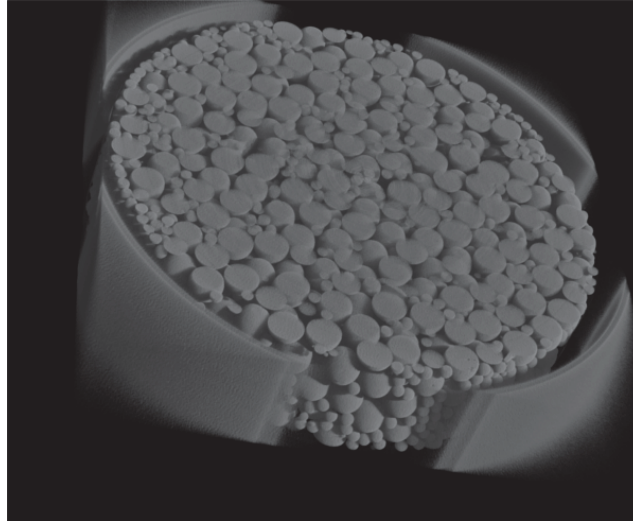


Figure 2.10: Reconstructed 3D image for a sample with a size ratio of $\delta = 0.35$ and a mixing ratio of $x_B = 0.72$. Particle diameters are $\varnothing_A = 615 \pm 15 \mu m$ and $\varnothing_B = 218 \pm 6 \mu m$. The section has a volume of $2150 \text{ px} \times 2150 \text{ px} \times 460 \text{ px} = 2.1 \times 10^9$ data points (voxels).

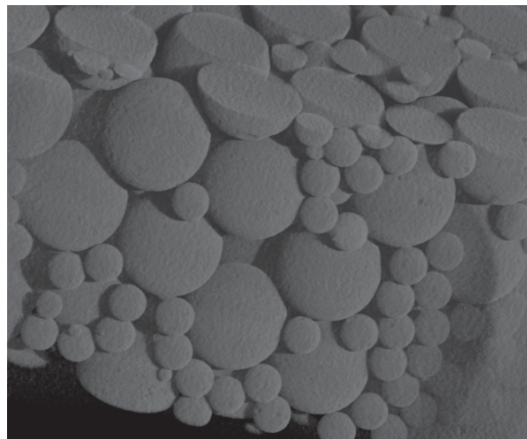


Figure 2.11: Close-up from the 3D image in Fig. 2.10. The big particles have a diameter of $\varnothing_A 137 \text{ px}$ with a volume of 1.3×10^6 voxels. The small particles have a diameter of $\varnothing_B 48 \text{ px}$ with a volume of 0.6×10^6 voxels.

2.3.3 Slice Images

The 3D tomogram is now available and with suitable commercial programs it is possible to separate the volume data in slices with different orientations such as axial, radial or diagonal slices. For further data analysis it is suitable to use radial sliced images. VGStudio Max (Phoenix|X-ray Systems software) was used for slicing the volume data.

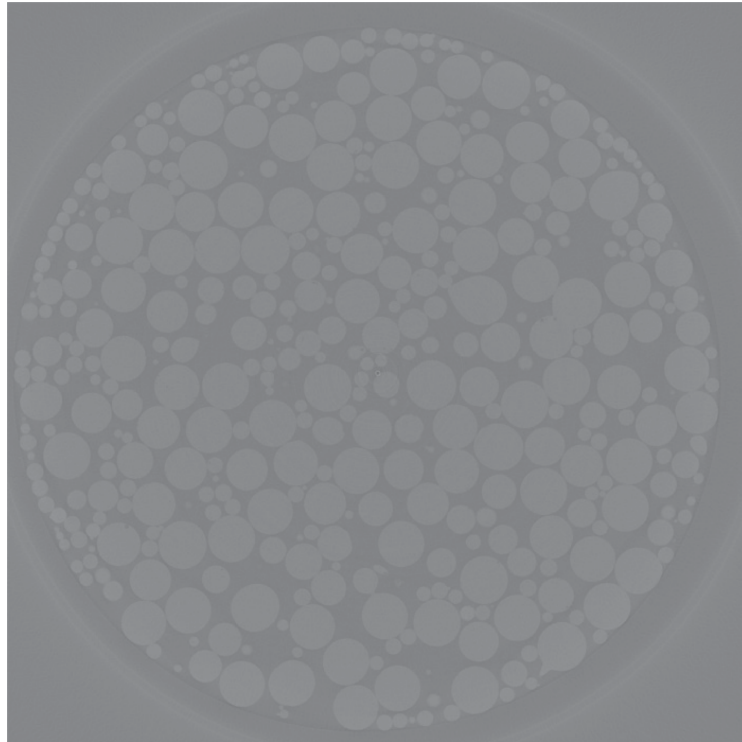


Figure 2.12: Exemplary slice image of Fig. 2.10.

2.4 3D Position Detection

The key to detailed analysis of granular packing is the knowledge about the 3D positions of each particle in the system.

The program described in the following automates the detection of the particle positions and generates a sufficiently precise data set which is suitable to serve as a basis for further structural analysis of granular binary mixtures.

To generate the desired particle positions the raw data are processed in two steps. First the slice images will be binarized and compressed by a program called **nano**. Subsequently, the particles positions are detected using the

program **dreiDposition** (The codes are described in detail in Appendix A.2). All codes are written in IDL. The first step is to generate a histogram, which shows the gray value distribution in the area of the particle location. Therefor a mask is imprinted to the slice image in order to exclude boundary errors such as the sample tube or other artifacts (see Fig. 2.13).

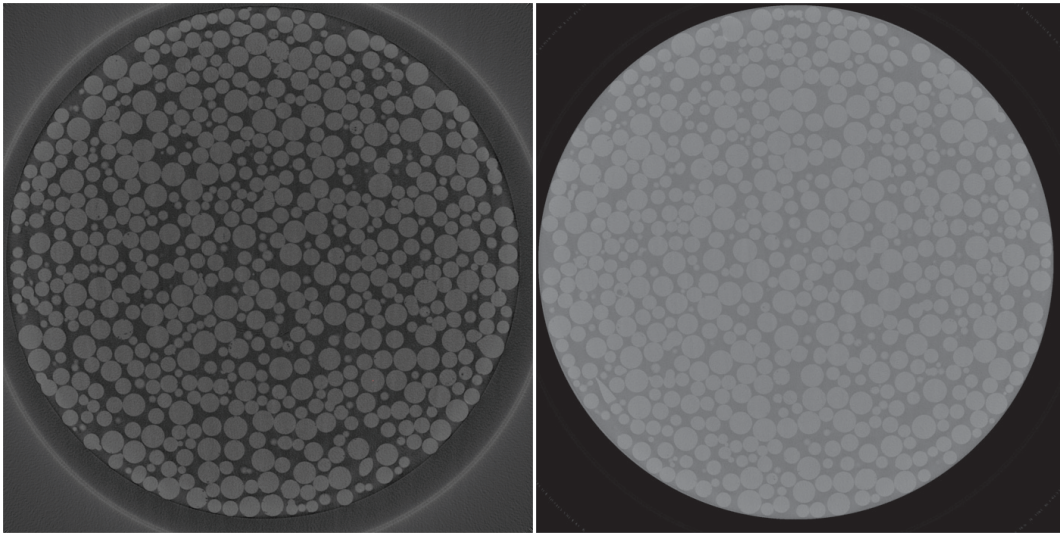


Figure 2.13: Slice images for a binary mixed sample. The image show a granular packing with a size ratio of $\delta = 0.55$ and a mixing ratio of $x_B = 0.54$. Left: original image, Right: image with mask.

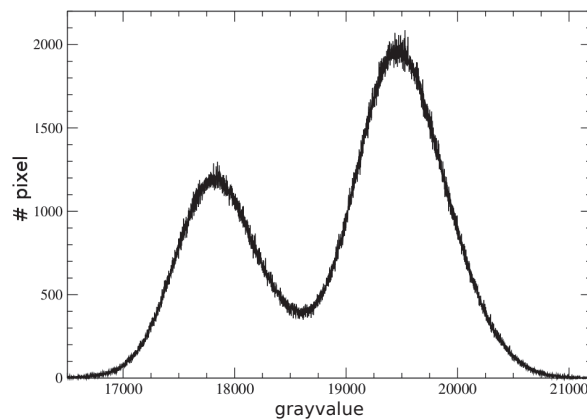


Figure 2.14: Histogram of the slice image with mask in Fig. 2.13

Fig. 2.14 shows the histogram of the slice image with mask in Fig. 2.13. For analysis the computer code **nano** expects a histogram with two peaks

for each image and therefore a minimum between the two maxima. The value of this minimum is the value for the threshold for binarization. After binarization center detection of the particles is processed. The working procedure for the computer codes are described in appendix A.2.

In Fig. 2.15 the compressed image outputted from the computer code `nano` is shown. Fig. 2.16 is the same image as shown in Fig. 2.15 after it has been processed by the computer code `dreidposition`. The detected big particles are outlined in red and the small ones are outlined in green. For every small and big particle 3D space coordinates are determined.

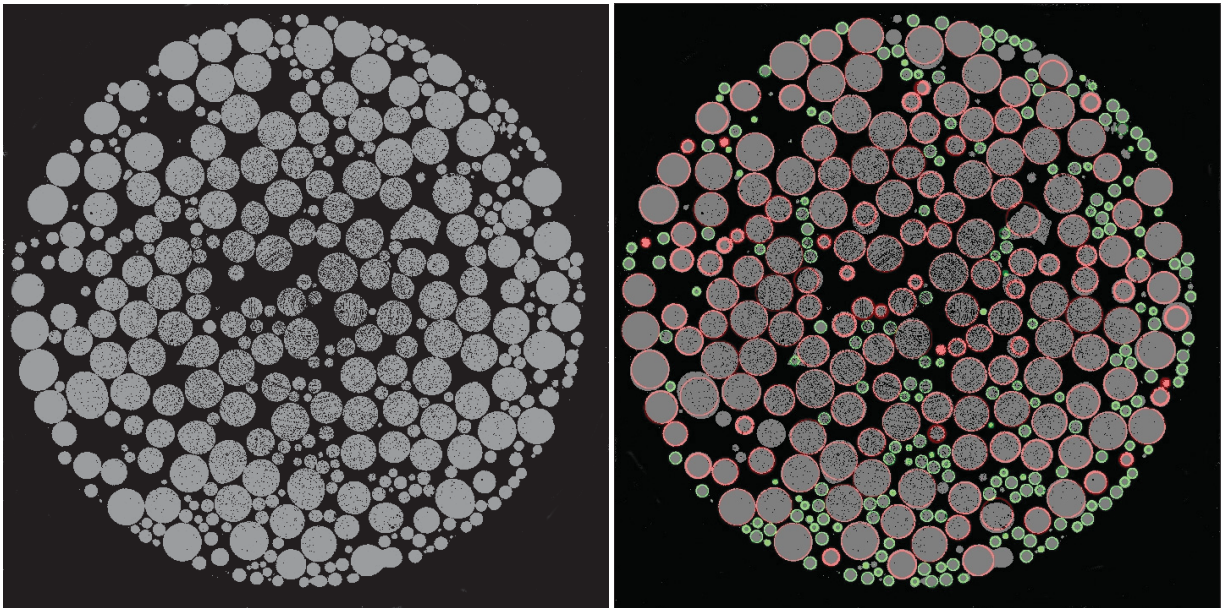



Figure 2.15: Slice picture from a bidisperse sample. Figure 2.16: Same picture as shown in Fig. 2.15 The picture show a packing with a size ratio of $\delta = 0.35$ and a mixing ratio of $\hat{x}_B = 0.72$.
The picture show a packing with a size ratio of $\delta = 0.35$ and a mixing ratio of $\hat{x}_B = 0.72$. The picture shows particle detection. Big particles are outlined in red, small particles are outlined in green. For every small and big particle 3D space coordinates are determined.

2.5 Determine the Deviation of the Mixing Ratio \hat{x}_B over the Sample Height

For determining the deviation of the actual mixing ratio \hat{x}_B over the entire sample height after preparation (compare section 2.1.3) the obtained position data are used. Exemplary one dataset is separated into three sections (see Fig. 2.17 (left)). For every section the mixing ratio $\hat{x}_{B\ 1,2,3}$ is calculated. The results are listed in Fig. 2.17 for a granular packing with size ratio $\delta = 0.35$ and several mixing ratios \hat{x}_B .



\hat{x}_B	\hat{x}_{B_1}	\hat{x}_{B_2}	\hat{x}_{B_3}	deviation _{max}
0.013	0.0123	0.0127	0.0135	≈ 10%
0.022	0.0216	0.022	0.0221	≈ 2%
0.035	0.0362	0.0345	0.0337	≈ 7%
0.049	0.0511	0.0481	0.048	≈ 6%
0.105	0.1039	0.1076	0.1037	≈ 4%

Figure 2.17: Deviation of the actual mixing ratio \hat{x}_B over the entire sample height after preparation for a granular system of glass spheres with a size ratio $\delta = 0.35$ and mixing ratio $\hat{x}_B = 0.013$, $\hat{x}_B = 0.022$, $\hat{x}_B = 0.035$, $\hat{x}_B = 0.049$ and $\hat{x}_B = 0.105$. Left: the separation convention is shown. Right: the results for the determined deviation are listed in the table.

2.6 Density Consistency Check for φ_{rcp} Packings

In order to provide a consistency check and to give a broad overview to the density evolution of bidisperse granular systems, a series of experiments (see Table 2.2) is performed. The used sample cell is the same as described in subsection 2.1.1. The sample tapped softly three times after filling. To calculate the resulting packing density the next step after filling is to separate the two sphere components via sieving and determine their individual weights. With the density of the material (which is $\rho = 2.45$ for lime-natron glass) and the sizes of the spheres it is possible to calculate the number of particles. Now the packing density can be calculated via $\varphi = \frac{\frac{4}{3}\pi r_A^3 n_A + \frac{4}{3}\pi r_B^3 n_B}{V_{samplecell}}$ with r_A, r_B radii of the spheres, n_A, n_B number of particles and $V_{samplecell}$ volume of the sample cell. Fig. 2.18 show the results of these measurements.

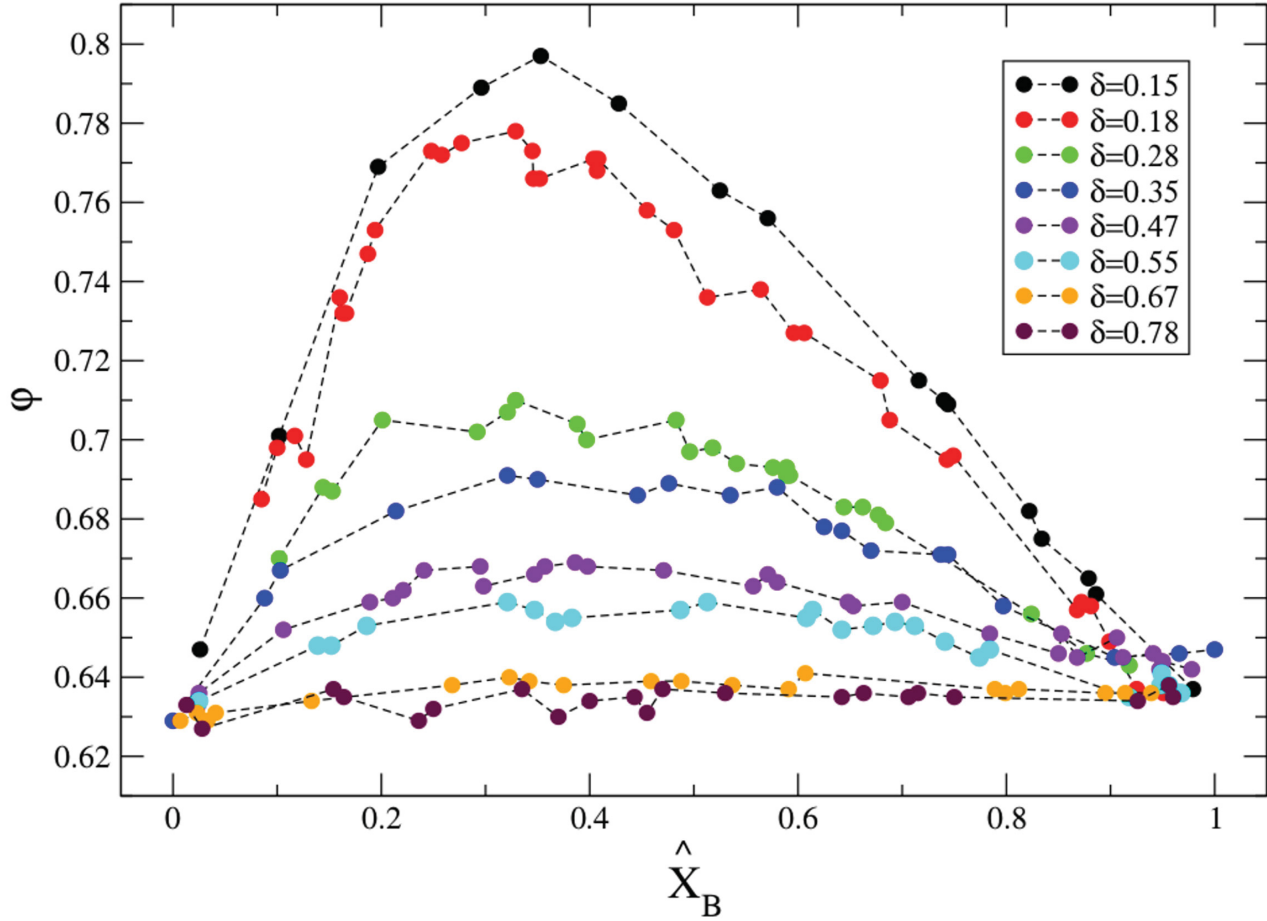


Figure 2.18: Density for bidisperse packings of glass spheres. The curves show the density distribution for binary mixtures with size ratio $\delta = 0.15, \delta = 0.18, \delta = 0.28, \delta = 0.35, \delta = 0.47, \delta = 0.55, \delta = 0.67$ and $\delta = 0.78$.

The majority of the curves in Fig. 2.18 starts with a packing fraction of around 63% at $\hat{x}_B = 0$. This value is slightly lower than an expected value of $\varphi_{rcp} \approx 64\%$ for monodisperse random close packed granular systems. A reasonable explanation for this behaviour is the influence of friction between the particles. Systems with friction can create significantly lower packing fractions as systems without friction [17]. For all measurements the granular systems are consisting of high number of particles. Table 2.3 show an example for measured packing properties including the number of particles for big and small spheres n_A, n_B and the friction coefficient μ_s . For the other measured size ratios shown in Fig. 2.18 the packings consists of comparable statistics.

The curve for $\delta = 0.15$ in Fig. 2.18 shows a clear maximum at $\hat{x}_B = 0.353$ with $\varphi_{rcp} = 0.797$. For increasing size ratios δ the curves flatten until the maxima disappear.

μ_s glass/glass	δ	\hat{x}_B	φ_{rcp}	n_A	n_B
0.9-1	0.15	0.026	0.647	20000	170000
		0.879	0.665	2500	5850000

Table 2.3: Packing properties for the granular system of glass spheres shown in Fig. 2.18 (black dots). The parameter for the system are size ratio $\delta = 0.15$ with particle diameter $\varnothing_A = 615\mu m$ and $\varnothing_B = 90\mu m$. The listed particle numbers for the big spheres n_A and small spheres n_B give an overview about the measured statistics.

2.7 Pair Correlation Function $g(r)$

The inner structure of random close packed systems based on the data obtained from the procedure described in section 2.1 is analysed by using the pair correlation function $g(r)$ [13, 18, 19, 20].

The pair correlation function $g(r)$ indicates how density varies as a function of distance from a reference particle and is defined as:

$$g(r) := \frac{1}{N\varphi} \int_{points} \int_{points} \delta(|\vec{p} - \vec{q}| - r) \frac{1}{4\pi r^2} d\vec{p} d\vec{q} \quad (2.1)$$

for systems with infinity boundary conditions. In equation 2.1 φ stands for the system density, N is the total number of particles, \vec{p} is the position vector of point p which applies also for \vec{q} and q . A pair of \vec{p} and \vec{q} have the distance $|r|$.

To make formula 2.1 applicable for restricted systems it is necessary to discretize the expression:

$$g(r) = \frac{1}{N\phi} \sum_{\vec{p} \in points} \sum_{\vec{q} \in points} \theta((|\vec{p} - \vec{q}| - r) * (r + b - |\vec{p} - \vec{q}|)) \frac{1}{4\pi r^2 b} \quad (2.2)$$

where N is the total number of particles and ϕ is the density of the restricted system. The expression b is known as binning of the calculation and it applies for the calculation radius $|r| = b * n$ with $n \in \mathbb{N}$. The fraction $\frac{1}{4\pi r^2 b}$ is approximately the volume of a hollow sphere with inner radius r and outer radius $r + b$ whereupon the heavysidefunction θ ensure that only pairings of points p and q between r and $r + b$ are possible. The restricted density ϕ is given by:

$$\phi = \frac{N}{(c_{Z1} - c_{Z0})\pi c_R^2} \quad (2.3)$$

where c_R is the radius of a cylinder and c_{Z0} , c_{Z1} are the lower and upper limits (note that c_R is the defined cylinder radius for calculation and not the

cylinder radius of the experiment container). The principle for calculating $g(r)$ in a restricted system is illustrated in Fig. 2.19.

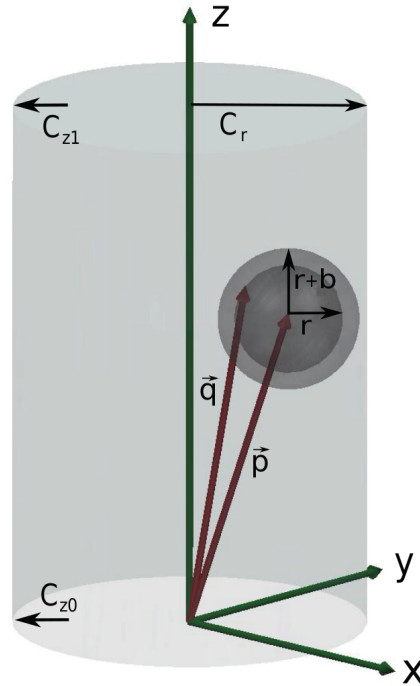


Figure 2.19: Principle of calculating $g(r)$ in a restricted system. Transparent gray is the cylinder which contains the scatter plot (not illuminated). Dark transparent gray is the volume of a hollow sphere with inner radius r and outer radius $r + b$. \vec{p} and \vec{q} are the position vectors of point p and q with distance $|r|$. $|r|$ has to be between the inner radius r and outer radius $r + b$ of the hollow sphere to fulfill the boundary conditions for pairing p and q .

When investigating $g(r)$ in restricted systems it is important that the normalization of $g(r)$ as described in equation 2.2 is only valid when the inner radius of the hollow sphere with its position vector \vec{p} is at least $r + b$ away from the system boundaries. If \vec{p} has a closer distance to the system boundaries it is possible that a pairing between p and q is calculated which is not allowed because q can have a value greater than the system boundaries. Hence the normalization has to be done with partial volumes. In this case the normalization has to be corrected and the sum

$$\sum_{\vec{q} \in \text{Punkte}} \theta((|\vec{p} - \vec{q}| - r) * (r + b - |\vec{p} - \vec{q}|)) \frac{1}{4\pi r^2 b}$$

from equation 2.2 has to be replaced by

$$\sum_{\vec{q} \in \text{Punkte}} \theta((|\vec{p} - \vec{q}| - r) * (r + b - |\vec{p} - \vec{q}|)) \frac{1}{V_P}. \quad (2.4)$$

where $\frac{1}{V_P}$ stands for the corrected normalization. Two cases must be distinguished when calculating $g(r)$ for systems with cylindrical boundary conditions and partial volume normalization: first \vec{p} is close to the area of the surface in radial direction, second \vec{p} is close to the area of the surface in axial direction. To avoid a complicated analytical solution for calculating the partial volume V_P the boundary value problem is simplified. In the first case a wedge is defined in which the scatter plot as well as the partial volume is excluded for calculating $g(r)$. For case two an additional volume has to be excluded. Both cases are shown in Fig. 2.20 and the detailed calculation is described in [21].

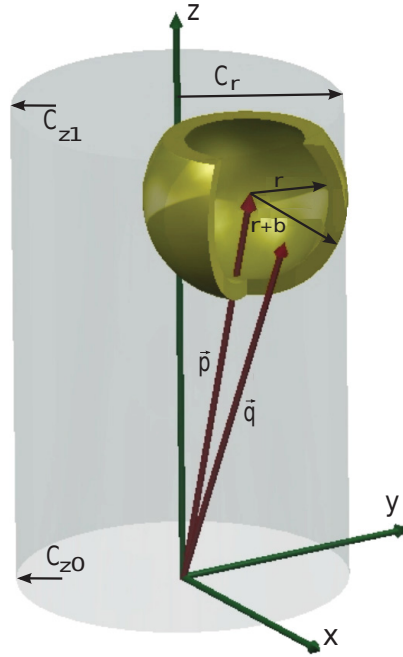


Figure 2.20: Boundary volume correction for $g(r)$ calculation in a restricted granular system. The figure visualizes the idea behind the simplification of the boundary value problem when calculating the pair correlation function $g(r)$ for restricted systems. Transparent gray is the cylinder which contains the scatter plot (not illuminated). Bright yellow is the volume of the hollow sphere with inner radius r and outer radius $r + b$ with excluded calculation volume.

2.8 Analysis of the Pair Correlation Function $g(r)$

In Fig. 2.21 a pair correlation function $g(r)$ is shown which is calculated based on a granular system with size ratio $\delta = 0.35$ and mixing ratio $\hat{x}_B = 0.013$. The pair correlation function is plotted against r/d_A where $|r|$ is the distance between vector \vec{p} and \vec{q} and d_A is the diameter of the big sphere. This means that the distance between two big spheres (hereinafter to be referred to as A-A-distance) is normalized to $r/d_A = 1$.

Three major peaks are distinguishable in the diagram: the first peak (from left to right) appears at $r/d_A = 0.35$ which indicates the distance of two small spheres (hereinafter to be referred to as B-B-distance), the second peak appears at $r/d_A = 0.675$ and indicates the distance between a small and a big sphere (hereinafter to be referred to as A-B-distance) and the third peak is at $r/d_A = 1$ and indicates the A-A-distance as mentioned above. The first peak at $r/d_A = 0.35$ indicates also the size ratio $\delta = 0.35$ which is a consequence of the chosen normalization.

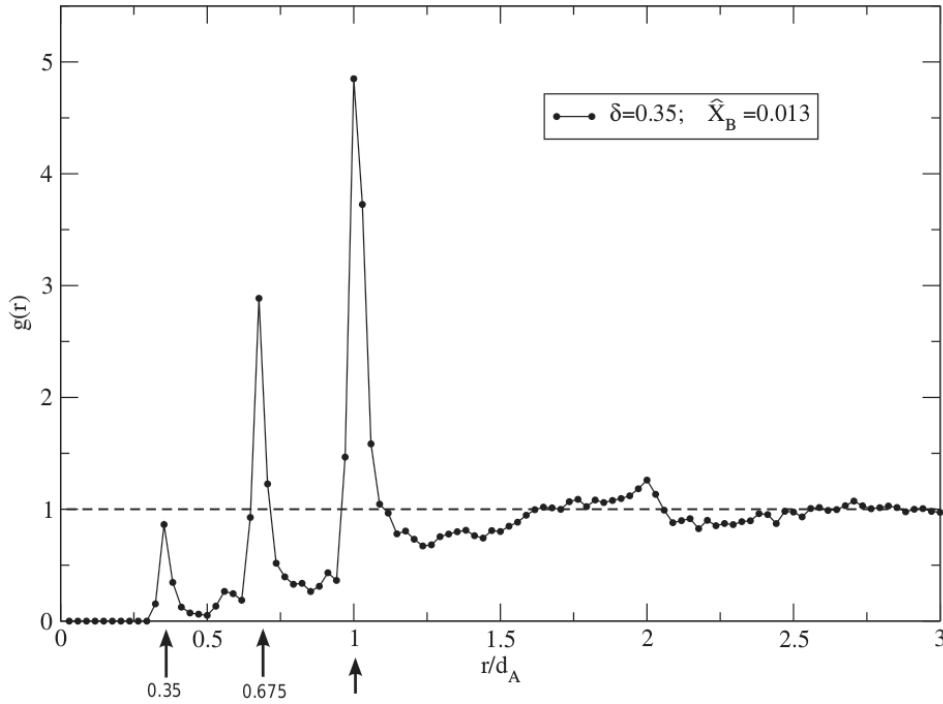


Figure 2.21: Calculated $g(r)$ for a restricted bidisperse granular system of glass spheres with size ratio $\delta = 0.35$ and mixing ratio $\hat{x}_B = 0.013$. The curve shows three major peaks at $r/d_A = 0.35$, $r/d_A = 0.675$ and $r/d_A = 1$ which indicates the possible particle-particle distances between the spheres.

The pair correlation function $g(r)$ can be interpreted as probability distribution function to find a particle at distance $|r|$ from a chosen point p [19]. The probability is consequently zero for hard spheres as long as the relation $|r| < B$ -B-distance is fulfilled. At the first peak $g(r)$ has a value $g(r) < 1$ which is a consequence of the small mixing ratio $\hat{x}_B = 0.013$. This means that the system consist of only a few small particles and hence a low probability for having two small particles in contact. The second peak increases to a value of $g(r) \approx 3$ which indicates a higher probability for A-B particle contacts. The highest peak has a value of $g(r) \approx 5$ which means that A-A particle contacts dominates the structure of these granular system. For higher $r/d_A > 1$ the pair correlation function asymptotically approaches a value of $g(r) = 1$ which means that the probability for large distances $|r|$ is only dependent on the density φ of the system.

The figures 2.22, 2.23 and 2.25 show the $g(r)$ calculation results for granular systems with size ratio $\delta = 0.35$, $\delta = 0.55$ and $\delta = 0.7$ respectively. The binning value is chosen to $b = 4$ in order to smooth the curves. The general structure of the curves are the same as described for Fig. 2.21. The three major peaks appear depending on the sizes of the spheres in the granular packing. The height of the peaks show the probability of a pair correlation between two spheres.

In Fig. 2.22 $g(r)$ is shown for three different mixing ratios \hat{x}_B . The curve for the smallest $\hat{x}_B = 0.013$ (blue line) has a peak at $r/d_A = 0.35$ with a value $g(r) < 1$ which means that the probability is low to find a B-B-contact in the system. The next peak at $r/d_A = 0.675$ increases to a value $g(r) \approx 3$ and hence the probability to find a A-B-contact in the system. The last peak at $r/d_A = 1$ with its value $g(r) \approx 5$ indicates that the system is dominated by A-A particle contacts (it is the same curve as shown in Fig. 2.21). The opposite is shown in the curve for the mixing ratio $\hat{x}_B = 0.105$ (red). There the system is dominated by B-B particle contacts. The calculation result for the intermediate mixing ratio $\hat{x}_B = 0.022$ is visible as dashed black line with stars in the diagram and has the same interpretation as described above. Note that between $\hat{x}_B = 0.013$ (blue line) and $\hat{x}_B = 0.105$ (red line) the volume mixing ratio \hat{x}_B increases only about $\approx 10\%$.

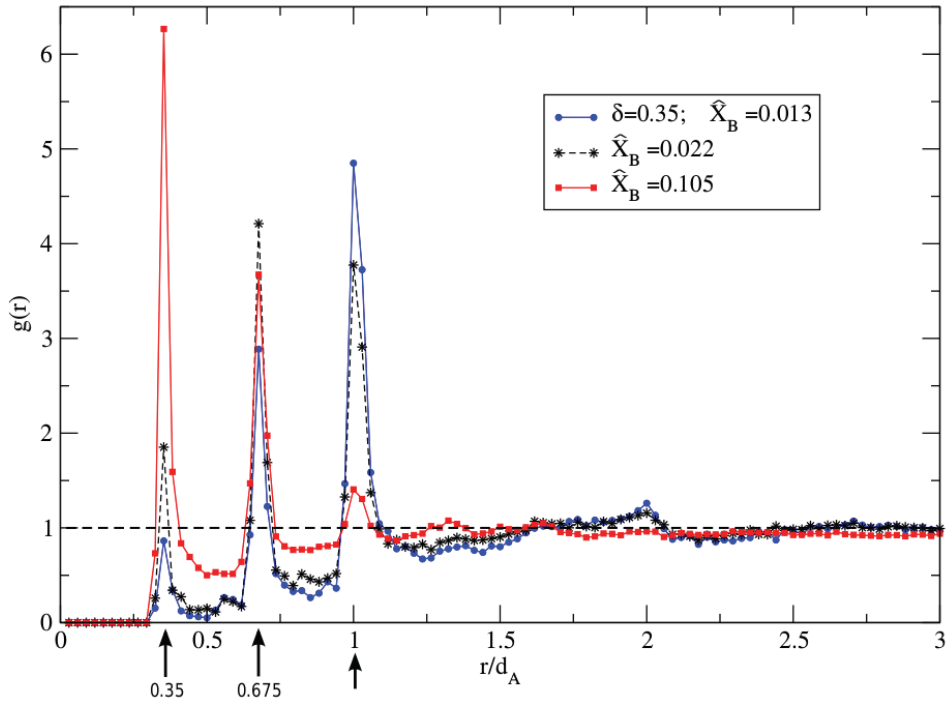


Figure 2.22: Calculated $g(r)$ for a restricted bidisperse granular system of glass spheres with size ratio $\delta = 0.35$ and three different mixing ratios $\hat{x}_B = 0.013$, $\hat{x}_B = 0.022$ and $\hat{x}_B = 0.105$. The curve show three major peaks at $r/d_A = 0.35$, $r/d_A = 0.675$ and $r/d_A = 1$ which indicates the particle-particle distances between the spheres.

In Fig. 2.23 $g(r)$ is shown for size ratio $\delta = 0.55$ and three different mixing ratios. Note that between $\hat{x}_B = 0.04$ (blue line) and $\hat{x}_B = 0.555$ (red line) the volume mixing ratio is about $\approx 50\%$ here. By comparing the diagram for size ratio $\delta = 0.35$ in Fig. 2.22 and $\delta = 0.55$ and in Fig. 2.23 it is mentionable that the $g(r)$ values for comparable mixing ratios show different trends. In Fig. 2.22 the curve for $\hat{x}_B = 0.105$ (red line) indicates a granular system which is dominated by B-B particle contacts. The curve in Fig. 2.23 for $\hat{x}_B = 0.104$ (black dashed line with stars) indicates a different situation for the random distribution of spheres in a granular packing. Here the system is dominated by A-B particle contacts with an also high possibility for A-A contacts. These A-A contacts are almost vanished in the system with size ratio $\delta = 0.35$ at $\hat{x}_B = 0.105$ (red line) shown in Fig. 2.22.

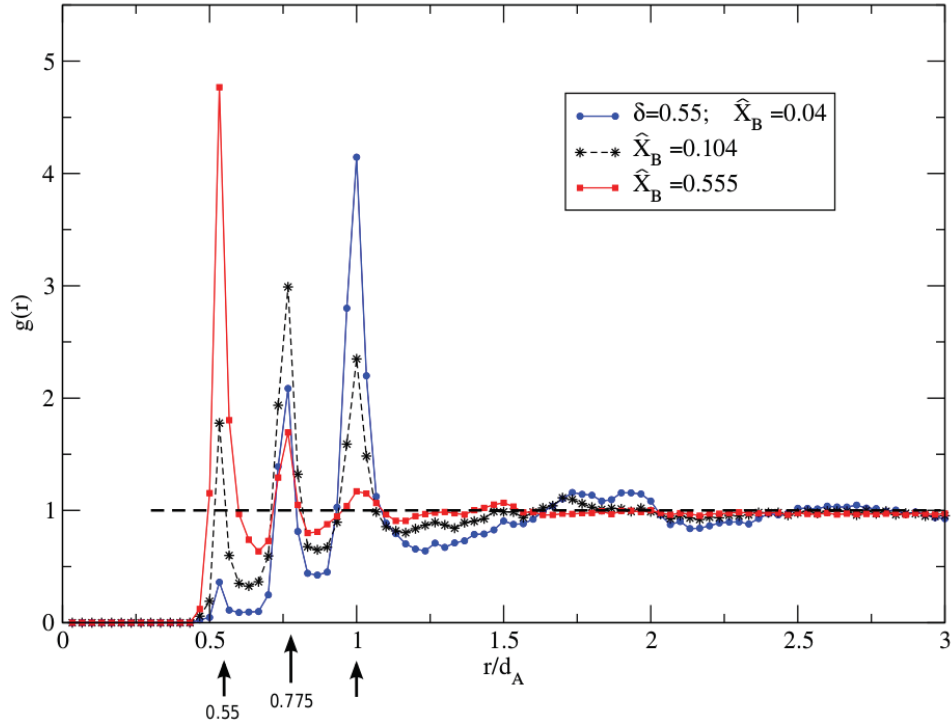


Figure 2.23: Calculated $g(r)$ for a restricted bidisperse granular system of glass spheres with size ratio $\delta = 0.55$ and three different mixing ratio $\hat{x}_B = 0.04$, $\hat{x}_B = 0.104$ and $\hat{x}_B = 0.555$. The curve show three major peaks at $r/d_A = 0.55$, $r/d_A = 0.775$ and $r/d_A = 1$ which indicates the particle-particle distances between the spheres.

Fig. 2.25 show the $g(r)$ results for a granular packing with size ratio $\delta = 0.7$ and three different mixing ratios. Here the interval of \hat{x}_B goes from $\hat{x}_B = 0.056$ to $\hat{x}_B = 0.937$ with a value in between of $\hat{x}_B = 0.636$. The two peaks for $\hat{x}_B = 0.056$ (blue line) and $\hat{x}_B = 0.937$ (red line) show almost the same height for $g(r)$ with a value $g(r) \approx 5.5$. Interesting to mention is that for very small \hat{x}_B 's (blue line) there is still a possibility for B-B particle contacts. In contrast to very large \hat{x}_B 's (red line) where the possibility for A-A and A-B particle contacts is vanished. Which means that in packings with a small mixing ratio (blue line) are still enough small particles to create B-B particle contacts, whereas in packings with large mixing ratios (red line) the big particles are so understaffed that they don't create A-A particle contacts and only a not significant number of A-B particle contacts. The curve with a mixing ratio $\hat{x}_B = 0.636$ is chosen in order to show that in a granular system with size ratio $\delta = 0.7$ the system lose their possibility for A-A contacts which can be seen in the almost vanished $g(r)$ value for A-A particle contacts. Furthermore additional peaks appear in the curves for $\hat{x}_B = 0.056$ (blue line) and $\hat{x}_B = 0.937$ (red line). They indicate the particle distance which are described in Fig. 2.24 [20, 22].

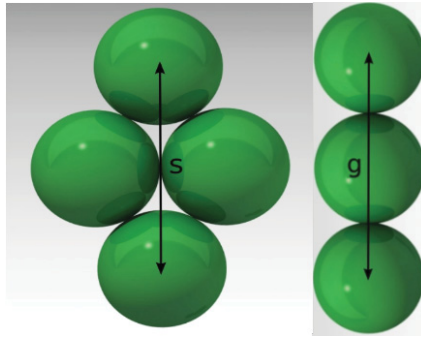


Figure 2.24: Particle arrangement with four spheres of diameter d where distance $s = \sqrt{3}d$ is shown (left). Particle arrangement with three spheres in a row where distance $g = 2d$ is shown (right).

The distance s has the values $s = \sqrt{3}d$ and g is $g = 2d$ where d is the diameter of the sphere. The peaks are marked with s and g in Fig. 2.25. The peaks for s and g distances can also be seen in the results for size ratio $\delta = 0.35$ in Fig. 2.22 ($\hat{x}_B = 0.04$, blue line) and for size ratio $\delta = 0.55$ in Fig. 2.23 ($\hat{x}_B = 0.013$, blue line).

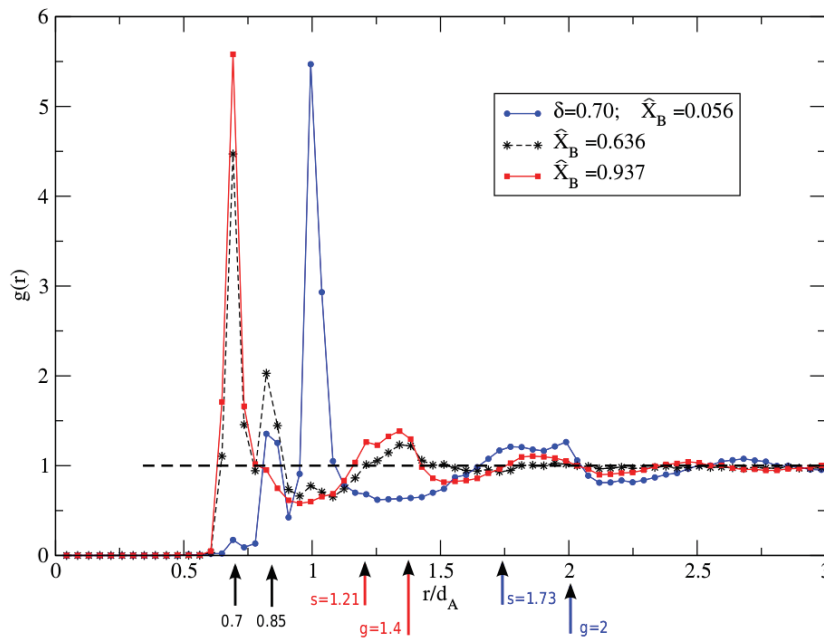


Figure 2.25: Calculated $g(r)$ for a restricted bidisperse granular system of glass spheres with size ratio $\delta = 0.7$ and mixing ratio $\hat{x}_B = 0.056$, $\hat{x}_B = 0.636$ and $\hat{x}_B = 0.937$. The curve show three major peaks at $r/d_A = 0.7$, $r/d_A = 0.85$ and $r/d_A = 1$ which indicates the particle-particle distances between the spheres. Also shown are the distances $s = \sqrt{3}d$ and $g = 2d$ (see Fig. 2.24) for the the mixing ratios $\hat{x}_B = 0.056$ and $\hat{x}_B = 0.937$

2.9 Rattler Detection via $g(r)$ Calculation

Particles in a dense packed granular system which are not fully arrested are called rattlers. An indication of the number of rattlers in such a system can be determined by analyzing the pair correlation function $g(r)$. For measuring these value a granular sample with size ratio $\delta = 0.7$ and mixing ratio $\hat{x}_B = 0.512$ is investigated. Three different preparation protocols have been performed for the same sample:

- preparation 1: A bidisperse granular mixture has been produced with the method described in section 2.1.3. For structural analysis, the particle positions have been determined based on X-ray tomography volume reconstruction data as described in section 2.2. The result is named “untapped” and is shown in Fig. 2.26 (black line).
- preparation 2: The same sample as describe in preparation 1 was processed again after soft tapping on a table. The result is named “tapped” and is shown in Fig. 2.26 (red line).
- preparation 3: The same sample as described in preparation 2 was processed again after hard compressing the packing with a bolt. The result is named “compressed” and is shown in Fig. 2.26 (blue line).

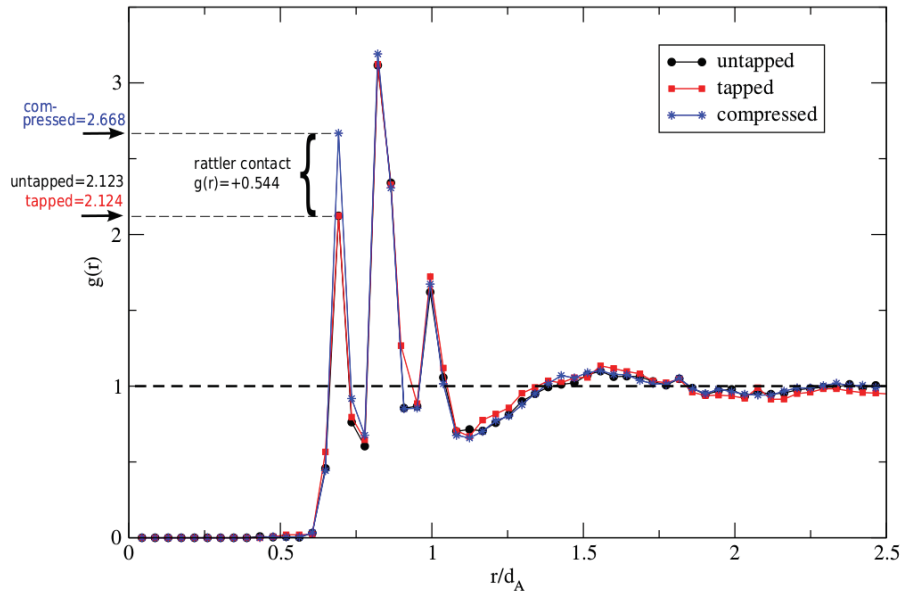


Figure 2.26: $g(r)$ for a bidisperse granular system of spheres with a size ratio $\delta = 0.7$ and a mixing ratio $\hat{x}_B = 0.512$. The three curves show the calculation results for the same sample which was manipulated in three different ways during preparation. The peak at $r/d_A = 0.7$ shows a significant increase in height for the compressed sample which indicates that the rattlers loose their voids in the packing.

The peaks for A-A and B-A particle distances (see Fig. 2.26) are not changing in height for the three different preparation protocols. The first peak at $r/d_A = 0.7$ increases significantly in height from $g(r) \approx 2.12$ for the untapped/tapped sample to $g(r) = 2.67$ for the compressed sample which means $g(r)$ increases about $\approx 25\%$ after compressing. This indicates that the B-B particle contacts increases during compression and it also indicates that predominantly small particles are the rattlers in this granular system.

2.10 Outlook

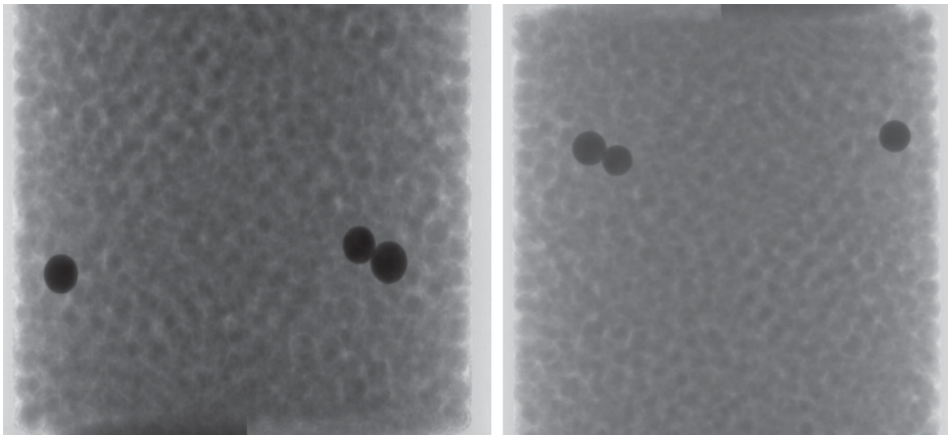


Figure 2.27: Radiography images of the sample cell (see Fig. 2.1 with aluminum caps) for rattler detection before (left) and after (right) rotation. The two images show the same granular packing of glass spheres with a size ratio of $\delta = 0.18$ and a mixing ratio of $\hat{x}_B = 0.056$. The particle sizes are: big spheres $\varnothing_A \approx 615\mu\text{m}$, small spheres $\varnothing_A \approx 112\mu\text{m}$. Visible are also the three tracer particles in both pictures. They consist of metal and have a diameter of $\varnothing_{\text{trace}} \approx 900\mu\text{m}$.

For further rattler investigations a new detection technique is developed, but needs to be analysed. In the new method two position data sets have to be available for each mixing ratio: the first data set is obtained after preparing the granular packing with the same experimental protocol as described in section 2.1. The second data set is obtained after the X-ray tomography for the first data set was produced. For the second tomography the sample cell needs to be rotated by 180° around an axis through the cylinder surface (see sample cell in Fig. 2.1 with aluminum caps)). In that situation the rattles move most likely the maximum distance in their pockets in the system. Some tracer particles which are slightly bigger than the biggest spheres in the granular packing and have a different coefficient of absorption for X-rays as the packing particles, for instance metal spheres in an environment of glass

spheres, are introduced during preparation. These tracer particles help to identify the exact positions before and after the sample rotation and they are most likely no rattlers because of their bigger sizes. After obtaining both data sets it is possible to compare the data due to the knowledge of the positions of the tracer particles before and after rotation. When now superimposing both data sets, most of the particle positions should be identical except the rattlers. By assuming the pockets of the rattlers have comparable sizes, so that the spheres move predominantly the same distances during rotation of the sample cell, an additional peak should appear in a pair correlation analysis. Fig. 2.27 show two radiography images produced as described above.

2.11 Monitoring Three-Dimensional Packings in Microgravity

In addition to the lab work in this thesis a parabola flight campaign (DLR-22) took place in April 2013. The experiment was built as a cooperation between different groups from the Institut of Material Science in Space at DLR. It is a X-ray source with a detector and a sample chamber for replaceable cartridges. During my thesis I supported Alexander Börngen who did his engineering master thesis on this topic. I supported him during the construction of the cartridge for the experiment and introduced him to X-ray measurement techniques. Peidong Yu analyzed the acquired data. The experimental technique which was used in the parabolic flight and the results are published in Granular Matter Journal [23].

2.11.1 Microgravity

Experiments with granular matter in microgravity allow access to regions in control-parameter space that are otherwise not accessible. Microgravity prevents the sedimentation of a loose non-agitated granular assembly and hence enables the long-term study of such states. For agitated granular matter, experiments in microgravity can reduce the inhomogeneity of driven states; and for particles in contact, the absence of gravity eliminates the pressure gradient in the packings. To what extent these goals can be realized in a specific experiment depends largely on the quality of the microgravity conditions found on specific platforms. Experiments have been performed for granular gases [2, 24, 25] as well as dense systems under shear [26, 27]. In the following sections, it will be shown how the microgravity environment

of a parabolic flight can be utilized for investigating granular packings. Results will be elaborated for X-ray radiography.

Microgravity environments are typically hard to obtain and require years of preparation. In contrast to experiments in space, parabolic flight campaigns offer a reasonably frequent opportunity to perform experiments under microgravity conditions. While not offering the best microgravity quality in terms of rest-accelerations, cf. discussion below, parabolic flights can help to test phenomena that depend on a distinction between top and bottom. One such phenomenon is convection. For a granular system under shear, convection was found perpendicular to the direction of shear along the direction of gravity [28]. On a parabolic flight however, it was observed recently, that in the absence of a distinction between top and bottom such convection disappears [26].

The limitation of such experiments on parabolic flights is the presence of rest-accelerations – called *g-jitter* – which drastically restrict the time the particles can stay in a granular gas without being collectively driven against the container walls within around a second. For dense granular matter, the *g-jitter* imposes a minimum necessary confinement for keeping granular packings confined.

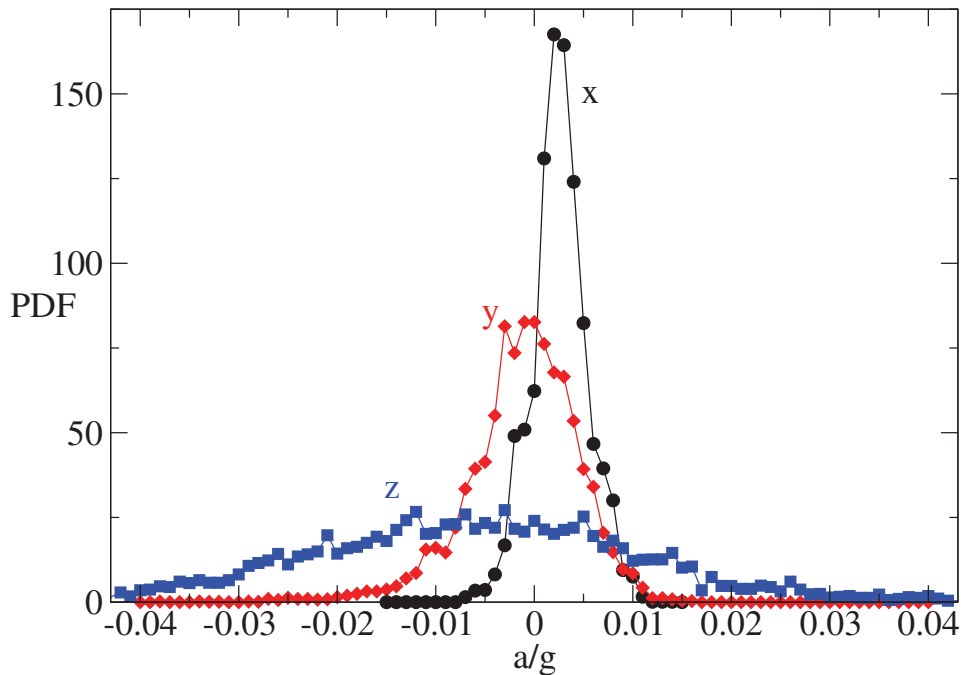


Figure 2.28: Distribution of rest accelerations averaged over a typical single parabola of 22 seconds on the third day of parabolic flight campaign DLR-22. Data are shown for the *x*- (circles, forward direction of the airplane), *y*- (diamonds, wing-to-wing direction of the airplane), and *z*-directions (squares, floor-to-ceiling direction of the airplane).

Fig. 2.28 shows the distribution of rest accelerations on a parabolic flight, averaged over a single parabola. The x -direction is defined from the tail to the front of the plane, the y -direction is from the left to the right wing when looking from the cabin to the cockpit, and the z -direction points from the floor to the ceiling of the cabin. Given the rather uncontrolled nature of the rest-accelerations, it is remarkable how well they follow reasonable distributions. The full width of the distributions at half maximum in units of g is 0.005 for the x -direction, 0.01 for the y -direction, and 0.04 for the z -direction. In addition to the width of the distributions showing rather large qualitative differences, also the maximum values in x - and z -directions show deviations from zero, $a_x^0/g \approx 0.0025$ (forward bias) $a_z^0/g \approx -0.012$ (downward bias). The y -direction is on average symmetric. Data for a single parabola typically look similar to Fig. 2.28 while being somewhat variable between individual parabolas.

Rather than trying to avoid the influence of the rest-accelerations, in the following experiments the g -jitter is utilized for providing agitation for dense granular systems.

2.11.2 X-Ray Radiography

The use of X-ray illumination facilitates the visualization of otherwise optically opaque samples. The simplest use of a combination of an X-ray source and a detector is by recording the transmission images after absorption from the sample in a radiography setup. X-ray radiography has been used to investigate hopper flow of sand [29] as well as the dynamics of granular matter in fluidized beds [30, 31, 32].

The aim of the present study using X-ray radiography is to investigate the compaction of a granular assembly into a dense packing. On ground the compaction is dominated by gravity-induced sedimentation and takes place rather rapidly within a fraction of a second and also comparably violently with shock waves traveling through the system [33]. In microgravity, the energy loss is still driven by inter particle collision but the rapid sedimentation is replaced by the compaction from the container walls which is chosen here to be rather moderate in speed.

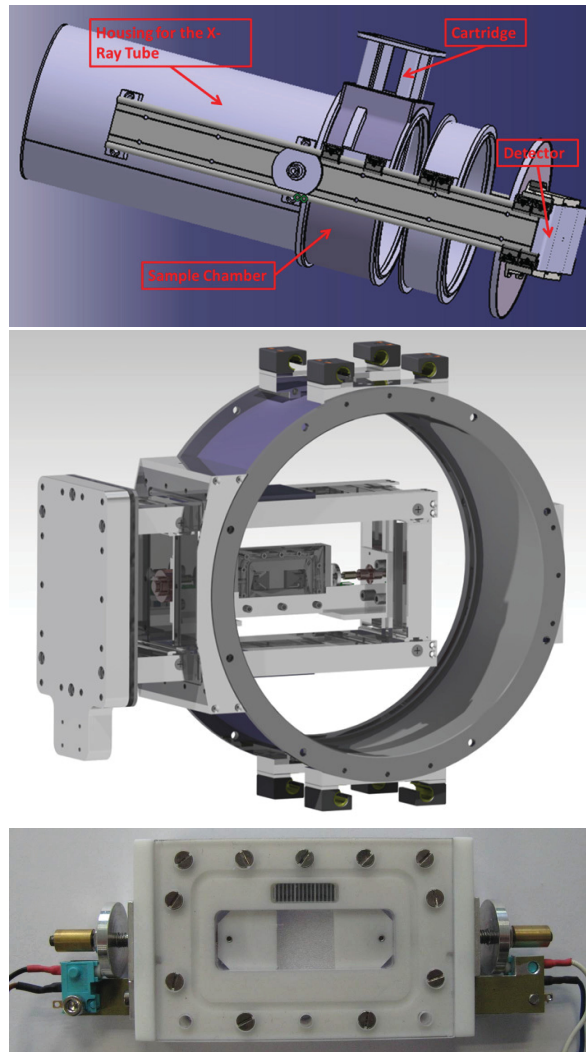


Figure 2.29: Experimental setup for the parabolic flight (DLR-22, April 2013) for X-ray radiography. The top panel shows a schematic view from left to right of the X-ray tube, the experiment chamber with sample cartridge, a spacer ring, and the detector. The central panel exhibits the sample chamber with the replaceable cartridge for granular experiments which is shown in the photograph of the bottom panel. The granular cartridge has two motorized pistons of cross-section 15mm×5mm and an X-ray ruler with a mm-scale on top.

Fig. 2.29 shows the setup of the radiography device. The source produces a divergent X-ray beam that irradiates a sample before being registered by the detector (CCD-/COOL-1100XR) with pixel size $9\mu\text{m}\times 9\mu\text{m}$ recording with a resolution of 2008×1340 pixels and 16-bit depth at 4 fps (frames per second). The placement of the sample between source and detector as well as their overall distance determines the magnification. Additional spacer rings can be used to increase the possible magnification. In the following,

a magnification factor of 2 was chosen. The actual sample cell is placed in a sample chamber in the form of a replaceable cartridge. In addition to changing granular samples easily, also samples other than granular matter can be used with the device. As seen in the bottom panel of Fig. 2.29, the granular sample cell contains the sample material inside a rectangular volume that can be changed by pistons on two sides. An X-ray ruler with a millimeter scale is used to calibrate the volume and hence the packing fraction of the experiments.

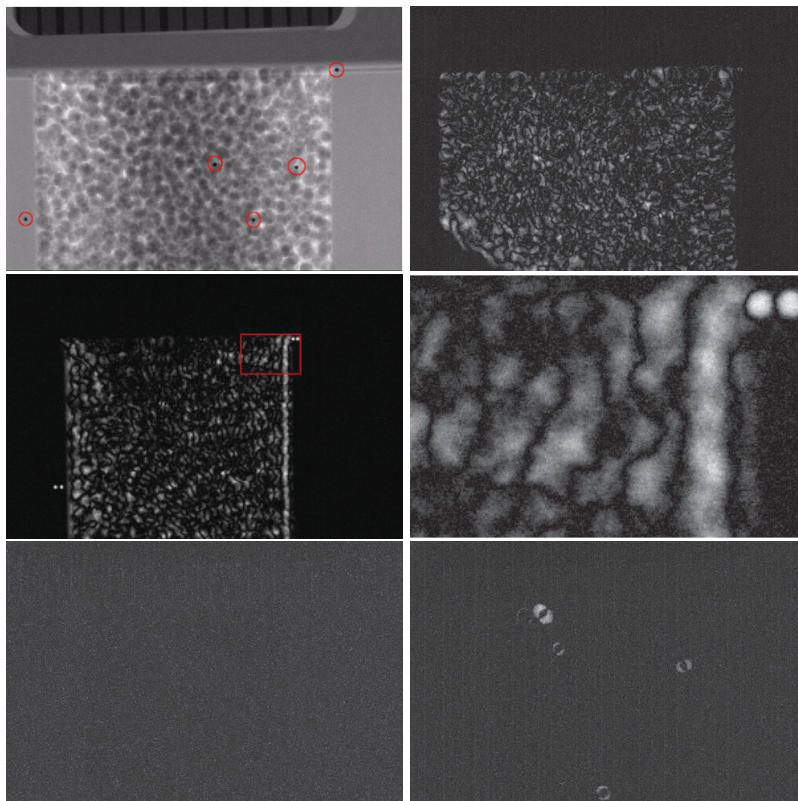


Figure 2.30: Radiography images from parabola number 1. The original transmission image (upper left) shows the pile of glass particles (diameter $500\mu\text{m}$) in the 2-g phase before the microgravity experiment. Gravity acts perpendicular to the plane of the image. Darker particles singled out by red circles are steel particles (diameter $200\mu\text{m}$) acting as tracers. The difference image (upper right) shows the motion between two successive frames due to g-jitter at the beginning of compaction (recording at four frames per second). A similar image (middle left) shows the differences immediately after motion of the pistons together with a rectangular frame for the enlarged selection shown on the next difference image (middle right). The fourth difference image (lower left) shows the absence of detectable motion after compaction and cooling of the arrested sample. The final difference image (lower right) illustrates the motion of four rattler particles at the transition from the 0g to the 2g-phase.

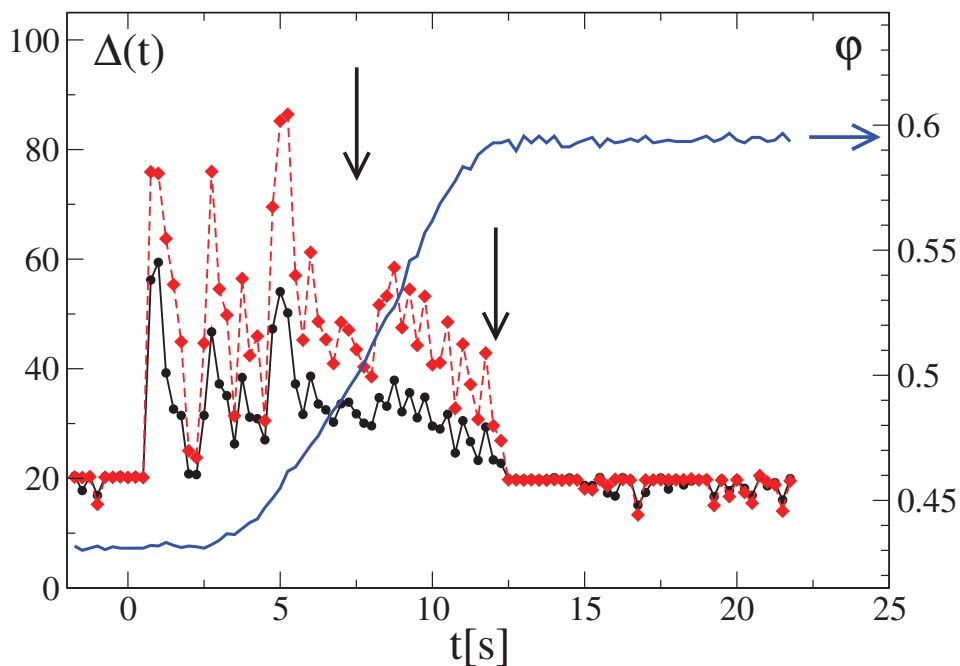
The device described above was used in the parabolic flight campaign DLR-22 in April 2013. The orientation of the X-ray beam was chosen in the z -direction of the airplane, so the largest dimensions of the sample cell were in the x - y -plane of the aircraft where the least overall bias of the g -jitter could be expected. The sample volume was filled with around 8000 glass particles of diameter $500\mu\text{m}$ (estimated coefficient of restitution $\varepsilon \approx 0.7$). Tracer particles of diameter $200\mu\text{m}$ were added to have access to individual particle trajectories. These particles were made from steel to ensure good contrast which is seen in the first panel of Fig. 2.30. The choice of tracer particles much smaller than the particles of the host system was motivated by the resolution limitations in both space and time: Smaller particles are more likely to be rattlers, i.e. show appreciable motion even inside an arrested state. The volume was filled with particles on ground and compacted with the pistons to form a stable packing without deforming the particles. Afterwards the pistons were retracted symmetrically and left the granular particles in a pile as seen in the upper left panel of Fig. 2.30 with more particles in the center than closer to the pistons. This asymmetry vanishes immediately after entering the microgravity phase where the g -jitter redistributes the particles homogeneously in the sample volume.

After agitation of the granular particles by g -jitter, the system was slowly compressed by the pistons from a packing fraction of around $\varphi = 0.43$ until the arrested state around $\varphi = 0.6$ was reached. The reported packing fractions are calculated from dividing the volume of the particles by the full available volume of the test cell. For the packed state we estimate the deviation of the true bulk packing fraction from the nominal one as follows: We subtract from the particle volume the sum of the half spheres of a completely covered layer of particles at the walls. From the cell volume we subtract the corresponding sum of half-cubes. The resulting boundary-corrected value for the packing fraction at the arrested state, $\varphi = 0.6$, is found at $\tilde{\varphi} = 0.615$, i.e. a deviation of 2.5% for the bulk value inside the sample. Since this correction is not reasonable for more dilute assemblies down to nominal packing fraction of 0.43, the nominal values are reported in the following. Even accounting for the outlined boundary correction, the arrested sample does not reach values for the packing fraction commonly reported for random-close packing of around $\varphi = 0.64$. The lower packing fraction at the arrested state in our samples is explained by the comparably high friction among the particles.

The difference image in the upper right panel of Fig. 2.30 shows the absolute intensity variation from one frame to the successive one and hence characterizes the overall motion across the sample. It is found that the particles at the initial volume are quite well agitated. The volume of particles in that difference image is distinguished well from the container walls which do

not move and appear black plus some noise. The middle panels of Fig. 2.30 show the motion immediately after compression by the pistons which is visible by the two trapped tracer particles on the lower-left and upper-right corners. While on the right wall a whole layer of particles is displaced together, on the left wall the energy input yields a more random pattern. This difference is not very surprising as the particle density at both walls is not necessarily the same before the particles are packed densely. A rectangular frame in the middle left panel indicates an area in the full test cell that is shown magnified by a factor of seven in the middle right panel. It is clear from the enlarged image that in the setup individual tracer particles can be resolved.

Once the final close-packed volume is reached, the motion in the sample cell vanishes as seen by the completely dark difference image in the lower left. Container and particle packing are then indistinguishable. The final difference image in Fig. 2.30 shows the observations at the transition from microgravity to 1.8g at the end of a parabola: As both new and old position of a particle show up brightly, four individual particles can be identified as moving on the timescale of a quarter second. We interpret these as rattlers that have lost all their energy during cooling inside the packing and are now pulled downwards by the 2g acceleration.



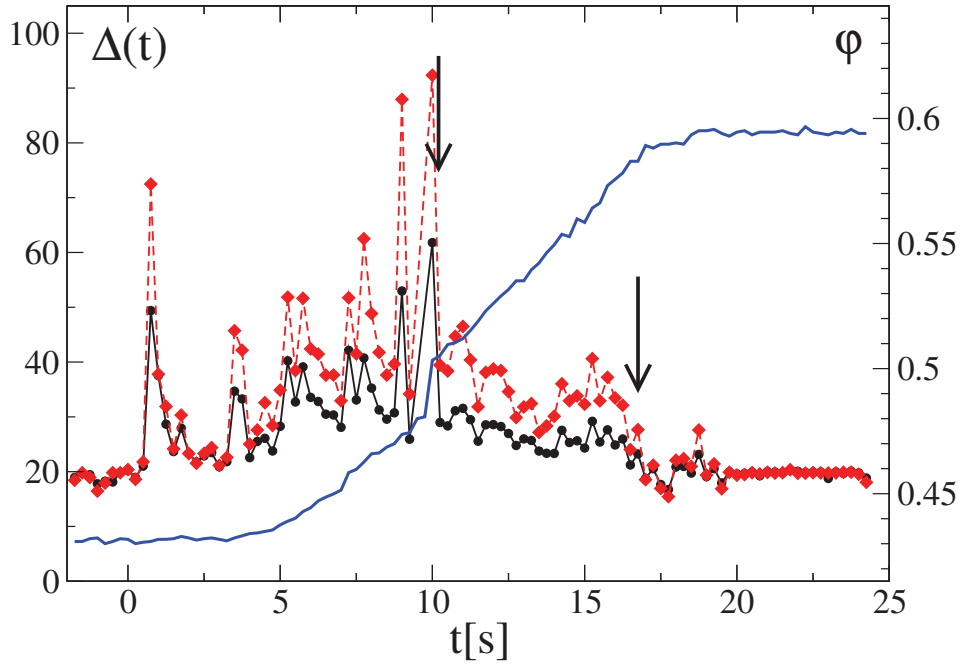


Figure 2.31: Dynamics of the granular particles during the slow compaction process. The plots display the overall brightness of successive difference images $\Delta(t)$ on the left axes over time during the microgravity phase for a representative compaction run within 10 seconds (parabola 10, upper panel) and a run within 13 seconds (parabola 1, lower panel). The respective right axes display the evolution of the packing fraction for the full curve. The two curves for $\Delta(t)$ show the average over the full sample (filled circles) and the center of the cell without boundaries (diamonds). Vertical arrows indicate a region of slow cooling (see text).

The time evolution of the brightness in the difference images can serve as an estimate of the granular system's kinetic energy and hence the decrease in brightness signals granular cooling. This evolution of the brightness is shown in Fig. 2.31. The brightness of the difference images $\Delta(t)$ is defined by the averaged greyvalue per pixel over a region of interest. The region of interest is taken either for the entire probe-cell volume (with the trade-off of including the pistons for the later part of the compaction) shown as diamonds as well as over only the central quadratic region filled with particles after compaction without any boundaries shown by the filled circles (with the trade-off of missing some particles close to the walls at the earlier part). Both definitions of the region of interest yield no qualitative difference in the observed data, so it seems both definitions capture the particle dynamics reasonably well and the dynamical features are dominated by the behavior in the bulk. The origin of the time scale is set to the beginning of the 0g phase. The compaction is seen by the evolution of the packing fraction over time.

The overall packing fraction is reduced by $\Delta\varphi/\Delta t = 0.017/s$ for compaction in 10s and by $\Delta\varphi/\Delta t = 0.013/s$ for compaction in 13s, respectively. For those slow compaction rates, data from 10 parabolas was used. Similar five runs have been obtained for a fast compaction rates of $\Delta\varphi/\Delta t = 0.04/s$ which is not shown in the figure but discussed below.

For slow compaction, at both reported compaction rates the reproducible observations can be summarized as follows.

(1) Throughout all the runs, both for the beginning when particles are at rest in 1.8g and at the end of compaction when still in a noisy 0g environment, the background value is always $\Delta_0 = 20$. There is no observable drift in Δ_0 and in the $\Delta(t)$ over different runs. Faster overall motion of the particles as apparent from the original images is reflected in a higher amplitude of Δ .

(2) At the start of 0g, the system is shaken strongly and exhibits strong fluctuations in $\Delta(t)$ seen by the large peaks in both panels of Fig. 2.31 on the respective left sides. The fluctuations are not affected by the compaction which is setting in after a few seconds in 0g.

(3) Around $\varphi = 0.5$ (indicated by vertical arrows in Fig. 2.31) fluctuations are dampened and the evolution of $\Delta(t)$ suggests a regime a granular cooling. This cooling regime was found for 10 out of 11 runs with slow compaction. For the single exception the pistons got stuck and snapped before a cooling regime can be identified in the data. A reminiscence of that stick-slip piston behavior can be seen around 10s in the lower panel of Fig. 2.31 in the curve for the packing fraction.

(4) The cooling regime shows up similarly for both definitions of a region of interest; the more restricted region of interest (diamonds) is used for the quantitative analysis in the following. The slow cooling can be described by a linear law $\Delta(t) - \Delta_0 = \tilde{\Delta}\gamma t$ where $\tilde{\Delta}$ describes the overall amplitude, i.e. the equivalent of granular temperature, at the beginning of the cooling. For the amplitude we obtain $\tilde{\Delta} = 40$ for the upper panel in Fig. 2.31 and $\tilde{\Delta} = 30$ for the lower panel. Parameter γ describes a normalized cooling rate that turns out to be well reproducible across all 10 parabolas for slow cooling with no significant difference for different compaction rates: $\gamma = 0.13 \pm 0.02/s$.

(5) The linear regime for slow cooling is terminated upon reaching the final packing fraction by a fast cooling regime where within around 1s the complete dynamics comes to rest, i.e. $\Delta(t) = \Delta_0$. The limited time resolution of the data does not allow a more quantitative statement, but the fast cooling regime is always identified clearly, the linear regime for slow cooling does not extend all the way to Δ_0 . After the fast cooling regime, the sample is arrested. Note that the appearance of rattlers as seen in Fig. 2.30 is not visible above the noise level in $\Delta(t)$. Observations (1) to (5) as elaborated above are found for all realizations of slow compaction for 10 parabolas. In particular, the limit of $\varphi = 0.5$ where fluctuations become smaller and cooling sets in,

is reproducible across the available data. If the compaction is around four times faster as investigated for additional five parabolas, no such limit exists and no such regime of slow cooling can be identified. Also, in Fig. 2.31 one observes that the range of validity for the linear law shrinks from 6.5s for compaction rate $\Delta\varphi/\Delta t = 0.013/s$ to 4.5s for $\Delta\varphi/\Delta t = 0.017/s$. Hence, we conclude that the existence of a slow cooling regime depends on the balance between energy input (from g -jitter and the compaction process) and the rate of dissipation (given by ε) and can be tuned by the rate of compaction. For fast enough compaction, the slow cooling regime vanishes.

The averages of the cooling dynamics for all available data from the parabolic flight are shown in Fig. 2.32. For the small compaction rate $\Delta\varphi/\Delta t = 0.013/s$, data from parabolas P0, P1 (cf. lower panel in Fig. 2.31), P2, P3, P4, and P5 are first rescaled in time to overlap in the evolution regarding the packing fraction φ with $\varphi = 0.5$ chosen as $t = 0$. Then the data for $\Delta(t)$ is averaged over the 6 data sets and shown for the full range of pixels as open circles (upper panel of Fig. 2.32) as well as open diamonds (lower panel of Fig. 2.32). Running averages in time are used to obtain the somewhat smoother corresponding full curves. Data for compaction rate $\Delta\varphi/\Delta t = 0.017/s$ is treated similarly and displayed as filled circles (upper panel) and filled diamonds (lower panel). From the averaged dynamics, linear cooling laws can be obtained that are consistent with the results from the single runs described above: Compaction rate 0.013/s is described by $\Delta(t) - \Delta_0 = 10 - 1.33t$ while compaction rate 0.017/s follows $\Delta(t) - \Delta_0 = 12.5 - t$ in the upper panel. The different slopes in those laws follow the variation of the overall amplitude of $\Delta(t)$ varies by around 25%. In the lower panel the corresponding laws read $\Delta(t) - \Delta_0 = 2.2(10 - 1.33t)$ and $\Delta(t) - \Delta_0 = 2.2(12.5 - t)$, respectively. Hence, the limitation to the pixels in the selected region only introduces an additional amplitude.

The linear law is valid for around 4s for $\Delta\varphi/\Delta t = 0.017/s$ and for 8s for the compaction rate 0.013/s which may be accidental. Also for the averaged data, the slow linear cooling is followed by a more rapid decay of $\Delta(t)$. Again, the final rapid collapse takes place within a second and it is observed in Fig. 2.32 that the final decays may be scaled on top of each other for different compaction rates. It is possible to interpret the data for different compaction rates by a roughly constant decay rate γ and a shrinking range of validity in time after which the final collapse terminates the slow cooling. The fits of the individual decay curves for $\Delta(t)$, cf. Fig. 2.31, yield such a constant γ when averaged. It is also possible to imagine that the cooling regime vanishes by a decreasing slope γ whereby the increased energy input at higher compaction rates can overcompensate for the dissipation. The latter scenario is consistent with the finding that in the fits of the averaged $\Delta(t)$ in Fig. 2.32, a slight decrease in the value of γ is obtained.

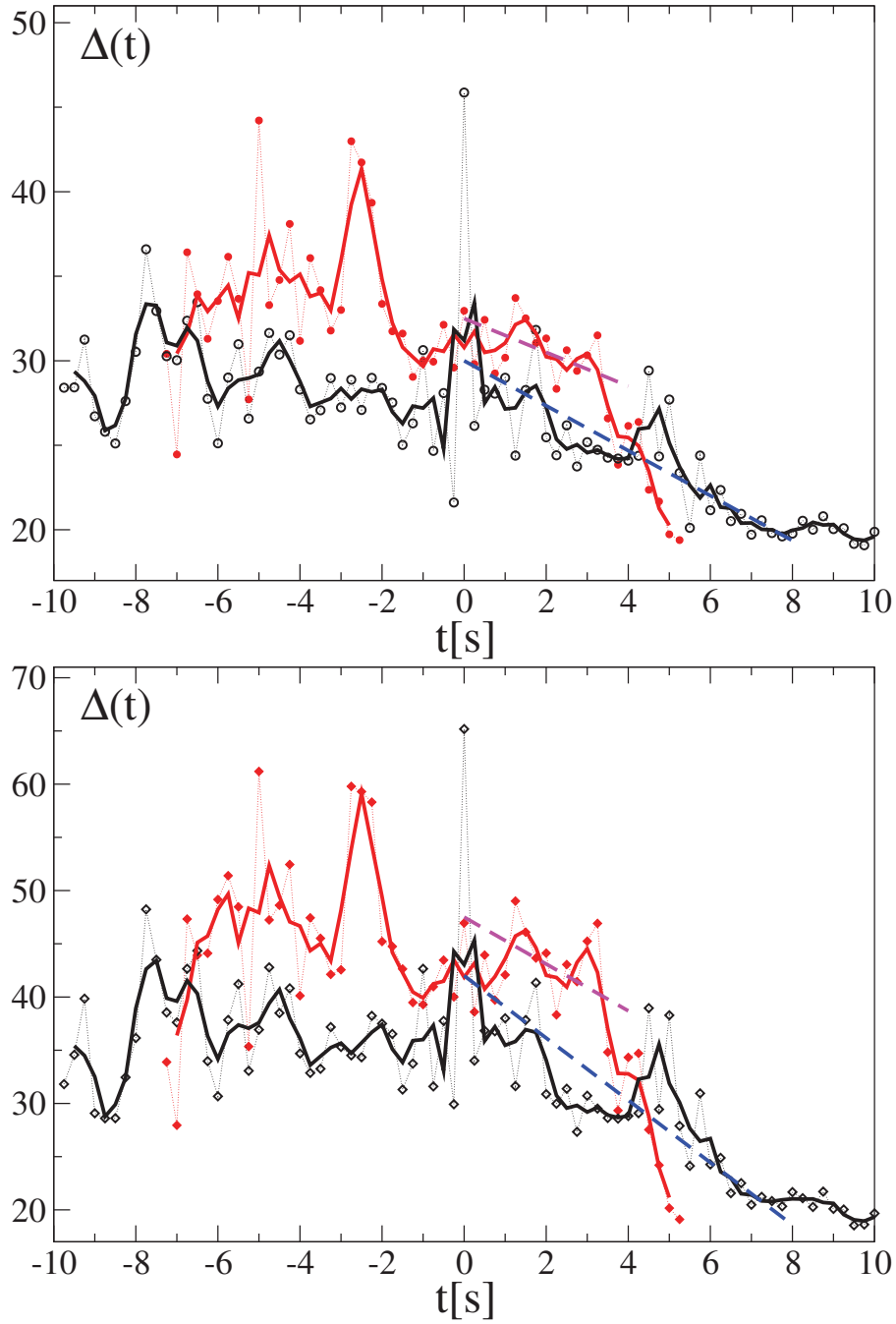


Figure 2.32: Averages over the particle dynamics during the slow compaction process evaluated for all pixels (top panel) and the selected region of pixels (bottom panel). The origin of time is set to the time when $\varphi = 0.5$ for each run. The open symbols in both panels represent the average over parabolae P0 to P5 (compaction rate $\Delta\varphi/\Delta t = 0.013/s$) while the full symbols show results from parabolae P6 to P10 (compaction rate $\Delta\varphi/\Delta t = 0.017/s$). Full curves are corresponding running averages in time over 0.5s, i.e. the average of three data points. Dashed straight lines display the linear laws $\Delta(t) = \tilde{\Delta}\gamma t$.

Chapter 3

3D Stress-Birefringence

3.1 Theoretical Background and Calibration

3.1.1 Stress Birefringent Technique

Materials are called birefringent if their index of refraction depends on the direction of the polarization of passing light. These properties can be found in many minerals in nature such as quartz, boron nitride, or calcite. A material is called stress birefringent if the index of refraction depends on the polarization of light only when mechanical stress is applied to the material. Such materials show no birefringent behavior as long as no force is applied. One can say that the degree of birefringence depends on the applied stress. The basic mechanism behind this phenomenon is that stress birefringent materials consist of optically anisotropic molecules which are randomly orientated. All these molecules show birefringent behavior but macroscopically this effect is averaged out due to the random orientation of these molecules. If stress is now applied to the material, a preferred direction arises. In this situation the microscopic optical anisotropy of each molecule is not averaged out any more and the material shows a birefringent behavior depending on the applied force [34].

This intrinsic stress birefringent property can be used to visualize forces in granular packings when the particles are made of suitable material [35, 36, 37, 38, 39].

3.1.2 Polariscopes

The forces in a three dimensional granular packing consisting of stress birefringence particles can be visualized by using polarized light transmitting through the sample and an analyzer to identify the phase shift caused by the material in the sample. Such a setup is known as a polariscopes. The easiest way to analyze stresses in a sample is to use a linear polariscopes setup. It

consists of two crossed linear polarizers with the sample in between. When no stresses are applied, the sample is not birefringent and no light is passing through the second polarizer. As soon as stresses are present, the sample becomes birefringent and a fraction of the polarized light changes the polarization direction. This fraction of light passes through the second polarizer. The transmitted light intensity I can be calculated by:

$$I = I_0 \sin^2(2\alpha) \sin^2\left(\frac{\Delta\phi}{2}\right) \quad (3.1)$$

Where I_0 is the incoming light intensity, α is defined as the angle between the directions of the first linear polarizer and the internal principal stress axes of the sample and $\Delta\phi$ is the phase shift caused by the material in the sample.

However, the α dependence in the expression $I \propto \sin^2(2\alpha)$ is undesired (see equation 3.1) because for every $\alpha = k\pi, k \in \mathbb{N}$ it partially suppresses the information about the phase shift $\Delta\phi$.

To get rid of the expression $I \propto \sin^2(2\alpha)$ it is possible to use a circular polariscope with a circular polarizer instead of a linear polarizer. A circular polarizer consists of a linear polarizer and a $\frac{\lambda}{4}$ -retarder plate. The slow and the fast axis of the $\frac{\lambda}{4}$ -plate need to have an angle of 45° relative to the direction of the polarization defined by the first linear polarizer. Consider two circular polarizers which are set in a row and orientated as

1st polarizer – 1st $\frac{\lambda}{4}$ -plate/sample/ 2nd $\frac{\lambda}{4}$ -plate – 2nd polarizer.

This system can also be described as one left handed and one right handed circular polarizer setup (see Fig. 3.1).

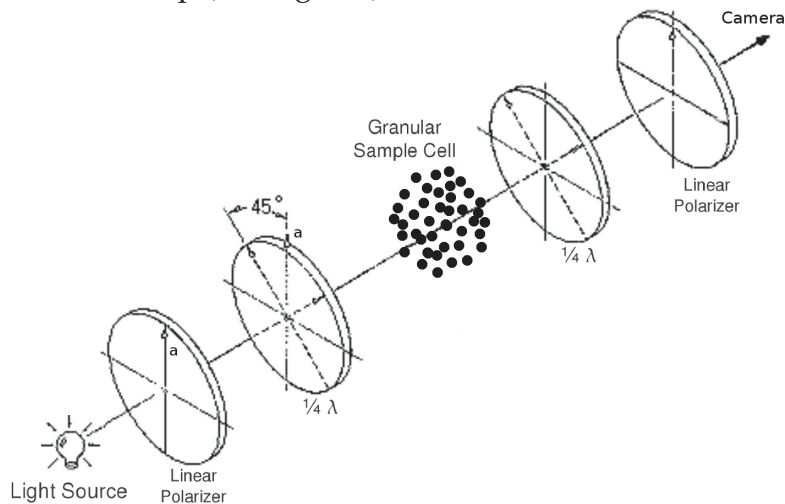


Figure 3.1: Sketch of a circular polariscope. (adapted from ©Viashay Measurement Corp.)

Together both $\frac{\lambda}{4}$ -plates flip the polarization of the light transmitted from the first linear polarizer by 90° . Hence the light is completely blocked by the second linear polarizer. As compared to the linear polarizer setup, the light arriving at the stress birefringent material is now circularly polarized. Thus, the interaction between the incident light and the sample should be invariant when rotating the sample around the optical axis of the polariscope. Consequently the angle dependence α in equation 3.1 does not occur any more. The transmitted light intensity I for a circular polariscope can be calculated by:

$$I = I_0 \sin^2\left(\frac{\Delta\phi}{2}\right) \quad (3.2)$$

Where I_0 is the incoming light intensity and $\Delta\phi$ is the phase shift caused by the material of the sample.

3.1.3 Phase Shift $\Delta\phi$ for a Diametrically Loaded Sphere

The phase shift $\Delta\phi$ in equation 3.2 can be calculated via $\Delta\phi = \frac{2\pi R_t}{\lambda}$, where λ is the wave length of light and R_t is the retardation caused by the sample. In two dimensions the stress-optic law gives a relation between the retardation R_t and the stress tensor σ of the material.

$$R_t = C_s t(\sigma_1 - \sigma_2), \quad (3.3)$$

where C_s is the stress-optical coefficient and σ_1, σ_2 are the eigenvalues of the two dimensional stress tensor.

In the following, the general approach for calculating the stress tensor and thus the retardation for a three dimensional, diametrically loaded sphere of radius a will be demonstrated. The stress calculation is described in [40]. Due to the symmetry of the problem, a description in spherical coordinates is suitable. The stress tensor in spherical coordinates $\sigma_{r,\theta,\phi}$ has the expression (see also Fig. 3.2):

$$\sigma_{r,\theta,\phi} = \begin{bmatrix} \sigma_r & \tau_{r\theta} & \tau_{r\phi} \\ \tau_{\theta r} & \sigma_\theta & \tau_{\theta\phi} \\ \tau_{\phi r} & \tau_{\phi\theta} & \sigma_\phi \end{bmatrix}$$

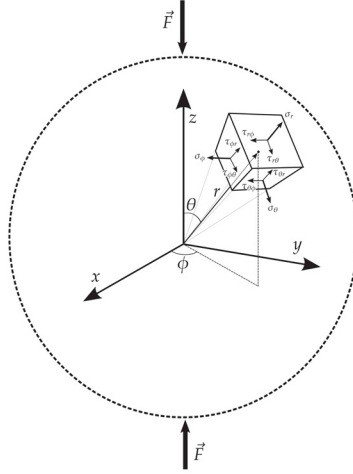


Figure 3.2: Stress tensor visualized in a sphere referring to spherical polar coordinates.

Assuming that the deformation of the sphere is small compared to the size of the sphere and its material is homogeneous and isotropic. In case that the stress components depend linearly on the strain components of the loaded sphere (Hook's law) it is possible to describe the relation through Lamé's parameters which are directly related to the elastic constants of Young's modulus E and Poisson's ratio ν :

$$\sigma_{ij} = 2\mu\epsilon_{ij} + \lambda tr(\epsilon)\delta_{ij} \quad (3.4)$$

where σ_{ij} is the stress tensor, ϵ_{ij} is the strain tensor, $\lambda = \frac{\nu E}{(1+\nu)(1-2\nu)}$ is Lamé's first parameter and $\mu = \frac{E}{2(1+\nu)}$ Lamé's second parameter (also known as shear modulus). Under these conditions it is possible to find a solution for the components of the stress tensor which only depend on the elastic constants of the material. The stress components in the sphere must satisfy the following equations:

$$\frac{\partial \sigma_r}{\partial r} + \frac{1}{r} \frac{\partial \tau_{r\theta}}{\partial \theta} + \frac{1}{r} (2\sigma_r - \sigma_\theta - \sigma_\phi + \tau_{r\theta} \cot \theta) = 0 \quad (3.5)$$

$$\frac{\partial \tau_{r\theta}}{\partial r} + \frac{1}{r} \frac{\partial \sigma_\theta}{\partial \theta} + \frac{1}{r} ((2\sigma_\theta - \sigma_\phi) \cot \theta + 3\tau_{r\theta}) = 0 \quad (3.6)$$

$$\frac{\partial \tau_{r\phi}}{\partial r} + \frac{1}{r} \frac{\partial \tau_{\theta\phi}}{\partial \theta} + \frac{1}{r} (3\tau_{r\phi} + 2\tau_{\theta\phi} \cot \theta) = 0 \quad (3.7)$$

owing to the equilibrium of forces and the symmetric argument that any stress component has to be independent of ϕ (see Fig.3.2). From the extrema $r = 0$ and $r = a$ (a is the diameter of the sphere) two conditions can be derived :

- For $r = 0$ every stress component must take a finite value and therefore the terms with $\frac{1}{r^n}$, $\frac{1}{r^{n+1}}$ and $\frac{1}{r^{n+2}}$ in the equations (3.8)-(3.13) should be zero.
- For $r = a$ it applies $\tau_{r\theta} = \tau_{\theta\phi} = \tau_{\theta r} = 0$.

In order to avoid singularities for sharp point forces a pressure with a finite area $p = \frac{F}{2\pi a^2(1-\cos\theta_0)}$ is being defined. If the pressure acts normally and uniformly on the surface of the sphere and is rotationally symmetrical with respect to the z-axis and the direction of the load is diametrically opposed and centered, an angle θ_0 can be defined which corresponds to the loaded area (see Fig. 3.3). For the stress tensor component σ_r :

$$(\sigma_r)_{r=a} = \begin{cases} p & \text{for } 0 \leq \theta \leq \theta_0, \pi - \theta_0 \leq \theta \leq \pi \\ 0 & \text{for } \theta_0 < \theta < \pi - \theta_0 \end{cases}$$

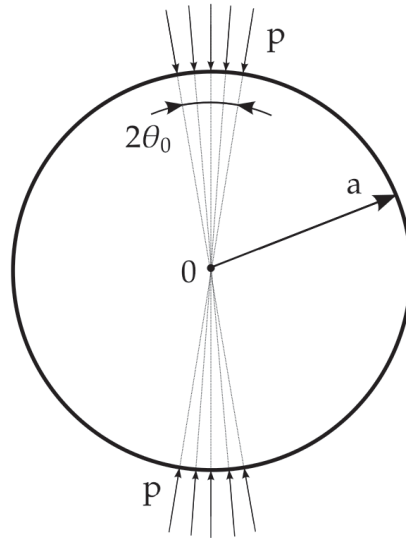


Figure 3.3: Sketch showing a diametrically loaded sphere with radius a . Pressure p is applied diametrically to an area defined by θ_0

When the displacements of r , θ , and ϕ are described by Δ_r , Δ_θ and Δ_ϕ respectively, the components of the stress tensor look like:

$$\sigma_r = \frac{\lambda}{r^2 \sin \theta} \left(\frac{\partial}{\partial r} (r^2 \Delta_r \sin \theta) + \frac{\partial}{\partial \theta} (r \Delta_\theta \sin \theta) \right) + 2\mu \frac{\partial \Delta_r}{\partial r} \quad (3.8)$$

$$\sigma_\theta = \frac{\lambda}{r^2 \sin \theta} \left(\frac{\partial}{\partial r} (r^2 \Delta_r \sin \theta) + \frac{\partial}{\partial \theta} (r \Delta_\theta \sin \theta) \right) + 2\mu \left(\frac{1}{r} \frac{\partial \Delta_\theta}{\partial \theta} + \frac{\Delta_r}{r} \right) \quad (3.9)$$

$$\sigma_\phi = \frac{\lambda}{r^2 \sin \theta} \left(\frac{\partial}{\partial r} (r^2 \Delta_r \sin \theta) + \frac{\partial}{\partial \theta} (r \Delta_\theta \sin \theta) \right) + 2\mu \left(\frac{\Delta_r}{r} + \frac{\Delta_\theta}{r} \cot \theta \right) \quad (3.10)$$

$$\tau_{r\theta} = \mu \left(\frac{\partial \Delta_\theta}{\partial r} - \frac{\Delta_\theta}{r} + \frac{1}{r} \frac{\partial \Delta_r}{\partial \theta} \right) \quad (3.11)$$

$$\tau_{\theta\phi} = \mu \left(\frac{1}{r} \frac{\partial \Delta_\phi}{\partial \theta} - \frac{\Delta_\phi}{r} \cot \theta \right) \quad (3.12)$$

$$\tau_{\phi r} = \mu \left(\frac{\partial \Delta_\phi}{\partial r} - \frac{\Delta_\phi}{r} \right) \quad (3.13)$$

When satisfying the boundary conditions, the solution (see [40]) of the equations (3.8)-(3.13) leads to a system of Legendre polynomials, $P_n(x)$. Specifically, the solutions of the stress tensor components in spherical coordinates are:

$$\begin{aligned} \sigma_r = \sum_{i=0}^{\infty} \left[P_n(\cos(\theta)) \left(- \frac{(4n^2 - 2n - 3)\lambda + (2n + 1)(2n - 2)\mu}{(4n + 3)} r^{2n} \right. \right. \\ \left. \left. + \frac{4n^2(2n + 1)\lambda + 2n(4n^2 + 4n - 1)\mu}{(2n + 1)(4n + 3)} a^2 r^{2n-2} \right) \right. \\ \left. \times \left(\frac{-(4n + 3)(4n + 1)(\cos \theta_0 P_{2n}(\cos \theta_0) - P_{2n-1}(\cos \theta_0))}{((8n^2 + 8n + 3)\lambda + (8n^2 + 4n + 2)\mu) a^{2n}} \right) p \right] \quad (3.14) \end{aligned}$$

$$\begin{aligned}
\sigma_\theta = \sum_{i=0}^{\infty} & \left[\left(P_{2n}(\cos(\theta)) \left(\frac{(2n+3)\lambda - (2n-2)\mu}{4n+3} r^{2n} \right. \right. \right. \\
& + \frac{4n^2(2n+1)\lambda + 2n(4n^2+4n-1)\mu}{(2n-1)(2n+1)(4n+3)} a^2 r^{2n-2} \left. \left. \left. \right) \right. \right. \\
& + \frac{\partial^2 P_{2n}(\cos\theta)}{\partial\theta^2} \left(- \frac{(2n+3)\lambda + (2n+5)\mu}{(2n+1)(4n+3)} r^{2n} \right. \\
& \left. \left. \left. + \frac{2n(2n+2)\lambda + (4n^2+4n-1)\mu}{(2n-1)(2n+1)(4n+3)} a^2 r^{2n-2} \right) \right) \right. \\
& \left. \times \left(\frac{-(4n+3)(4n+1)(\cos\theta_0 P_{2n}(\cos\theta_0) - P_{2n-1}(\cos\theta_0))}{((8n^2+8n+3)\lambda + (8n^2+4n+2)\mu)a^{2n}} \right) p \right] \quad (3.15)
\end{aligned}$$

$$\begin{aligned}
\sigma_\phi = \sum_{i=0}^{\infty} & \left[\left(P_{2n}(\cos(\theta)) \left(\frac{(2n+3)\lambda - (2n-2)\mu}{4n+3} r^{2n} \right) \right. \right. \\
& + \frac{4n^2(2n+1)\lambda + 2n(4n^2+4n-1)\mu}{(2n-1)(2n+1)(4n+3)} a^2 r^{2n-2} \left. \left. \right) \right. \\
& + \cot(\theta) \frac{\partial P_{2n}(\cos\theta)}{\partial\theta} \left(- \frac{(2n+3)\lambda + (2n+5)\mu}{(2n+1)(4n+3)} r^{2n} \right. \\
& \left. \left. \left. + \frac{2n(2n+2)\lambda + (4n^2+4n-1)\mu}{(2n-1)(2n+1)(4n+3)} a^2 r^{2n-2} \right) \right) \right. \\
& \left. \times \left(\frac{-(4n+3)(4n+1)(\cos\theta_0 P_{2n}(\cos\theta_0) - P_{2n-1}(\cos\theta_0))}{((8n^2+8n+3)\lambda + (8n^2+4n+2)\mu)a^{2n}} \right) p \right] \quad (3.16)
\end{aligned}$$

$$\begin{aligned}
\tau_{r\theta} = \sum_{i=0}^{\infty} & \left[\frac{\partial P_{2n}(\cos\theta)}{\partial\theta} (-r^{2n} + a^2 r^{2n-2}) + \frac{2n(2n+2)\lambda + (4n^2+4n-1)\mu}{(2n+1)(4n+3)} \right. \\
& \left. \times \left(\frac{-(4n+3)(4n+1)(\cos\theta_0 P_{2n}(\cos\theta_0) - P_{2n-1}(\cos\theta_0))}{((8n^2+8n+3)\lambda + (8n^2+4n+2)\mu)a^{2n}} \right) p \right] \quad (3.17)
\end{aligned}$$

$$\tau_{\theta\phi} = 0 \quad (3.18)$$

$$\tau_{\phi r} = 0 \quad (3.19)$$

These are the solutions for the stress tensor components for a diametrically loaded sphere, subject to a pressure p under the boundary conditions described above.

3.1.4 Analytical Calculation and Experiment

With the help of Dr. Peidong Yu, who implemented the analytical solution for the diametrically loaded sphere as described in section 3.1.3 in a computer code, the calculated results are compared with the results from the experiment.

Analytical Calculation

The strategy to generate a two dimensional light intensity map which is comparable to those of the experiment is to discretize the sphere into a series of small cubes. For each cube the phase retardation of the polarization of the transmitting light, caused by the stresses in the sphere, is calculated and serves as the initial polarization to the next cube in beam direction. At the end of each series the resulting polarization state and thereby the intensity is determined.

In technical terms, it is necessary to first transform the stress tensor $\sigma_{r,\theta,\phi}$ in an expression in cartesian coordinates $\sigma_{x,y,z}$

$$\sigma_{x,y,z} = \begin{bmatrix} \sigma_x & \tau_{xy} & \tau_{xz} \\ \tau_{yx} & \sigma_y & \tau_{yz} \\ \tau_{zx} & \tau_{zy} & \sigma_z \end{bmatrix} = A\sigma_{r,\theta,\phi}A^T$$

with the transformation matrix A

$$A = \begin{bmatrix} \sin \theta \cos \phi & \sin \theta \sin \phi & -\cos \theta \\ \sin \phi \cos \theta & \sin \phi \sin \theta & \sin \theta \\ \cos \theta & -\sin \theta & 0 \end{bmatrix}$$

The polarization status of the light beam is fully represented by the Stokes vector, \vec{S} . If the light ellipse is described by the amplitudes of the electric field vector components E_x and E_y in the transverse direction (the light beam propagates in the z-direction) and by their phase shift Δ , the Stokes vector has the expression:

$$\vec{S} = \begin{bmatrix} S_0 \\ S_1 \\ S_2 \\ S_3 \end{bmatrix} = \begin{bmatrix} E_x^2 + E_y^2 \\ E_x^2 - E_y^2 \\ 2E_xE_y\cos\Delta \\ 2E_xE_y\sin\Delta \end{bmatrix}$$

To be able to transform the Stokes vector depending on the stresses in the sphere the *Mueller matrix* $\{m_{ij}\}$ can represent the stress tensor $\sigma_{x,y,z}$. The Stokes vector for the emergent light is named \vec{S}_e and for the incident light it is \vec{S}_i , the transformation can be described by (see [41]):

$$\vec{S}_e = \{m_{ij}\}\vec{S}_i \quad (3.20)$$

The intensity I of an electromagnetic wave is proportional to the amplitude of the square $I \propto E^2$. Hence the intensity of the electromagnetic wave is proportional to the Stokes parameter $I \propto S_0$ and we can directly use this value to map the intensity.

Comparing Calculation and Experiment

The sphere for the comparison experiment was made by a two component resin and hardener system obtained from the VISHAY Micro-Measurements company. Specifically, in the present experiment PL-3 Liquid Plastic was used, which was casted in a casting mold. For index matching the same procedure as described in section 3.4 was applied. In the case of PL-3 the index match liquid combination of Diethyl phthalate ($C_{12}H_{14}O_4$) with an index of refraction of 1.501 and cassia oil from the *SAFCTM* company with an index of refraction of 1.614 was used. The sphere had a diameter of $\varnothing 30\text{mm}$. The measurement was performed with the same setup as described in section 3.4. Fig. 3.4 shows a picture series which compares the analytical result with the experimental data. Sixteen pictures are presented for different forces. On the left side the experimental pictures are shown and on the right side the related analytical solutions.

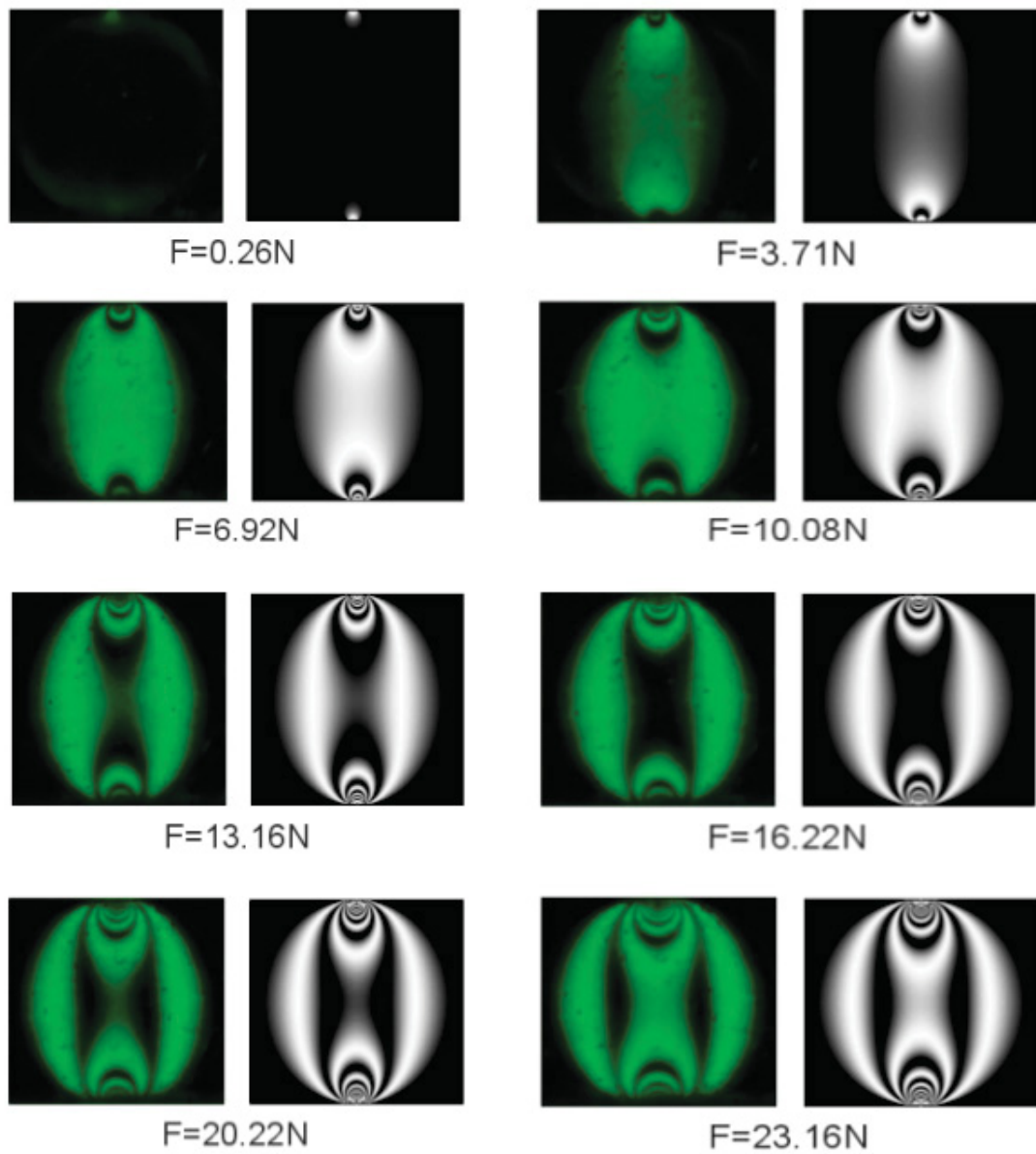


Figure 3.4: Picture series comparing experimental picture with related analytical solution for a diametrically loaded stress birefringent sphere. Left: experimental picture and right: related analytical solution. The sphere for the experiment is made by PL-3 from VISHAY Micro-Measurements company and has a diameter of $\varnothing 30\text{mm}$.

3.1.5 Stress Optical Calibration

The solution for a diametrically loaded sphere presented in section 3.1.3 describes only a fraction of possible contacts of a sphere in a three dimen-

sional complex packing. To interpret all measurable contact distributions of a sphere in a three dimensional granular system with analytical calculations, including force resolution for individual particles, the method needs improvement.

Nevertheless to get access to some essential information of the measured packing data such as the random close packing transition density φ_{rcp} a calibration for the overall light intensity have been used in this thesis.

Assuming that during compaction a granular system reacts linear to the applied pressure and hence the contact forces F at each individual particle, the components of the stress tensor are proportional to the contact forces $\sigma \propto F$. On the other hand an elastic sphere to sphere force contact can be described by the Hertzian contact law

$$F = \frac{4}{3}E^*R^{\frac{1}{2}}d^{\frac{3}{2}}. \quad (3.21)$$

with $E^* = \frac{E}{2(1-\nu)}$ where E is Young's modulus and ν is Poissons ratio. This applies to $R : \frac{1}{R} = \frac{1}{R_1} + \frac{1}{R_2}$ where R_1 is the radius of the first sphere, R_2 is the radius of the second sphere and d is the indentation. Figure 3.5 show the data for the force response of a Polydimethylsiloxan (PDMS) sphere with a radius of 8mm (see subsection 3.3.1) to an increasing indentation from 0 to 1mm. In the diagram $\frac{F^2}{R}$ vs d^3 is plotted in order to make a linear fit to the data. The slope of the fit enables to calculate the Youngs's modulus for the specific material in use. For PDMS with a Poissons ratio of approximately 0.5 (literature value) the Youngs's modulus is $E \approx 0.684$ MPa.

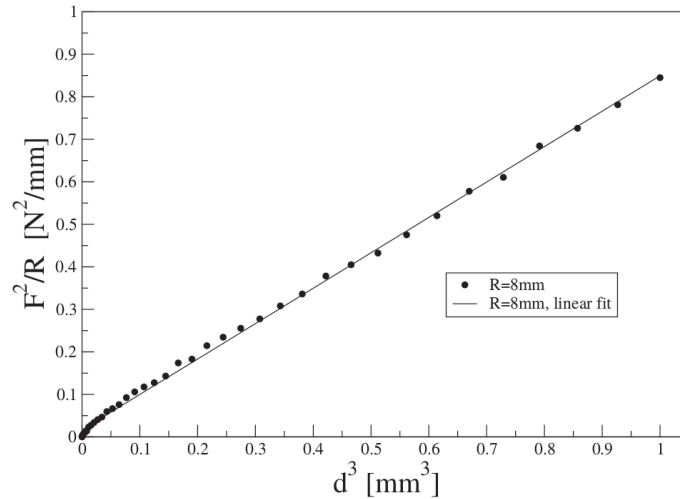


Figure 3.5: Hertzian force contact for a Polydimethylsiloxan (PDMS) sphere of radius 8mm. The linear fit to the $\frac{F^2}{R}$ vs d^3 data plot enables to calculate the Youngs's modulus for the measured material.

In case $\delta = \frac{d}{R}$ is inserted as the relative indentation into the equation the Hertzian contact law looks like

$$F(\delta) = \frac{4}{3}E^*R^2\delta^{\frac{3}{2}}. \quad (3.22)$$

The Hertzian contact law can be combined with the equation (see also equation 3.2 and 3.3):

$$I \propto \sin^2\left(\frac{C_s\pi}{\lambda}RF\right) \quad (3.23)$$

Where C_s is the stress-optical coefficient, λ is the wavelength of light and R is the thickness of the material. When substituting equation 3.22 into equation 3.23, we get a relation for the intensity:

$$I \propto \sin^2\left(R^3F\delta^{\frac{3}{2}}\right) \quad (3.24)$$

Fig. 3.6 show the comparison between the experimental measured (see section 3.4) mean intensity of a PDMS sphere (see subsection 3.3.1) with a diameter of $\varnothing = 8\text{mm}$ and the calculated mean intensity results for the calculation as described above. The sphere in the calculation have had the same parameter like diameter and Poissons ratio as the experimental sphere.

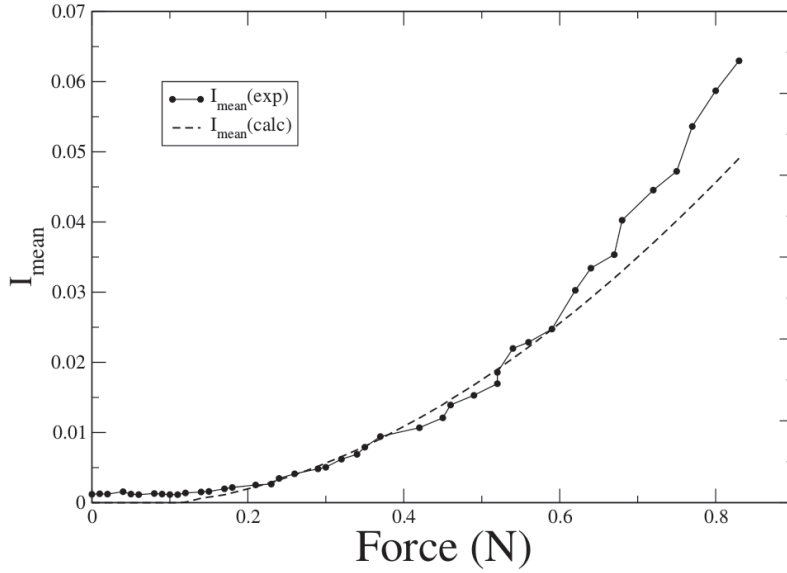


Figure 3.6: Comparison between experimental measured mean intensities for a stress birefringent sphere with a diameter of 8mm, and calculated intensity results. For both curves the same parameters like diameter, applied force and Poissons ratio of the material (PDMS) are valid.

3.2 Experimental Concept for the Determination of Mechanical Properties in Bidisperse Granular Packings

In this experiment the mechanical properties like the random close packing transition density $\varphi_{rcp}(\delta, \hat{x}_B)$ from a loose to a dense bidisperse granular system or the inner stress development during compaction in three dimensional granular packings are investigated. As discussed in section 3.1.1, a very convenient way to measure these properties is to use the stress birefringent technique. An appropriate polarizer setup, as described in section 3.1.2, should be implemented in a way that makes it possible to take images of the stress-optical signal of the sample for different packing fractions. The number of particles in the packing should be as large as possible to reduce finite size effects and provide a good statistics.

3.3 Stress Birefringent Materials

A great variety of materials shows stress birefringence such as glass and several transparent plastics. The material used in the present experiment needs to fulfill certain requirements. In order of priority the requirements are:

- The material has to be transparent and needs to show stress birefringent behavior.
- Spherically shaped particles with different sizes consisting of stress birefringent material are necessary.
- The material needs to be processed without producing frozen in stresses. Frozen-in stresses remain permanently in the material and thus change the way the stress tensor σ reacts to external forces. The stress tensor is a non-additive quantity and it is very complicated to extract the stresses caused by external forces even if frozen-in stresses are known.
- The particles have to be resistant against index matching fluids (e.g. frozen-in stresses can be caused by index matching fluids).
- The particles have to be sufficiently stiff that means the deformation of the particles caused by the inter-particle forces stays linear, hence reversible, during compaction and decompaction.

After several pilot tests with different materials a PDMS-elastomer from Dow Corning SYLGARD company described in section 3.3.1 was chosen. This silicone turned out to be the best compromise to fulfill the requirements described above. Together with Peidong Yu and Matthias Sperl we submitted a patent on this subject [42].

3.3.1 Particle Production

The 184 Silicone Elastomer KIT from Dow Corning SYLGARD company was used as raw material. This is a Polydimethylsiloxan (PDMS), which means a polymer based on silicone (see Fig. 3.7).

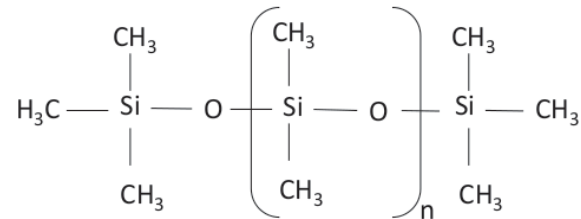


Figure 3.7: Chemical formula for Polydimethylsiloxan (PDMS). In brackets: monomer unit of the molecule with n repetitions

Due to the nonpolar character of the CH_3 methyl group at the end of each anorganic chain, PDMS has a low surface energy. Consequently, the molecule is a hydrophobic substance. Furthermore PDMS is chemically inert against salt (NaCl). These two properties make PDMS processable for a water and saltwater based production method described in the following.

3.3.2 Water Based Production Method

The basic concept of this sphere production method is the density difference between pure water (H_2O) and Saltwater ($\text{H}_2\text{O} + \text{NaCl}$). The density of H_2O is $\rho \approx 1$ and ρ of a saturated salt solution is $\rho \approx 1.359$ at 25°C . The density of PDMS has a value of $\rho \approx 1.05$ measured with the pycnometer AccuPyc II 1340 V1.05 from the *micromeritics*[®] company consequently PDMS sinks in pure H_2O and floats on a saturated $\text{H}_2\text{O} + \text{NaCl}$ solution. If H_2O and a $\text{H}_2\text{O} + \text{NaCl}$ solution is now layered on top of each other in one box a diffusion layer is formed. This diffusion layer has two advantages for producing spherical particles

- the density gradient of the diffusion layer supports the surface tension of PDMS to form a sphere
- the diffusion layer is stable for several hours and can keep the PDMS during the hardening process, which takes typically 12 hours at 25°C .

Diffusion

Diffusion is the transport of mass on the atomic scale and it can, for instance, be driven by gradients in composition and/or gradients in density. The diffusion in our case is driven by the gradient in composition (or chemical diffusion) as long as the salt solution is in gravitational direction lower than the pure water. Otherwise diffusion would be gravitationally and chemically driven [43].

If we assume a unit area of a plane perpendicular to the direction of diffusion per unit time the flux of mass passing through the area is described by Fick's first law:

$$J = -D \frac{\partial c}{\partial z}, \quad (3.25)$$

where c is the concentration of mass and D the diffusion coefficient. The continuity equation of mass is described by

$$\frac{\partial c}{\partial t} = -\frac{\partial J}{\partial z} \quad (3.26)$$

and gives us in combination with equation 3.25 Fick's second law:

$$\frac{\partial c}{\partial t} = D \frac{\partial^2 c}{\partial z^2}. \quad (3.27)$$

Solutions of the equation 3.27 depend on the boundary and initial conditions of each specific problem. Furthermore, note that D in equation 3.25 and 3.27 has to be independent of the concentration.

Fig. 3.8 shows a PDMS sphere with 10mm in diameter imbedded in the diffusion layer (left). To the right the density gradient depending on diffusion $\rho(C(z, t))$ is plotted for three different times. The black curve shows a density profile after 1 second of diffusion. The red curve shows the density profile after 12 hours diffusion time and the green line indicates the density profile after 14 days of diffusion. The green curve illustrates the situation when the PDMS sphere starts floating. The length scale in both pictures are the same and the black dot indicates the height and density position of the sphere. The plot in Fig. 3.8 shows that the density gradient is not vanishing during the hardening process of PDMS, which typically takes 12 hours at 25°C (note that only the chemical diffusion is calculated!).

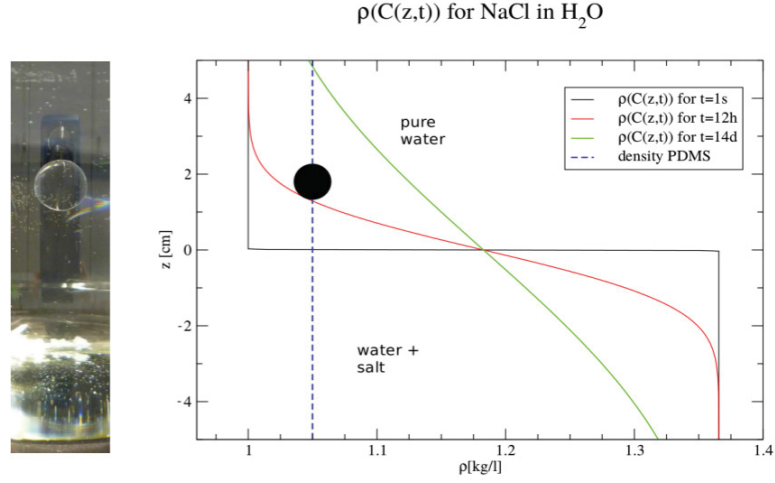


Figure 3.8: Density distribution of $NaCl$ in H_2O depending on diffusion calculated for three diffusion times. Left: PDMS sphere with $\varnothing \approx 13\text{mm}$ imbedded in a diffusion layer of $NaCl$ in H_2O . Right: density profile depending on the concentration of $NaCl$ for three different diffusion time intervals. The scales of the z -axes in both the picture and the plots are the same.

In the following the solution for the density distribution depending on diffusion shown in Fig. 3.8 is presented. The reservoir of the $H_2O + NaCl$ solution at the bottom and H_2O on top can be considered as infinity comparing to the height of the diffusion layer. Hence, the concentrations at the opposite far ends of the liquids stays constant during production time. For our specific problem [44] provides a solution of Fick's second law.

Fortunately, the density of a salt solution depends linearly on the amount of $NaCl$ dissolved in H_2O . Hence, we are able to calculate the density $\rho(C(z,t))$ for the diffusion layer depending on the concentration of $NaCl$ in the layer with:

$$\rho(C(z,t)) = MC(z,t) + \rho_0 \quad (3.28)$$

The concentration of $NaCl$ in the diffusion layer is defined by

$$C(z,t) = \frac{C_{NaCl}}{2} + \frac{C_{NaCl}}{2} \operatorname{erf} \left\{ \frac{z - z_0}{\sqrt{4Dt}} \right\} \quad (3.29)$$

where $C(z,t)$ is concentration in the diffusion layer, which is dependent on the position in z -direction and time. C_{NaCl} is the initial concentration of salt in the $H_2O + NaCl$ solution and D is the diffusion coefficient of

salt in water. The center of the diffusion profile is specified by z_0 and erf denotes the error function.

To be able to calculate $\rho(C(z, t))$, we need to determine the necessary constants: D is the diffusion coefficient of salt in water, C_{NaCl} is the concentration of $NaCl$ in H_2O , M is the constant of proportionality, and ρ_0 is the initial density of water.

When pouring a salt crystal into water the $NaCl$ molecule separates into a Na^+ -ion and a Cl^- -ion and the diffusion of the $NaCl$ molecule is dependent on the diffusion coefficient of each ion. The diffusion coefficients for Na^+ and Cl^- have not the same value but the numbers can be combined to a diffusion coefficient for salt in water. D_{NaCl} can be calculated from the diffusion coefficients D_{Na^+} and D_{Cl^-} for the single ions with equation [45]:

$$D_{NaCl} = \frac{(z_+ + |z_-|)D_{Na^+}D_{Cl^-}}{z_+D_{Na^+} + |z_-|D_{Cl^-}} \quad (3.30)$$

where $z_{+/-}$ is the charge on the ions. The diffusion coefficients at 25°C are $D_{Na^+} = 1.334 * 10^{-5} \frac{cm^2}{s}$ and $D_{Cl^-} = 2.032 * 10^{-5} \frac{cm^2}{s}$. D_{NaCl} can be calculated applying the equation 3.30:

$$D_{NaCl} = 1.6106 * 10^{-5} \frac{cm^2}{s}.$$

When dissolving solid $NaCl$ in water, the concentration in units of mass fraction C_{NaCl} can be defined as:

$$C_{NaCl} = \frac{m_{NaCl}}{m_{NaCl} + m_{H_2O}}. \quad (3.31)$$

where m is the mass of each component. To prepare a saturated salt solution one needs to stir 359g of $NaCl$ in one liter of H_2O at 25°C. The dissolved ions do not significantly increase the volume of the solvent. The concentration of 359g $NaCl$ in one liter of water in units of mass fraction is:

$$C_{NaCl} = \frac{359g}{359g+1000g} = 0.26.$$

The constant of proportionality M can be calculated by

$$M = \frac{\rho_{NaCl+H_2O} - \rho_{H_2O}}{C_{NaCl}} = \frac{0.36}{0.26} = 1.38. \quad (3.32)$$

With $z_0 = 0$ and $\rho_0 = 1$ for H_2O we can calculate the density profile with equation 3.28 and the results are shown in Fig. 3.8.

Applying this method spheres with five different diameters were produced. Table 3.1 lists the existing spheres.

<i>spheretype</i>	\varnothing [mm]	$\Delta\varnothing$ [mm]	<i>#spheres</i>
a	2.4	± 0.1	6200
b	4	± 0.1	1900
c	5	± 0.1	1000
d	6	± 0.1	600
e	13	± 0.1	50

Table 3.1: List of PDMS spheres produced by Water Based Production Method. The diameter of the sphere is determine via individual measurements with a caliper.

Table 3.2 shows which kind of size ratios δ are mixable from the sphere types of Table 3.1.

	a	b	c	d	e
a	1	0.6	0.48	0.4*	0.18*
b		1	0.8	0.67	0.3*
c			1	0.8*	0.38
d				1	0.46
e					1

Table 3.2: Possible size ratios δ mixable with the spheres listed in Table 3.1.

The size ratios δ marked with "*" in Table 3.2 are the basis for investigating mechanical properties of dense packed granular systems. In particular, packings with size ratios $\delta = 0.18$, $\delta = 0.4$, $\delta = 0.3$ and $\delta = 0.8$ are measured.

Fig. 3.9 shows some PDMS spheres immersed in a $H_2O + NaCl$ diffusion layer during the hardening process. Fig. 3.10 gives an overview about the produced sphere sizes (left) and shows an accumulation of ≈ 2500 spheres with diameter $\varnothing 2.4$ mm (right)



Figure 3.9: PDMS spheres imbedded in a diffusion layer of $H_2O+NaCl$ during the hardening process. Seven spheres with a diameter of $\varnothing 6mm$ and one sphere with a diameter of $\varnothing 13mm$ are visible.

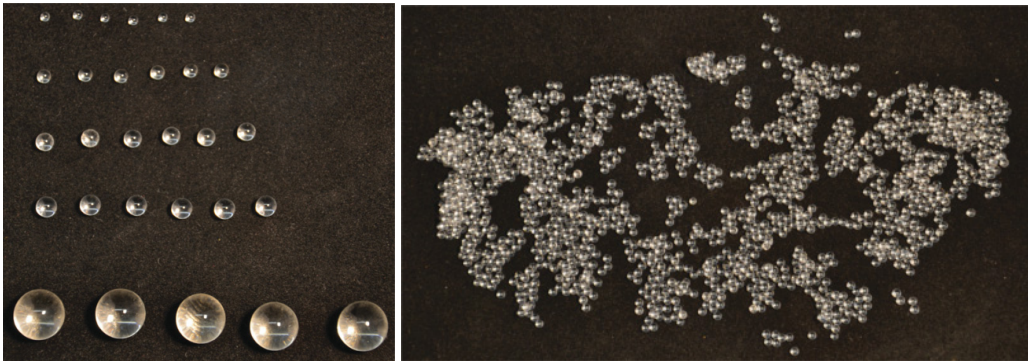


Figure 3.10: Detailed view of some produced spheres with diameter of $\varnothing 2.4mm$, $\varnothing 4mm$, $\varnothing 5mm$, $\varnothing 6mm$ and $\varnothing 13mm$ (left) respectively and an accumulation of ≈ 2500 spheres with diameter $\varnothing 2.4mm$ (right)

3.4 Experimental Setup

An apparatus is designed that makes it possible to measure and adjust packing properties like packing density, overall pressure and light intensity with a very accurate resolution. Fig. 3.11 show the setup.

A micrometer screw at the bottom of the machine (not visible in Fig. 3.11) can adjust the volume of the sample and another micrometer screw (see (5) in Fig. 3.11) can adjust the angle of the sample to achieve an aligned optical light path. From the top the overall pressure can be measured with a *Chatillon*[®] force gauge (see (7) in Fig. 3.11), which has a range from 0 – 50N and a resolution of two decimal places. For measuring the intensity a circular polariscope as described in section 3.1.2 is in use. The polariscope contains the following components all visible in Fig. 3.11: a light source with a green LED panel (3), the first circular polarizer (4), the sample container (1), and a Nikon D3 camera (2) with a second circular polarizer (6) in front of a 60mm focal length objective. The sample container is a $5 \times 5 \times 5 \text{ cm}^3$ glass cube (1).

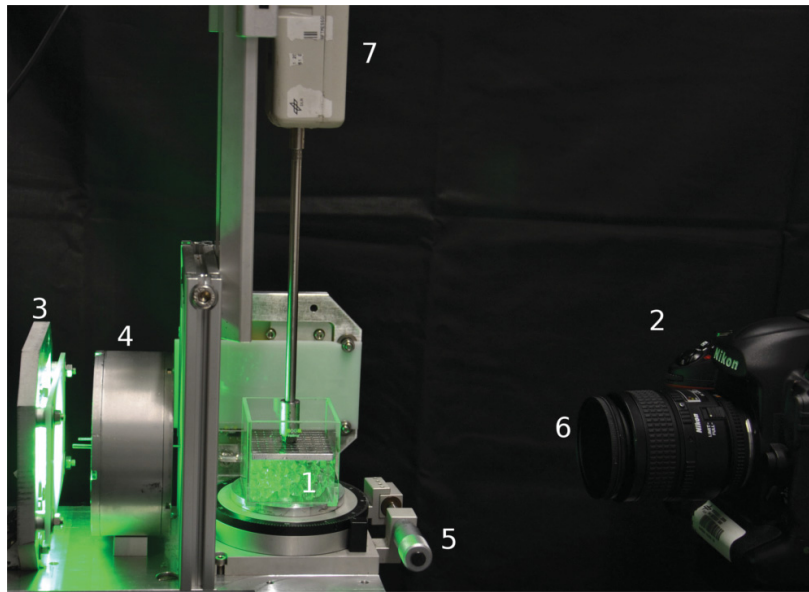


Figure 3.11: Experimental setup for 3D stress birefringence packing experiments. (1) sample container containing dry not index matched spheres, (2) Nikon D3 camera, (3) light source containing a green LED light panel, (4) circular polarizer, (5) micrometer screw for angle adjustment, (6) circular polarizer in front of a camera objective with 60mm focal length, (7) *Chatillon*[®] force gauge

Index Match for Transparent Spheres

The images taken by the Nikon D3 camera (2) in Fig. 3.11 are the basis for analyzing the light intensity passing through the polariscope. Therefore it is essential that no refraction is induced during measurement. To avoid these effects it is necessary to surround the spheres by a background liquid, which has the same index of refraction as the spheres. This procedure is called index matching.

The idea to achieve the same index of refraction as the spheres is rather simple: Two liquids, one with a higher index of refraction and one with a lower index of refraction as the particles are being mixed together and varying their mixing ratio until the desired index of refraction is achieved. Note that the liquids being used are not aggressive in the sense that they are not inducing frozen-in stresses to the particle material. PDMS spheres have an index of refraction of 1.4118. Water with an index of refraction of 1.333 and glycerol with an index of 1.4729 were used in the present experiment for index matching. The mixing ratio is 44% water and 56% glycerol in mass%.

Water has a density of $\rho_{water} = 1 \frac{g}{cm^3}$ and glycerol of $\rho_{glycerol} = 1.261 \frac{g}{cm^3}$. With the previously mentioned mixing ratio the resulting liquid has a density of $1.146 \frac{g}{cm^3}$. As a consequence the PDMS spheres with a density of $1.05 \frac{g}{cm^3}$ are slightly floating. Fig. 3.12 shows the difference between a dry and an index matched sample.

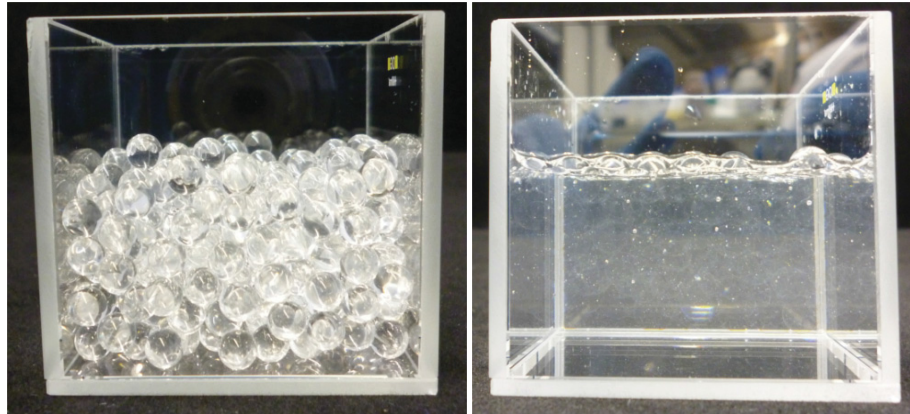


Figure 3.12: PDMS spheres in a glass container with and without index matching liquid. Left picture: dry sample container with ≈ 350 PDMS spheres of diameter $\varnothing 6\text{mm}$. Right picture: same spheres as shown on the left side in an index matched environment of $\approx 44\%$ pure water and $\approx 56\%$ glycerol.

3.4.1 Operation of Experiment

Packings with four different size ratios δ , which are marked with a "*" in Table 3.2, are investigated in the present experiment. Table 3.3 gives an overview of the performed mixing ratios \hat{x}_B for each size ratio δ .

size ratio δ	mixing ratio \hat{x}_B
0.18	0; 0.1; 0.2; 0.3; 0.35; 0.38; 0.39; 0.42; 0.43; 0.44; 0.45; 0.46; 0.47; 0.49; 0.5; 0.6; 0.7; 0.8; 0.9; 1
0.3	0; 0.1; 0.2; 0.3; 0.35; 0.38; 0.4; 0.42; 0.43; 0.434; 0.44; 0.45; 0.454; 0.46; 0.47; 0.5; 0.6; 0.7; 0.8; 0.9; 1
0.4	0; 0.1; 0.2; 0.28; 0.38; 0.4; 0.42; 0.44; 0.46; 0.48; 0.5; 0.6; 0.7; 0.8; 0.88; 1
0.8	0; 0.1; 0.2; 0.3; 0.4; 0.5; 0.6; 0.7; 0.8; 0.9; 1

Table 3.3: List of size ratios δ and mixing ratios \hat{x}_B for the 3D stress birefringent experiment.

A measuring procedure starts with preparing the specific number of particles for each mixing ratio \hat{x}_B by weighting the two components A and B (A stands for the big spheres and B for the small ones). After inserting the correct amount of A and B in the sample container, the sample needs to be index matched (see Fig. 3.12). A homogeneous mixing ratio \hat{x}_B of the components A and B is achieved by carefully mixing the spheres using a stirring stick. The slightly floating property of the spheres in the liquid prevents the packing from sedimenting and keeps it in a loose state until the packing fraction increases to the transition point φ_{rcp} . The measurement starts at a packing fraction of $\varphi_0 \approx 0.6$ and it increases between $\Delta\varphi \approx 0.002$ and $\Delta\varphi \approx 0.01$ per step depending on the protocol. The measurement ends when the overall light intensity has reached a certain brightness, which makes it obvious that the transition has already happened. For each step one stress-optical image is taken by the Nikon D3 camera (see (2) in Fig. 3.11). Due to the liquid environment and the smooth surface of the PDMS material, the sphere to sphere interaction has low influence of friction. At some packing fraction the system starts to show force chains percolating through the system. This behavior indicates that the granular system passes the transition from a loose to a dense packing. Fig. 3.13 visualize a typical experimental run.

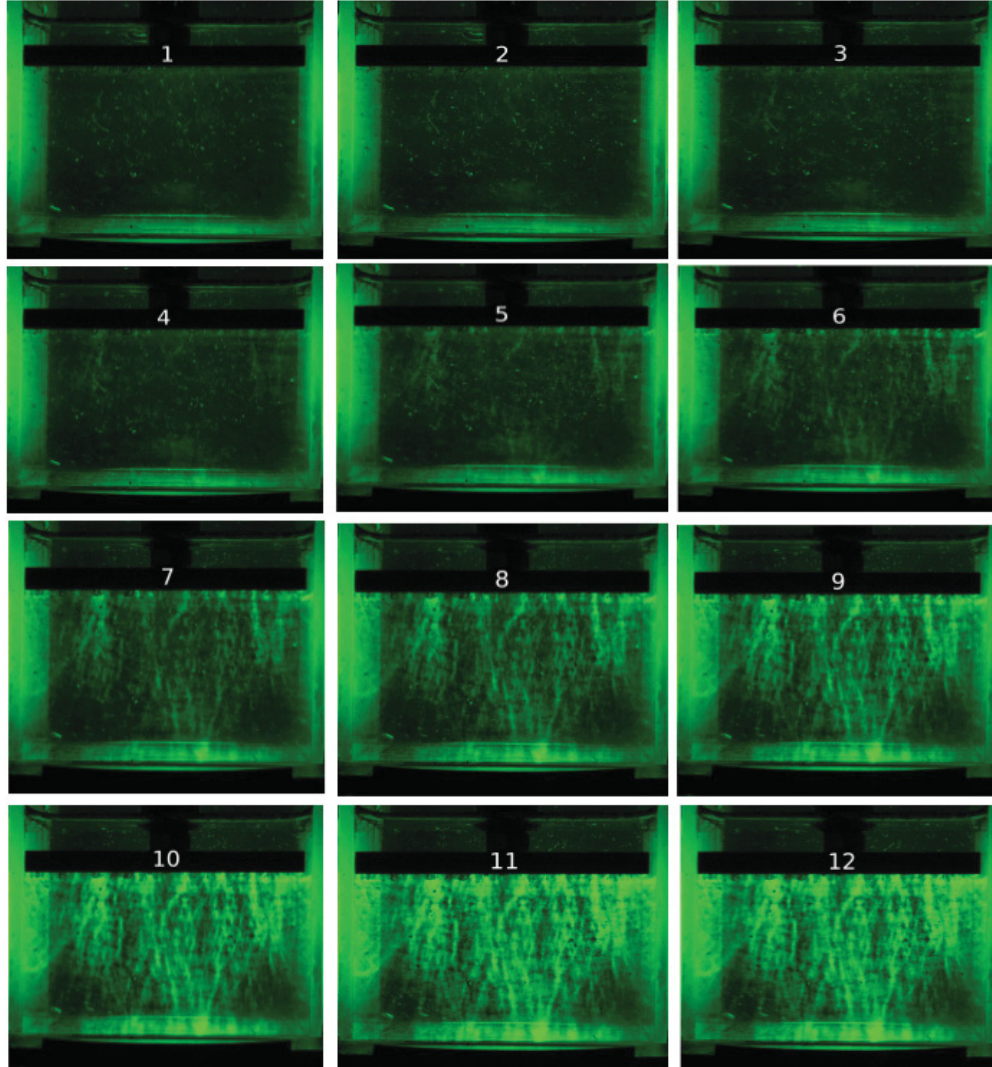


Figure 3.13: Typical picture series (1-12) from a stress birefringent measurement run. A packing with a size ratio of $\delta = 0.4$ and mixing ratios of $\hat{x}_B = 0.38$ is shown. The random close packing transition happens between picture (5) and (6) at a packing fraction of $\varphi_{rcp} \approx 0.676$ (see also results in chapter 3.5.1). Packing fractions for the pictures are $\varphi_{(1)}=0.649$; $\varphi_{(2)}=0.656$; $\varphi_{(3)}=0.663$; $\varphi_{(4)}=0.667$; $\varphi_{(5)}=0.674$; $\varphi_{(6)}=0.676$; $\varphi_{(7)}=0.68$; $\varphi_{(8)}=0.685$; $\varphi_{(9)}=0.689$; $\varphi_{(10)}=0.692$; $\varphi_{(11)}=0.697$; $\varphi_{(12)}=0.704$.

Three compression cycles are performed for each mixing ratio \hat{x}_B to provide some statistical information. The pictures can be evaluated by an image processing computer code.

3.4.2 Volume and Intensity Detection

For volume and intensity detection an image processing algorithm which is written in C++ was used. In order to avoid solving the distortion problem for the taken images [46] a value ξ is defined which can be determined by four characteristic points of each image.

Fig. 3.14 shows an exemplary calibration picture for a height of 23mm. The characteristic points A, B, C and D can be detected by the image processing algorithm (see also blue points in Fig. 3.17) and ξ is defined as $\xi = \frac{(AD+BC)}{AB}$.

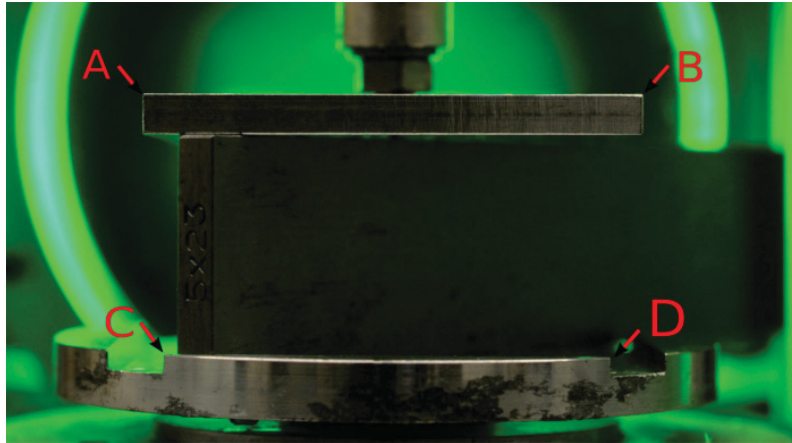


Figure 3.14: Reference for calibration with a height of 23mm. Characteristic points A,B,C, and D can be detected via an image processing algorithm.

In Fig. 3.15 a fit for different calibration heights in order to optimize the height detection for the image processing is shown.

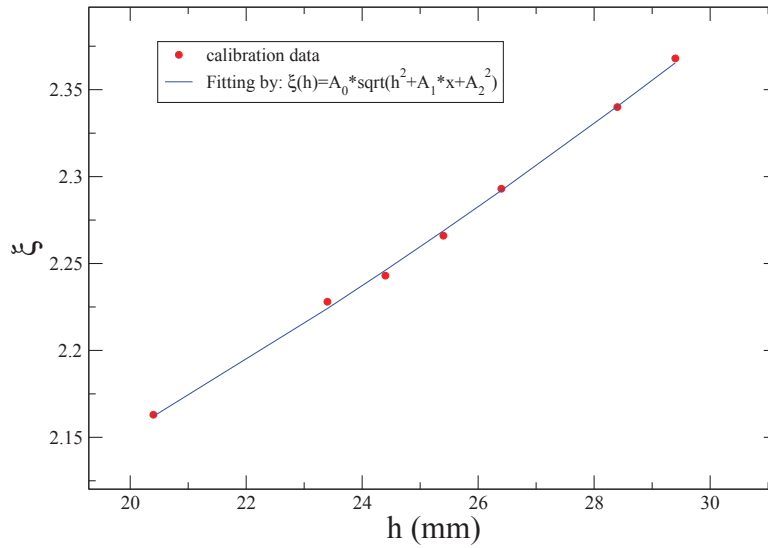


Figure 3.15: Height calibration. The black line shows $\xi(h)$ fitted to the calibration measurements. Every black dot stands for a height h , which was adjusted by spacers.

Fig. 3.16 is a raw image of the experiment taken by the Nikon D3 camera.

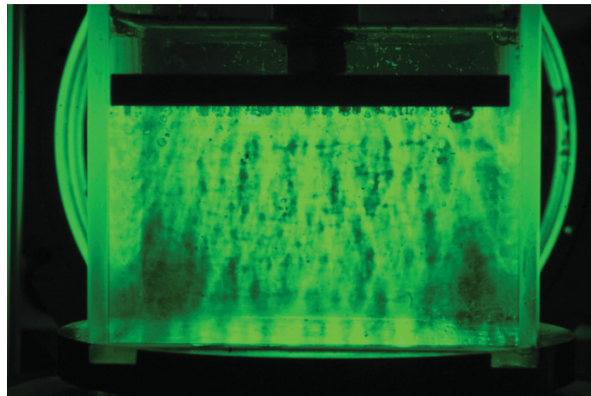


Figure 3.16: Raw image of the experiment for determine the φ_{rcp} density. The picture show a packing with parameter: size ratio $\delta = 0.4$, mixing ratio $\hat{x}_B = 0.42$ and is compressed by a pressure of ≈ 16.2 kPa.

In Fig. 3.17 a typical image processed by the image processing algorithm is shown. The algorithm is working as described in the following. The first step is to convert the colored raw data into a gray value image. In the present experiment a green LED light source is used. Hence the rgb raw data show negligible fraction of red and blue colors. For gray scaling the algorithm ignores red and blue and converts the green values in a gray shade. The Second step is to select the corners of the characteristic points A,B,C and D using a self made corner detection program based on a Sobel filter (see [46]). The third step is the selection of the area (see (5) in Fig. 3.17) where the mean intensity is to be calculated. This area is manually chosen for every experimental run once in order to avoid the detection of scattered light, artifacts like bubbles, mirror effects from the container walls and exclude finite size effects.

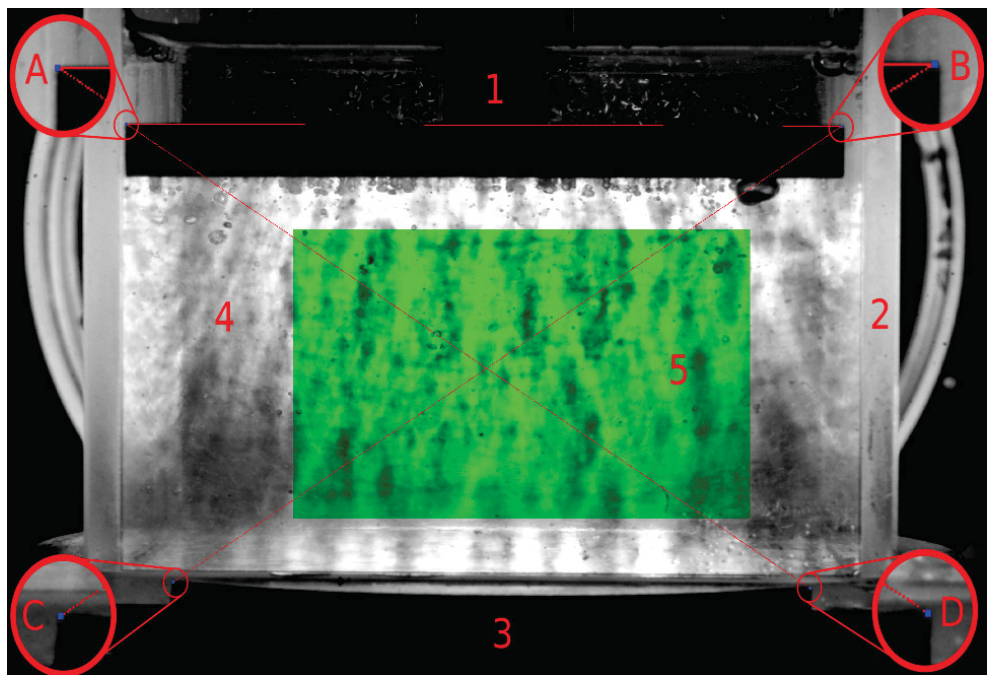


Figure 3.17: Image processed by the image processing algorithm (same image as shown in Fig. 3.16) In close-up views the selected corners A,B,C,D (blue dots) are shown

- 1: top of the sample cell connected to the *Chatillon*[®] force gauge
- 2: sample container
- 3: base plate of the experiment
- 4: particles
- 5: selected area for mean intensity determination (green)

3.4.3 Stress-Optical Analysis I

The mean intensity value $I_{mean} = \frac{\sum grayvalue}{\sum pixel}$ is determined for the selected area ((5) in Fig. 3.17) of each image. In Fig. 3.18 the intensity values for three different runs are plotted.

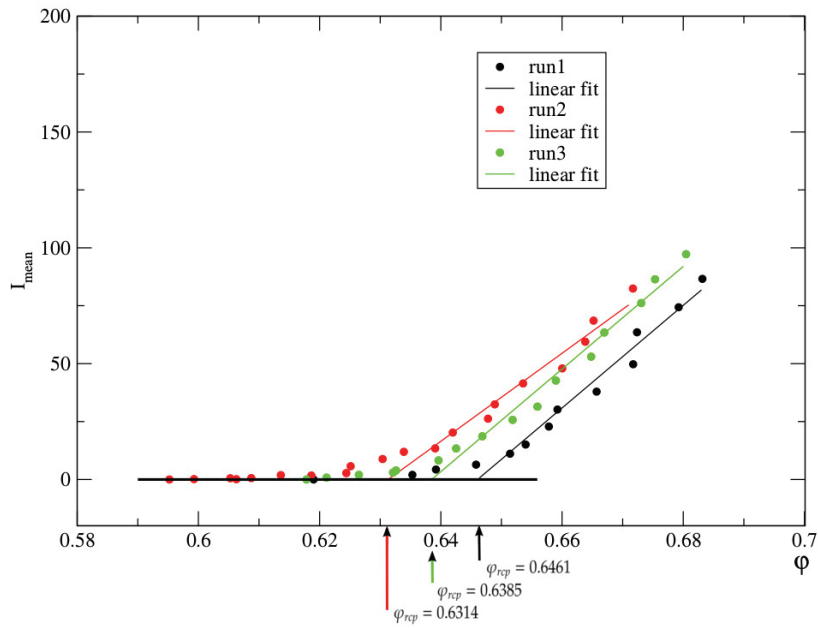


Figure 3.18: Mean intensity plot for three different experimental runs with size ratio $\delta = 0.4$ and mixing ratio $\hat{x}_B = 0.88$. The intersection of the linear fit with the background level indicates the transition density φ_{rcp} . In particular it is for run1: $\varphi_{rcp} = 0.6461$, run2: $\varphi_{rcp} = 0.6314$ and run3: $\varphi_{rcp} = 0.6385$.

Three different sections can be distinguished from the plots in Fig. 3.18. For low densities φ the intensity is almost zero (here the background intensity is already subtracted). When increasing φ , at some point the mean intensity starts to grow slowly. By further increasing φ the growth becomes linear. The packing fraction where the fit line intersects the background level is considered to be φ_{rcp} . Note that for steeper increases of the mean intensity values after φ_{rcp} an overestimation of the transition density could be determined. For every mixing ratio \hat{x}_B three runs are performed in experiment and the mean value $\varphi_{rcp_{mean}} = \frac{\varphi_{rcp_{run1}} + \varphi_{rcp_{run2}} + \varphi_{rcp_{run3}}}{3}$ gives the transition density for this particular mixing ratio \hat{x}_B . The values $\varphi_{rcp_{run1}}$, $\varphi_{rcp_{run2}}$ and $\varphi_{rcp_{run3}}$ give the error distribution for $\varphi_{rcp_{mean}}$ and are shown in the resulting diagrams as black, red and green dots, respectively.

3.4.4 Stress-Optical Analysis II

In the second analysis of the stress optical signal measured as described in section 3.4.1 the slope η of the increasing mean intensity after φ_{rcp} is analysed. The procedure for analyzing the data is comparable to the approach described in subsection 3.4.3. The mean slope η_{mean} is calculated as $\eta_{mean} = \frac{\eta_{run1} + \eta_{run2} + \eta_{run3}}{3}$ from the measurements run1, run2 and run3 respectively. The values η_{run1} , η_{run2} and η_{run3} give the error distribution for η_{mean} and are shown in the resulting diagrams as black, red and green dots respectively. In Fig. 3.19 the procedure is illustrated.

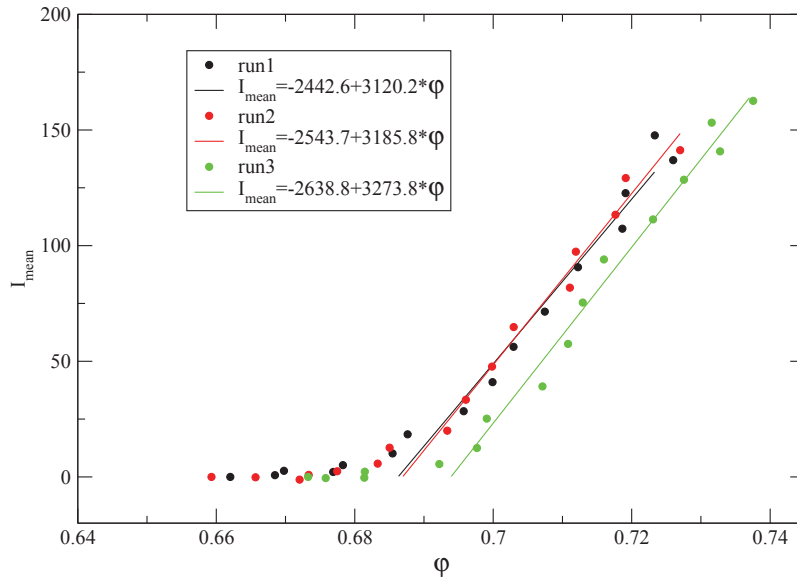


Figure 3.19: Mean intensity plot for three different experimental runs with size ratio $\delta = 0.4$ and mixing ratio $\hat{x}_B = 0.48$. The increasing mean intensity after φ_{rcp} is fitted by a linear law. The slope of this line is analyzed for two different size ratios $\delta = 0.18$ and $\delta = 0.4$ and different mixing ratios \hat{x}_B .

3.5 Results

3.5.1 Results for Packing Fraction $\varphi_{rcp}(\hat{x}_B)$ Measurements

Packings with four different size ratios $\delta = 0.18$, $\delta = 0.3$, $\delta = 0.4$ and $\delta = 0.8$ and different mixing ratios \hat{x}_B are experimentally performed. The results are shown in the figures 3.20, 3.21, 3.22 and 3.23. The plotted

mean values in Fig. 3.20, 3.21, 3.22 and 3.23 are connected with a black dashed line. The error bars with black, red and green dots represent the deviation of the transition density $\varphi_{rcp,mean}$ for run1, run2 and run3 respectively. For some mixing ratios one error point in the error bar is missing (e.g. for $\delta = 0.4$ with a $\hat{x}_B = 0.37$), due to not detectable edges from the analysis software. All data are listed in Table A.1, A.2, A.3 and A.4.

In Fig. 3.20 the transition density progression for size ratio $\delta = 0.18$ is shown. The packing consists of big particles with diameter $\varnothing_A = 13\text{mm}$ and small particles with diameter $\varnothing_B = 2.4\text{mm}$. For $\hat{x}_B = 0$ the curve starts at a density φ_{rcp} lower than $\approx 55\%$ packing fraction and increase rapidly to a value of $\approx 63\%$ for $\hat{x}_B \approx 0.2$. Between $\hat{x}_B \approx 0.2$ and $\hat{x}_B \approx 0.4$ the transition density decreases and increases slightly. After $\hat{x}_B \approx 0.4$ the curve increases rapidly again until the maximum density of $\varphi_{rcp} = 0.7106$ for a mixing ratio $\hat{x}_B = 0.49$ is reached. From this maximum to the end of the curve the density values decrease monotonously until $\varphi_{rcp} = 0.6236$ at $\hat{x}_B = 1$ is reached.

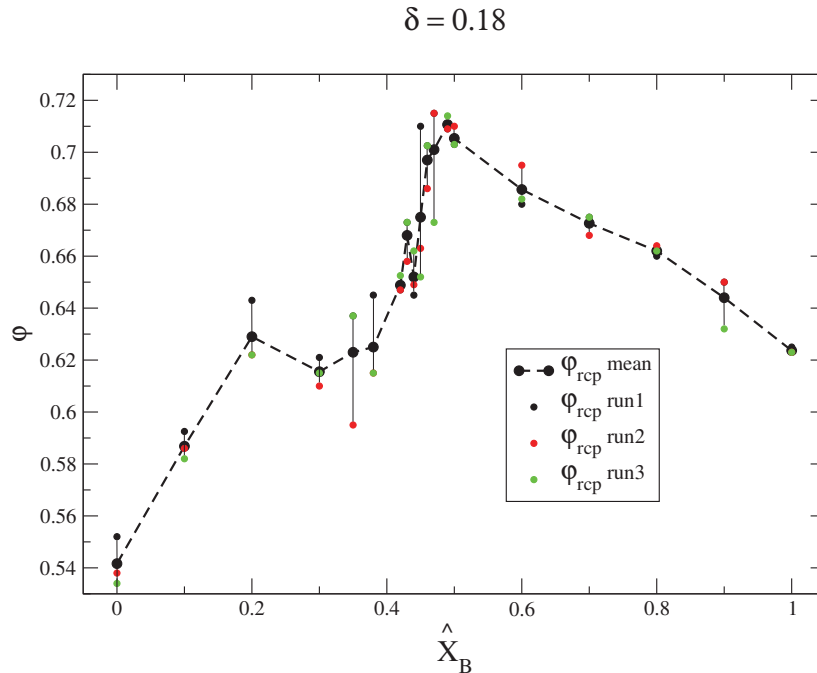


Figure 3.20: Random close packing transition density for a granular packing with size ratio $\delta = 0.18$. The measured packing consists of PDMS particles with diameters $\varnothing_A = 13\text{mm}$ and $\varnothing_B = 2.4\text{mm}$. The black dashed line connects the mean values.

The Fig. 3.21 show the data for size ratio $\delta = 0.3$ with particle diameter $\varnothing_A = 13\text{mm}$ and $\varnothing_B = 4\text{mm}$. For the first part of the curve between $\hat{x}_B = 0$ and $\hat{x}_B \approx 0.4$ the data increases strictly from $\varphi_{rcp} \approx 0.56$ to $\varphi_{rcp} \approx 0.7$. Between $\hat{x}_B \approx 0.4$ and $\hat{x}_B \approx 0.44$ the data exhibits a small jump in the transition density from $\varphi_{rcp} \approx 0.7$ to $\varphi_{rcp} \approx 0.72$. From $\hat{x}_B \geq 0.44$ to the last point at $\hat{x}_B = 1$ the curve decreases strictly to its ending point with a density of $\varphi_{rcp} \approx 0.64$.

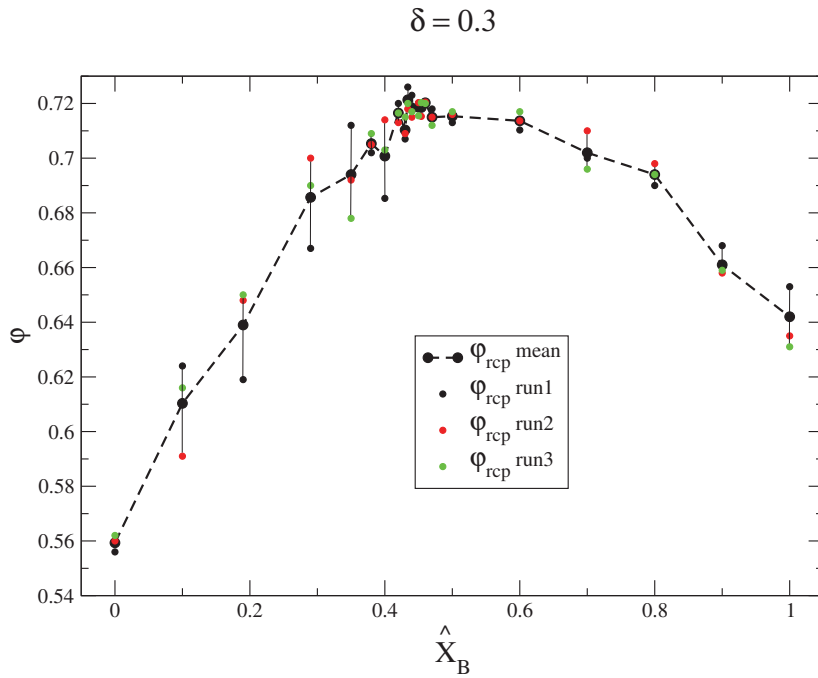


Figure 3.21: Random close packing transition density for a granular packing with size ratio $\delta = 0.3$. The measured packing consists of PDMS particles with diameter $\varnothing_A = 13\text{mm}$ and $\varnothing_B = 4\text{mm}$. The black dashed line connects the mean values.

The measured data for size ratio $\delta = 0.4$ with particle diameter $\varnothing_A = 6\text{mm}$ and $\varnothing_B = 2.4\text{mm}$ are visualized in Fig. 3.22. The curve starts with a packing density of $\varphi_{rcp} = 0.6276$. For increasing \hat{x}_B the curve growth slowly to its maximum point at $\hat{x}_B \approx 0.5$ with a density $\varphi_{rcp} = 0.687$ and decreases again to a density of $\varphi_{rcp} = 0.6256$ at $\hat{x}_B = 0.5$.

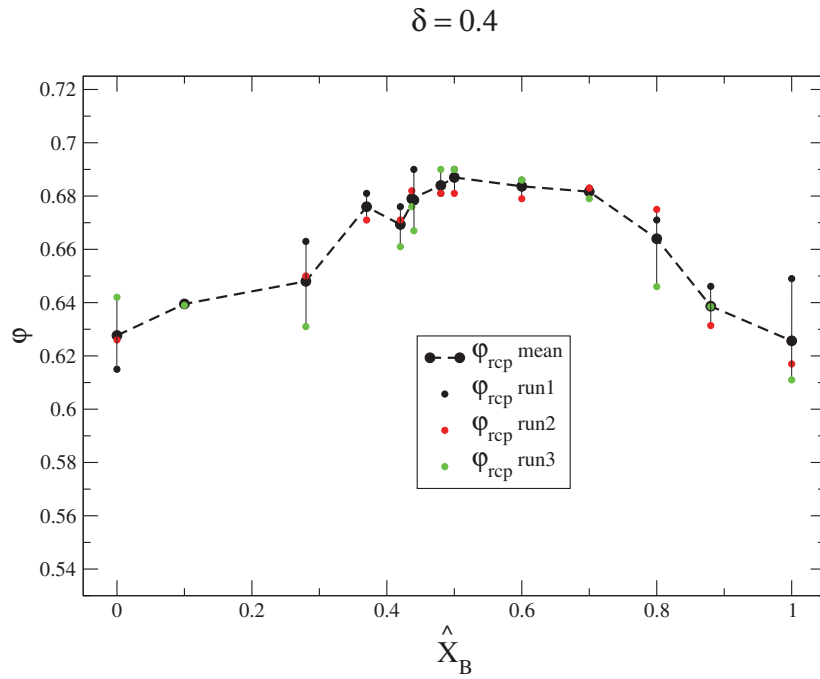


Figure 3.22: Random close packing transition density for a granular packing with size ratio $\delta = 0.4$. The measured packing consists of PDMS particles with diameter $\varnothing_A = 6\text{mm}$ and $\varnothing_B = 2.4\text{mm}$. The black dashed line connects the mean values.

In Fig. 3.23 the data for size ratio $\delta = 0.8$ with particle diameter $\varnothing_A = 5\text{mm}$ and $\varnothing_B = 4\text{mm}$ are presented. In contrast to the values shown in Fig. 3.20, 3.21 the curve in Fig. 3.23 shows no pronounced maximum.

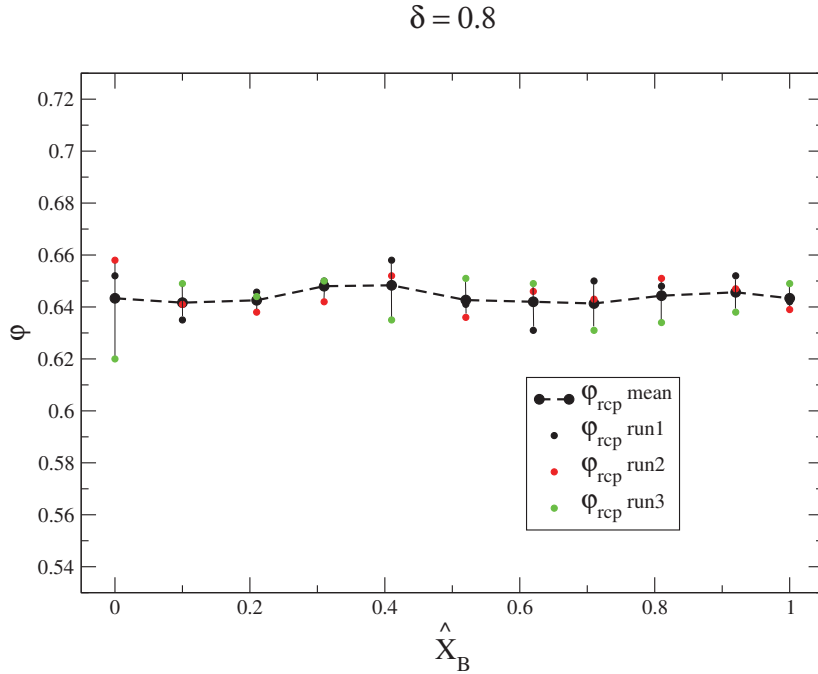


Figure 3.23: Random close packing transition density for a granular packing with size ratio $\delta = 0.8$. The measured packing consists of PDMS particles with diameter $\varnothing_A = 5\text{mm}$ and $\varnothing_B = 4\text{mm}$. The black dashed line connects the mean values.

3.5.2 Discussion

The first data points of the curves in Fig. 3.20 and 3.21 from $\hat{x}_B = 0$ to $\hat{x}_B \approx 0.2$ do not represent a packing with randomly distributed spheres. Due to the dimension of the sample container and the sphere sizes it is most likely that the measured values are subject to finite size effects (see section finite size effects 3.5.5). For example the first two points at $\hat{x}_B = 0$ and $\hat{x}_B = 0.1$ in Fig. 3.20 are measured based on a total number of particles $n_A = 42$; $n_B = 0$ and $n_A = 42$; $n_B = 728$ respectively (see also Table A.1 and A.2).

3.5.3 Results for the Slope η Analysis

As described in subsection 3.4.4 the slope η of the linear fit to the increasing part of the mean intensity curves is analysed. Data for

packings with size ratios $\delta = 0.18$ and $\delta = 0.4$ are analyzed for different mixing ratios \hat{x}_B .

Fig. 3.24 shows the results of the slope analysis for the packing with size ratio $\delta = 0.18$ (all values are listed in Table A.5). The curve shows two outliers for $\hat{x}_B = 0$ and $\hat{x}_B = 1$ (these values are in brackets) which are most likely caused by the influence of finite size effects (see discussion 3.5.5) and crystallization. The slope values from $\hat{x}_B = 0.1$ to $\hat{x}_B = 0.42$ creates a slightly increasing curve from $\eta_{mean} \approx 2940$ at $\hat{x}_B = 0.1$ to $\eta_{mean} \approx 2250$ at $\hat{x}_B = 0.42$. Between $\hat{x}_B = 0.42$ to $\hat{x}_B = 0.5$ a peak arises with its maximum $\eta_{mean} \approx 4160$ at $\hat{x}_B = 0.5$. For $\hat{x}_B \geq 0.5$ the slope values decreases strictly to the ending point at $\hat{x}_B = 0.9$ with a slope value of $\eta \approx 3200$.

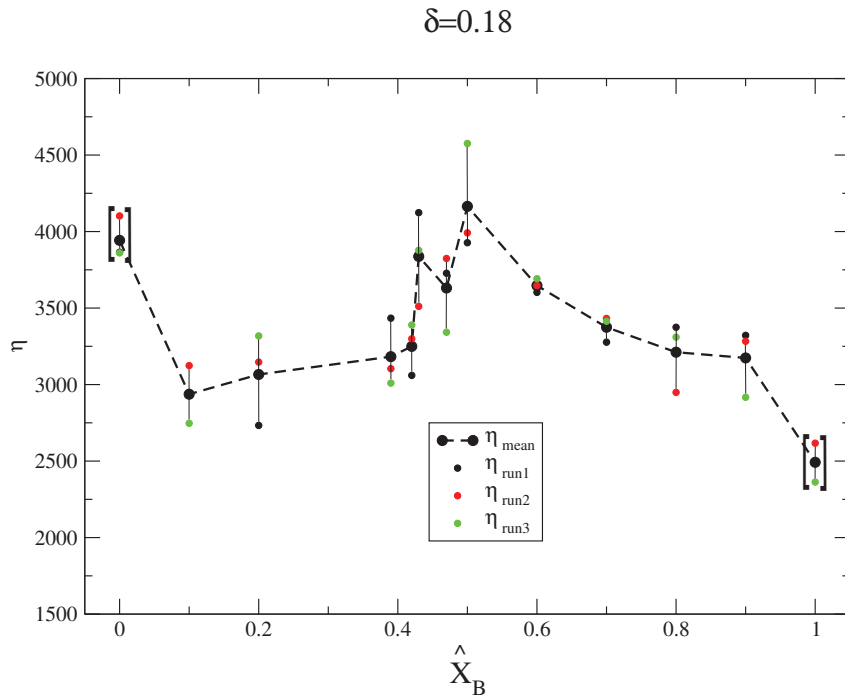


Figure 3.24: Mean intensity slope of the stress birefringent packing measurements. The data are measured based on a packing with size ratio $\delta = 0.18$. Data in brackets are outliers (see text).

Fig. 3.25 shows the results of the slope analysis for packings with size ratio $\delta = 0.4$ (all values are listed in Table A.6). The curve starts (from left to right) at a slope value $\eta_{mean} \approx 3300$ for $\hat{x}_B = 0$ and $\hat{x}_B = 0.1$. After a dip at $\hat{x}_B = 0.28$ with a slope value of $\eta_{mean} \approx 2950$ the curve

growth to its maximum $\eta_{mean} \approx 3460$. Then the curve levels again for $\hat{x}_B = 0.6$ and $\hat{x}_B = 0.7$ at $\eta_{mean} \approx 3300$. The slope values for $\hat{x}_B = 0.8$ and $\hat{x}_B = 0.9$ decreases monotonously to $\eta_{mean} \approx 3120$ and $\eta_{mean} \approx 2920$ respectively. In contrast to the curve in Fig. 3.24 the curve in Fig. 3.25 show no pronounced maximum. The last value for $\hat{x}_B = 1$ is shown in brackets to emphasize the influence of finite size effects and crystallization. Against a systematically argumentation the slope value for $\hat{x}_B = 0$ show no conspicuous behavior.

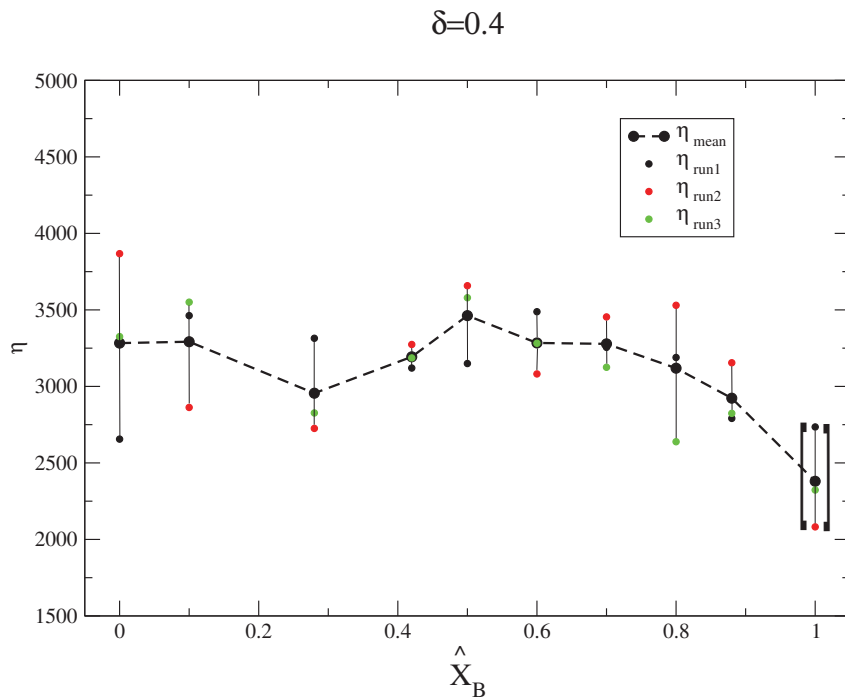


Figure 3.25: Mean intensity slope of the stress birefringent packing measurements. The data are measured based on a packing with size ratio $\delta = 0.4$. Data in brackets are outliers (see text).

3.5.4 Results for Bulk Modulus $\kappa(\hat{x}_B)$ Measurements

The experimental setup described in section 3.4 provides a pressure measurement for every volume fraction. With these values the bulk modulus $\kappa = -V \frac{dP}{dV}$ is calculated. To determine the derivative $\frac{dP}{dV}$ a straight line is plotted to the linear increasing pressure values after the rcp-transition, assuming that before the transition at φ_{rcp} the bulk

modulus κ is zero and after the transition κ has a finite constant value. From the slope of the fitted line the derivative value $\frac{dP}{dV}$ is calculated (see Fig. 3.26). The volume data which are used for bulk modulus analysis are the same as used in section 3.5.1 for determine the packing fraction. For volume calculation the mean volume from the fitted line (see Fig. 3.26) is used. In Fig. 3.27, 3.28, 3.29 and 3.30 the values for the calculated bulk modulus are shown. The mean values are calculated as $\kappa_{mean} = \frac{\kappa_{run1} + \kappa_{run2} + \kappa_{run3}}{3}$ and the values for the single runs serves as errors. In all diagrams for the bulk modulus results it stands out, that the error bars are mostly greater than the error bars in the diagrams for the transition densities (see Fig. 3.20 to 3.23). Furthermore some data points which are shown in the transition densities diagrams are missing in the diagrams for the bulk modulus analysis. The reason is that the measuring protocol was not initially optimized for measuring the bulk modulus, hence it was not possible to fit a reasonable linear function to all data series because of less measurement points after the rcp-transition.

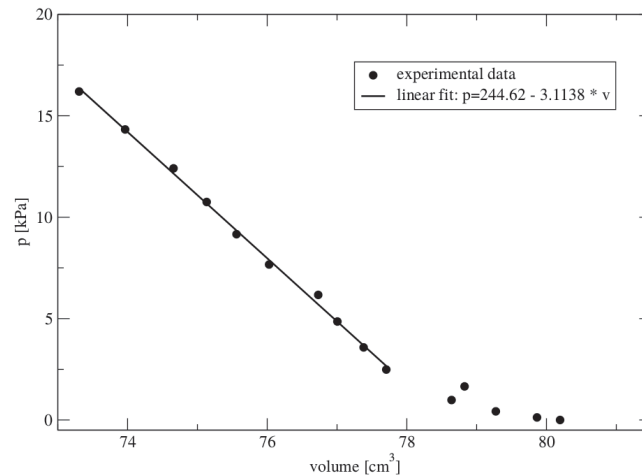


Figure 3.26: Linear fit to the experimental pressure data in order to determine the derivation for the bulk modulus calculations. The measured data are based on a granular packing with size ratio $\delta = 0.4$ and mixing ratio $\hat{x}_B = 0.042$.

Fig. 3.27 show the data for the calculated bulk modulus for packings with size ratio $\delta = 0.18$. The first data points until $\hat{x}_B \approx 0.2$ are based on packings with high influence of finite size effects (see also discussion in section 3.5.1). Although the data show comparable values for the bulk modulus on the outer ends of the curve (see also table A.7), the errors have a high deviation from its mean value. It is remarkable that the error bars for mixing ratios $\hat{x}_B \leq 0.5$ in the curves for size ratios $\delta = 0.18$

(see Fig.3.27) and $\delta = 0.3$ (see Fig.3.28) exhibits greater variations than the data for mixing ratios $\hat{x}_B > 0.5$. Also the data for size ratios $\delta > 0.3$ show smaller error bars.

The data exhibit a maximum at $\hat{x}_B \approx 0.7$ with $\kappa \approx 0.31MPa$. This means that the maximum bulk modulus is around 30% higher than for the starting and ending values.

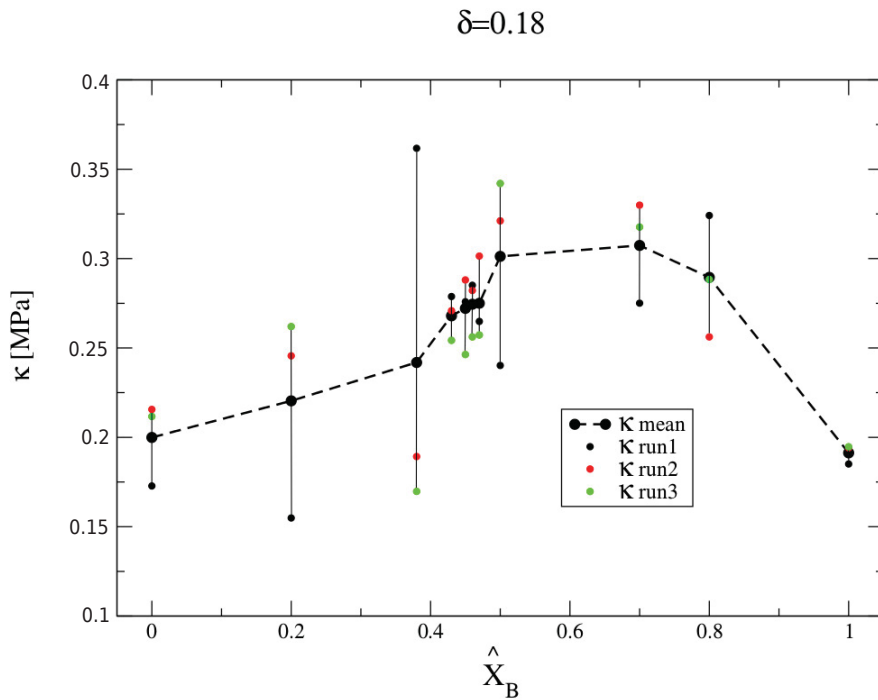


Figure 3.27: Bulk modulus determined for a granular packing with size ratio $\delta = 0.18$. The measured packing consists of PDMS particles with diameter $\varnothing_A = 13mm$ and $\varnothing_B = 2.4mm$. The black dashed line connects the mean values.

Fig. 3.28 present the bulk modulus data for size ratio $\delta = 0.3$. After a increasing progression until mixing ration $\hat{x}_B \approx 0.4$ a peak at $\hat{x}_B \approx 0.45$ with $\kappa \approx 0.32MPa$ appears (see also Table A.7). From $\hat{x}_B \approx 0.5$ until $\hat{x}_B = 0.6$ the curve decreases to $\kappa \approx 0.3MPa$ and does not change much until the end at $\hat{x}_B = 1$.

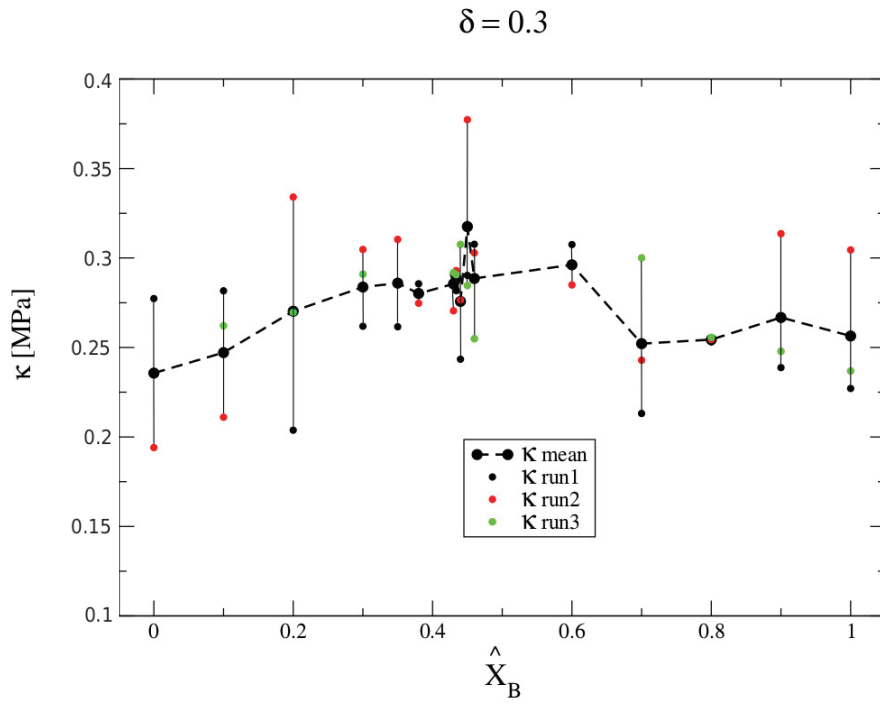


Figure 3.28: Bulk modulus determined for a granular packing with size ratio $\delta = 0.3$. The measured packing consists of PDMS particles with diameter $\varnothing_A = 13\text{mm}$ and $\varnothing_B = 2.4\text{mm}$. The black dashed line connects the mean values.

The bulk modulus data for packings with size ratio $\delta = 0.4$ are plotted in Fig. 3.29. Here the progression of the curve show an slowly increasing behavior until $\hat{x}_B = 0.8$ with $\kappa \approx 0.28\text{MPa}$ and decreases again to $\kappa \approx 0.24\text{MPa}$ at $\hat{x}_B = 1$ which is almost the same κ as for $\hat{x}_B = 0$ with $\kappa \approx 0.23\text{MPa}$.

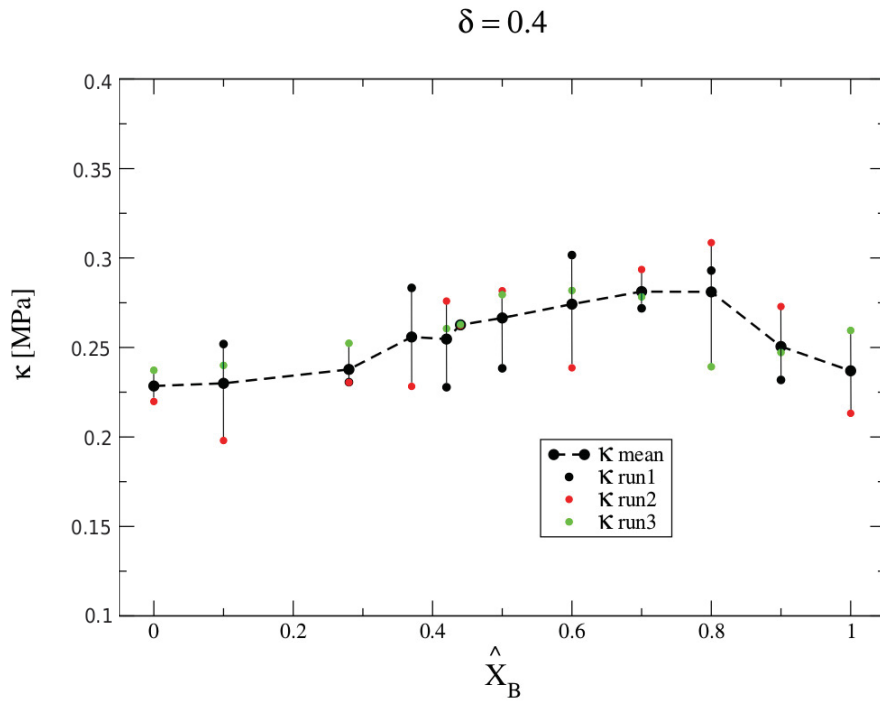


Figure 3.29: Bulk modulus determined for a granular packing with size ratio $\delta = 0.4$. The measured packing consists of PDMS particles with diameter $\varnothing_A = 6\text{mm}$ and $\varnothing_B = 2.4\text{mm}$. The black dashed line connects the mean values.

The last diagram for the bulk modulus (see Fig. 3.30) shows the data of a granular packing with size ratio $\delta = 0.8$. It starts with $\kappa \approx 0.2\text{MPa}$ at $\hat{x}_B = 0$ increases and decreases slightly until a small peak appears at $\hat{x}_B = 0.52$ with $\kappa \approx 0.21\text{MPa}$. Decreases and increases again to the end value $\kappa \approx 0.22\text{MPa}$ for $\hat{x}_B = 1$. In the range of the error bars the curve shows no significant maximum or peak such as the curves in Fig. 3.27, 3.28 and 3.29.

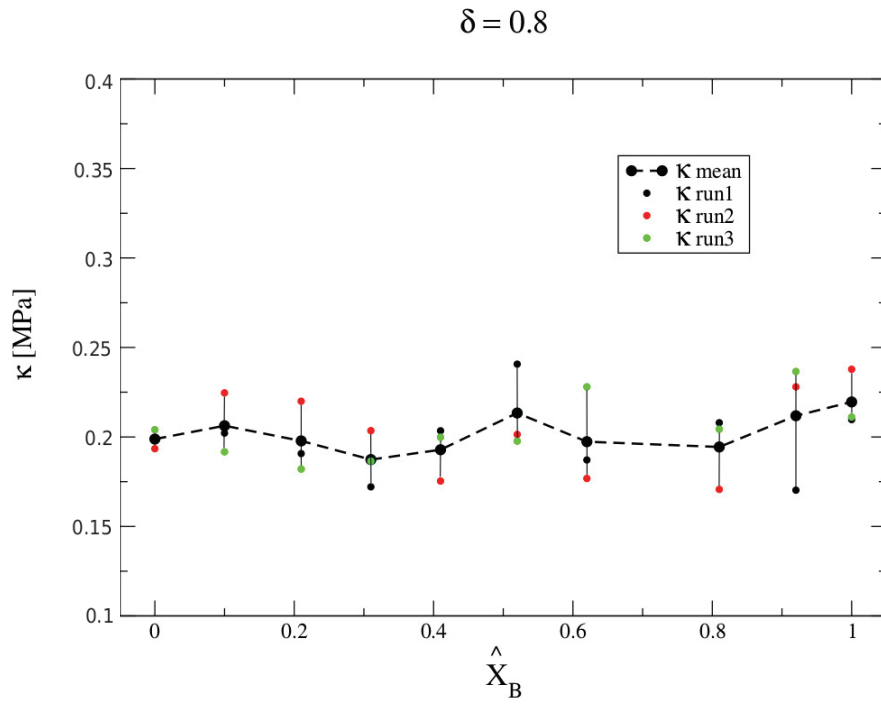


Figure 3.30: Bulk modulus determined for a granular packing with size ratio $\delta = 0.8$. The measured packing consists of PDMS particles with diameter $\varnothing_A = 5\text{mm}$ and $\varnothing_B = 4\text{mm}$. The black dashed line connects the mean values.

3.5.5 Finite Size Effects

Finite size effects have been investigated for restricted granular systems experimentally [47] and in computer simulations [48]. It is shown, that packing properties of a granular system are influenced by the container walls. For instance, spheres might arrange in the corner of a container like a regular lattice (see Fig. 3.31) which leads to a local packing fraction of $\frac{\pi}{6} \approx 0.524$.

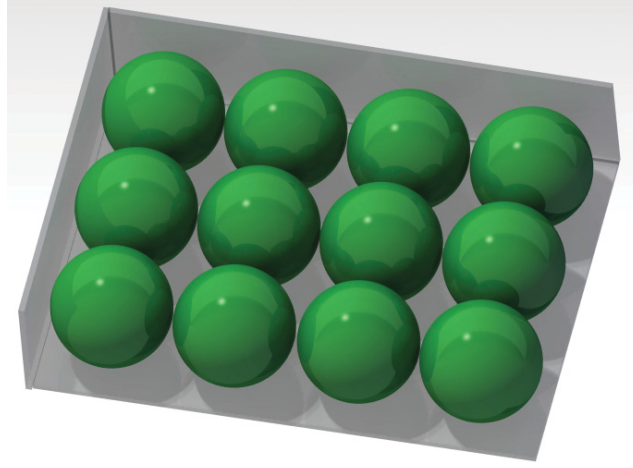


Figure 3.31: Ordered packing of spheres in a corner of a rectangular sample cell.

This packing fraction is significantly smaller than packing fractions which can be achieved in a disordered inner region of a packing. This behavior has been investigated in computer simulations for two- and three-dimensional systems [48]. K. W. Desmond et al. found a fitting law for simulated data which shows the density progression for a three dimensional packing depending on the distance from the system boundaries. For simulations they use bidisperse mixtures with size ratio $\delta = 0.71$ and mixing ratio $\hat{x}_B = 0.5$. They defined finite boundary conditions in one direction and infinite boundary conditions in the two other directions. The following formula was obtained:

$$\varphi'_{rcp} = \varphi_{rcp} - \frac{C}{S_L} \quad (3.33)$$

where φ'_{rcp} is the critical packing fraction which appears near the system boundaries while φ_{rcp} is the packing fraction which could be measured in an infinitely large system. S_L is the distance between the system boundaries and is given in multiples of sphere diameter. The constant C is determined as $C = 0.233$. Although the assumptions of equation 3.34 are not fully fulfilled by the packings investigating in the present thesis, it may still provide a good estimate for the finite size effects. Boundary errors are calculated for the granular packing consisting of PDMS spheres with size ratio $\delta = 0.18$ and mixing ratios $\hat{x}_B = 0$ and $\hat{x}_B = 1$ where the big spheres have a diameter of $\varnothing_A = 13\text{mm}$ and the small ones have $\varnothing_B = 2.4\text{mm}$. The length L of the system is chosen as 50mm (this is the size of the sample container) and the boundary errors are calculated with

$$\Delta\varphi = 4 \frac{C}{S_L} \quad (3.34)$$

where $\Delta\varphi$ is $\Delta\varphi = \varphi_{rcp} - \varphi'_{rcp}$ and the factor 4 is introduced because the present system has 6 instead of 2 container walls:

$$\hat{x}_B = \begin{cases} 0 : & \Delta\varphi = 4 * 0.233 * \frac{13mm}{50mm} \approx 0.24 \\ 1 : & \Delta\varphi = 4 * 0.233 * \frac{2.4mm}{50mm} \approx 0.04 \end{cases}$$

With an estimated packing fraction of $\varphi_{rcp} \approx 0.64$ for an infinite monodisperse system the values for the calculated packing fraction φ'_{rcp} show a deviation of $\approx 26\%$ from the measured data for the mixing ratio $\hat{x}_B = 0$. For the mixing ratio $\hat{x}_B = 1$ the deviation is $\approx 3.8\%$. The calculated and measured results are listed in Table 3.4:

size ratio δ	mixing ratio \hat{x}_B	φ'_{rcp} calculated	φ'_{rcp} measured	deviation
0.18	0	0.4	0.5416	$\approx 26\%$
	1	0.6	0.6236	$\approx 3.8\%$

Table 3.4: Calculated and measured packing fraction for a restricted granular system. The list show the calculated and measured packing fraction for a granular system of PDMS spheres consisting of particles with diameter $\varnothing_A = 13mm$ and $\varnothing_B = 2.4mm$ contained in a glass container with size $50 * 50 * 50mm$.

3.6 Outlook

For further investigation it is recommendable to improve the measurement statistics in order to get a better overview of the error deviations especially for packings where the critical jumps in the properties are observed. Furthermore it is recommendable to measure the properties of the packings for small mixing ratios $\hat{x}_B < 0.3$ with a larger sample container in order to avoid measuring finite size effects.

The data for the slope analysis provides an information of the inner stresses of a granular packing during compaction. For deriving more comparable values to other scientific results from these data, they need to be analysed regarding to for instance the pressure P which is defined as the trace of the Cauchy stress tensor. Furthermore it would be interesting to detect the individual particle contacts.

3.7 Rattler Observation via Rest Acceleration under Microgravity Conditions using Stress Birefringence

Some introductory words to microgravity research environments can be seen in section 2.11. Another parabola flight campaign (DLR-13) took place in February 2009 with an experiment using stress birefringent technique. The experimental principals are the same as described in section 3.1.1, but the experimental setup was adapted for parabolic flights with its special requirements (for full description and results see publication [23]). The setup can be seen in Fig. 3.32.

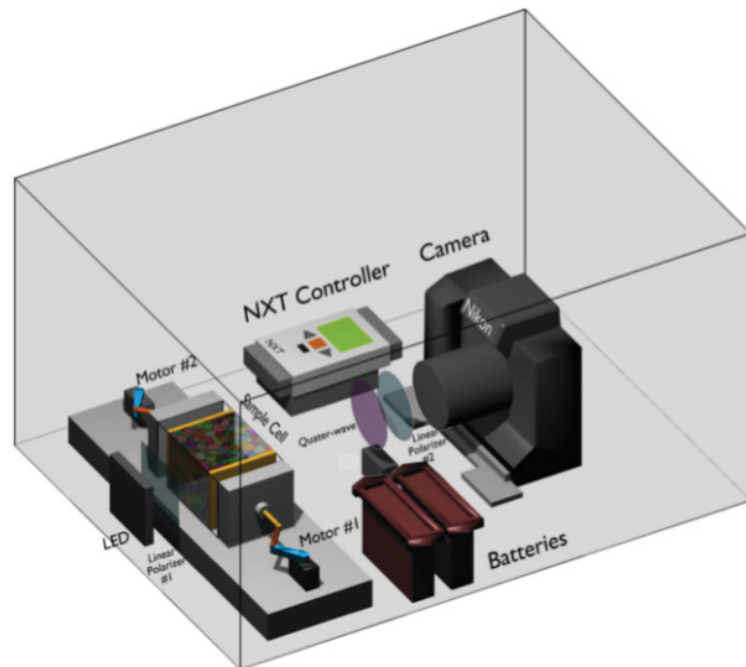


Figure 3.32: Experimental setup for the parabolic flight (DLR-13, February 2009). Stress-birefringent particles inside a sample container with cross section 5cm x 5cm and two pistons movable by servo motors #1 and #2 are illuminated by an LED panel from behind and recorded between crossed polarizers by a camera (Nikon D3). Compression and recording is operated by an NXT controller and initiated wireless via a bluetooth signal from a cell phone (Nokia 6131). The entire setup is enclosed in an aluminum box, weighs 10kg in total, and is left free-floating for distances up to 50cm inside the cabin.

The sample particles consists of gelatine and have an irregular shape with a mean diameter of around 9mm. They are surrounded by an index matching environment of pure water. Unfortunately the measured packing transition data are not analyzed so far but an observation of

a rattler in the observed system could be detected. Fig. 3.33 show an image of the dense packed granular system captured from the camera during a parabola. The packing consists of around 300 fully arrested particles with only a single particle having the space to be a rattler in a pocket formed by the arrested particles. Fig. 3.33 visualizes also the shape of the rattler particle at its initial (0, *green*) and end (1, *red*) position. The trajectory (*yellow*) is obtained by comparing a sequence of 50 pictures which were captured during a 20 second microgravity parabola. The overall travel distance of the rattler is about half its diameter. The differences in the shapes of the outline in the beginning and in the end of the trajectory are due to the rotation of the rattler in its pocket.

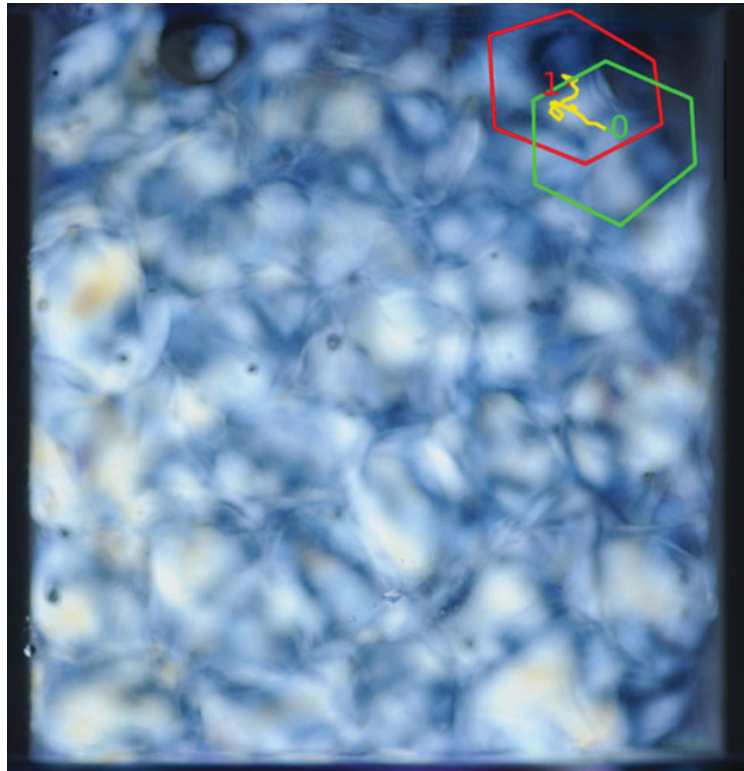


Figure 3.33: Rattler motion observed against the force-network in a granular packing visualized by stress-birefringence. The outlines indicate the rattler at its initial (0, *green*) and end (1, *red*) position. The trajectory (*yellow*) shows the distance traveled and is obtained by comparing a sequence of 50 pictures which were captured during a 20 second microgravity parabola.

Chapter 4

Sound Transmission

This chapter addresses the question how granular packings transmit sound [49, 50, 51, 52, 53]. In the present work sound transmission in bidisperse granular systems have been investigated. The measurement took place during a campaign at Ruhr-Universität Bochum where measurements for three different size ratios δ and several mixing ratios \hat{x}_B (see table 4.1) had been performed. For preparing the granular packing, lime-natron glass spheres with diameter $\varnothing = 0.2\text{mm}$, $\varnothing = 0.3\text{mm}$, $\varnothing = 0.5\text{mm}$ and $\varnothing = 1\text{mm}$ were used.

size ratio δ	$\varnothing_{particle}$ [mm]	mixing ratio \hat{x}_B
0.2	$\varnothing_A = 1$ $\varnothing_B = 0.2$	0; 0.07; 0.12; 0.19; 0.25; 0.35; 0.41; 0.42; 0.45; 0.5; 0.55; 0.65; 0.83; 0.88; 1;
0.3	$\varnothing_A = 1$ $\varnothing_B = 0.3$	0.13; 0.16; 0.23; 0.3; 0.35; 0.38; 0.4; 0.41; 0.47; 0.56; 0.68; 0.77; 1;
0.5	$\varnothing_B = 1$ $\varnothing_B = 0.5$	0.1; 0.22; 0.32; 0.4; 0.42; 0.45; 0.53; 0.64; 0.72; 1;

Table 4.1: List of performed size ratios δ and mixing ratios \hat{x}_B for the sound transition measurement in granular media.

4.1 Experimental Setup

The core element of the sound transmission setup is the triaxial compression cell with two ultrasonic transducers. One is attached to the bottom of the sample and acts as the wave generator. The other one is attached to the top of the sample and acts as the receiver. Furthermore a pressure control together with a force loading mechanism is necessary to provide triaxial compression ≥ 1 bar. The measurement chain from

the sound wave generator to the received sound signal had already been installed and calibrated. Fig. 4.1 shows the entire setup.



Figure 4.1: Sound transmission setup with the triaxial compression cell. Compression cell (1), pressure control with a force loading mechanism (2), and measurement chain with sound wave generator and receiver (3).

4.1.1 Triaxial Compression Cell

The triaxial compression cell contains and compresses the sample during the measurement procedure (see Fig. 4.2). Two shells are necessary to achieve a constant and homogenous pressure distribution. The inner shell is a cylindrical flexible latex membrane with a height of 200mm, a diameter of $\varnothing 100\text{mm}$ and a thickness 1mm (see Fig. 4.6). This inner shell contains the sample, is closed on the top and on the bottom with the ultrasonic transducer heads, and is sealed by rubber sealing rings, hose clips, and silicone grease. The outer shell is a plexiglass cylinder with a height of 350mm, a diameter of $\varnothing 250\text{mm}$, and a wall thickness of 15mm. The plexiglass cylinder is closed by aluminum plates with sealing rings and distance screws. The aluminum plates have connections for a pressure sensors, ultrasonic transducers, vacuum, and water hoses.

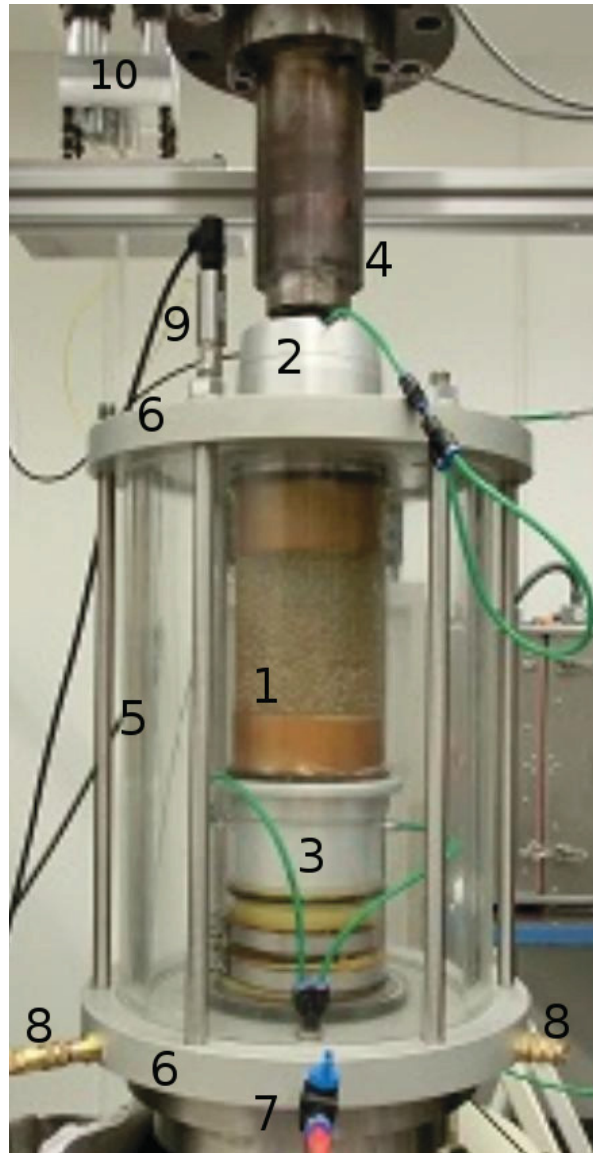


Figure 4.2: Triaxial compression cell for sound transmission measurement in granular media. The cell is not filled with water. (1) Latex membrane containing the sample (glass beads with size ratio $\delta = 0.2$ and mixing ratio $\hat{x}_B = 0.23$), (2) ultrasonic transducer receiver, (3) ultrasonic transducer wave generator, (4) Computerized Numerical Controlled (CNC) force loading mechanism, (5) plexiglass cylinder, (6) aluminum plates with (9) pressure sensors, (7) vacuum hoses, and (8) water hoses. (10) mixing apparatus as described in subsection 2.1.3

4.1.2 Force Loading Mechanism and Pressure Control

To generate a homogenous triaxial pressure distribution on the surface of the sample, the sample is loaded with a well controlled vertical force/pressure from the top. The resulting pressure at the cylindrical surface of the sample caused by the vertical force is controlled. This control mechanism is described below. For this purpose the volume between the inner shell (latex membrane) and the outer shell (plexi-glass cylinder) is filled with water. Due to the fact that water is almost incompressible, the pressure of the volume can be controlled by small changes in the water volume. These small volume changes are generated by a cylinder (see Fig. 4.3) which is driven by a stepper motor. This motor is connected to a computer via RS-232 interface. The cylinder has an inner diameter of $\varnothing 50\text{mm}$ and a stroke length of $\varnothing 250\text{mm}$. The model being used is the DNC-50-250-P-S11 from Festo[®] company. The stepper motor is a MCD EPOS 60 W from Maxon[®], which provides a torque of 54mNm . Thus, the maximum pressure of the triaxial cell can be adjusted to 2.7 bar. To load the sample in vertical direction an upgraded testing machine from the DOLI Elektonik GmbH was used. It has a mechanically driven stamp and can reach $\pm 50\text{kN}$ as the vertical force and a torque of $\pm 300\text{Nm}$. During testing only vertical force was used. The pressure sensor (see (9) in Fig. 4.2), which has a measurement range of 0-5 bars provides a feedback of the pressure status in the cell. The sensor is from the *Sensortec* company. All devices are LabVIEW controlled.



Figure 4.3: Pressure control for generating triaxial compression. (1) DNC-50-250-P-S11 cylinder from the Festo[®] company and (2) a stepper motor MCD EPOS 60 W from the Maxon[®] company

4.1.3 Measurement Chain

The measurement chain (see schematics in Fig. 4.4) starts with a frequency generator from the Tektonix[®] company. The model AFG3101

generates an amplitude of $\pm 5V$ in the pulse modus and a frequency between $1mHz$ and $50MHz$. An additional trigger signal allows to identify the start of the pulse. The initial start signal together with the received signal allows to determine the time of flight. The initially generated signal is pre-amplified by a factor of 200 via an amplifier from *Ciprian*[®] company and with this output signal the ultrasonic transducer from the company *Olympus* generates the sound pulse. The ultrasonic generator and the receiver have a central frequency of $100kHz$ and a maximum input voltage of $\pm 400V$. After passing the sample the received signal is re-amplified. The used re-amplifier is the model 5077PR from the Panametrics-NDT company and the emitted and received signal are combined in a *Wavesurfer 24Xs-A* oscilloscope from *LeCroy*[®] company. The data are saved via LAN form the oscilloscope on a computer.

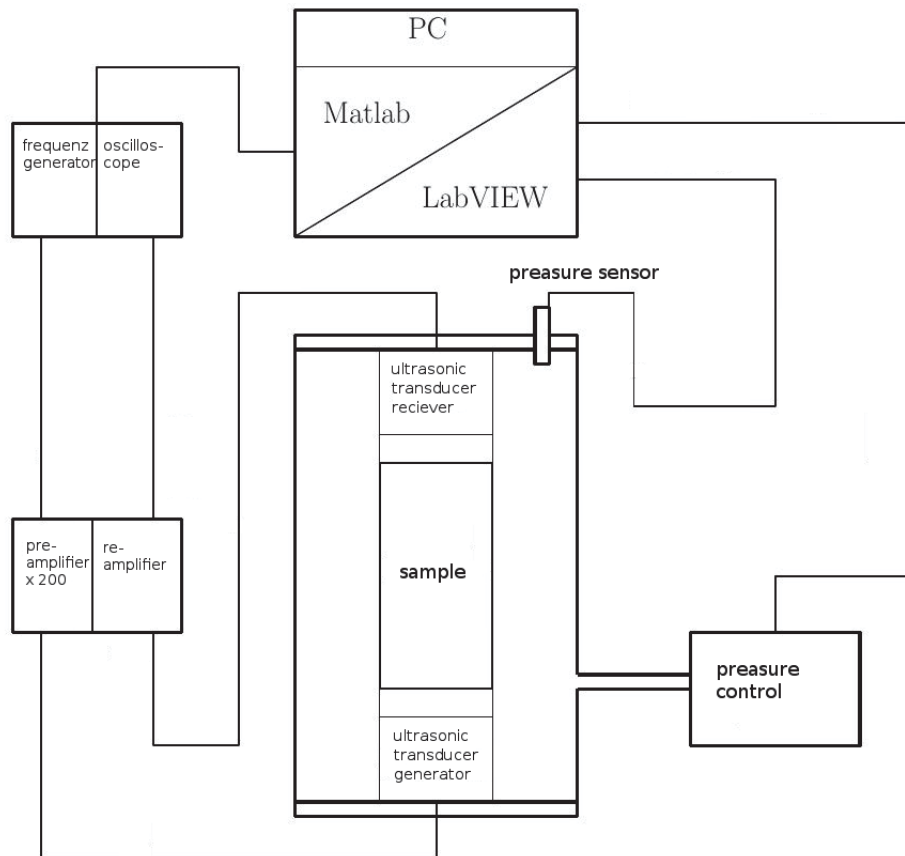


Figure 4.4: Schematics of the measurement chain for the sound transmission setup.

For more details see also the diploma thesis of Michael Krause [54].

4.1.4 Sample and Measurement Preparation

To get reproducible results, each sample needs to be prepared in a comparable and accurate way. The most challenging part of the preparation is the fixation of the granular system in the flexible latex membrane (see Fig. 4.8). The whole procedure is described in the following sections.

Preparation of the Latex Membrane

An aluminum cylinder ensures a cylindrical shape of the latex membrane (see Fig. 4.6). This cylinder consists of two halves, which are screwed together.

The latex membrane is vacuum sealed to the ultrasonic transducer generator on the bottom of the cylinder (see Fig. 4.5). After evacuation of the air between the aluminum cylinder and the latex membrane the membrane takes on the shape of the aluminum cylinder (see Fig. 4.6).

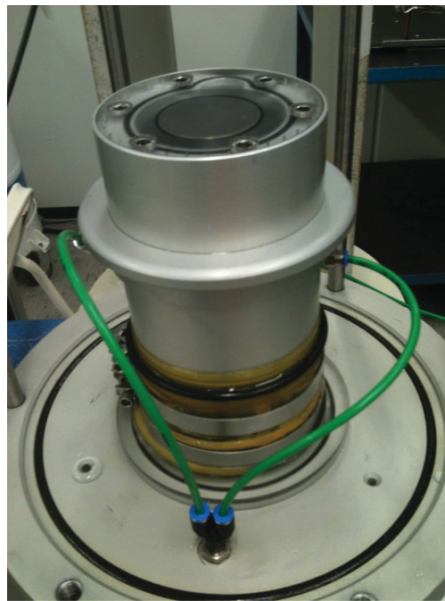


Figure 4.5: Ultrasonic transducer generator defines the bottom of the sample. Green are the hoses for the vacuum connection for later evacuation of the sample.



Figure 4.6: Picture series to visualize the latex membrane stabilization. Upper left: latex membrane with a height of 200mm, a diameter of $\varnothing 100\text{mm}$, and thickness of 1mm. Upper right: aluminum cylinder with vacuum connection in the middle. Lower left: installed and vacuum sealed latex membrane with aluminum cylinder on top of the ultrasonic transducer. Lower right: latex membrane pressed on the inner aluminum cylinder surface due to evacuation, the ultrasonic transducer is visible on the bottom.

Filling and Closing the Sample

The filling procedure for bidisperse granular mixtures has the same protocol as described in section 2.1.3 and uses the same machine (see also (10) in Fig. 4.2). After filling the sample the latex membrane has to be closed and vacuum sealed with the ultrasonic transducer receiver (see Fig. 4.7).

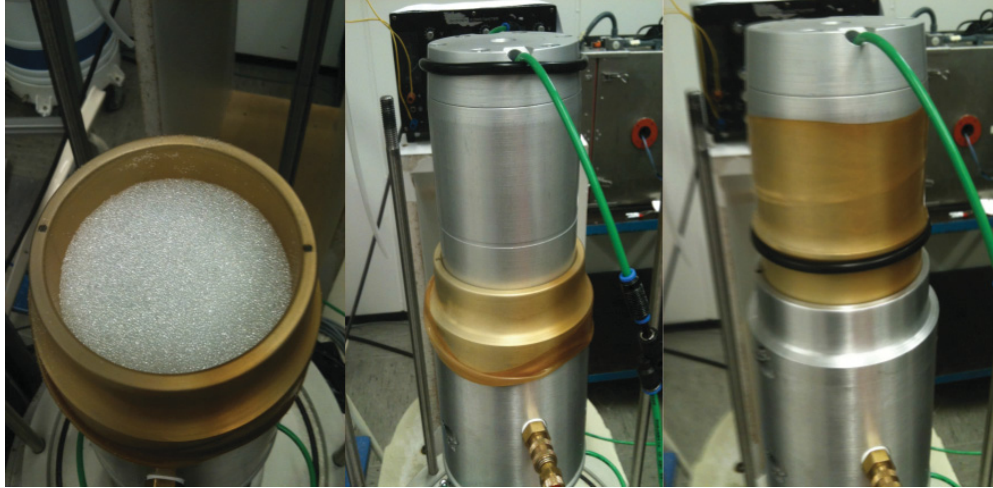


Figure 4.7: Picture series showing the closing process for the sound measurement sample cell. Left: filled latex membrane with a bidisperse mixture of glass beads ($\delta = 0.2$ and $\hat{x}_B = 0.23$). Middle: closed sample with the ultrasonic transducer receiver. Right: vacuum sealed sample with rubber sealing rings and silicone grease (not visible).

In order to stabilize the granular packing in the latex membrane the inner volume of the sample has to be evacuated. Afterwards the outer aluminum cylinder can be removed and the sample has a stable form (see Fig. 4.8).

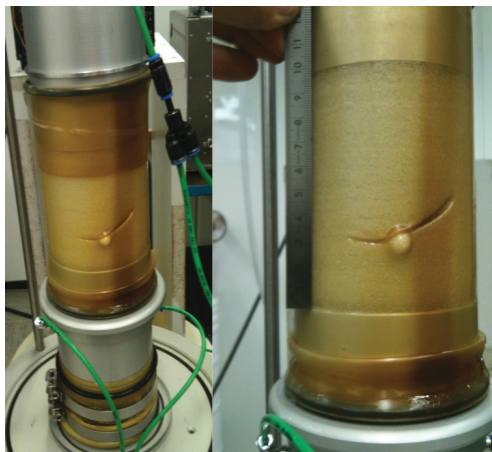


Figure 4.8: Closed sound measurement sample cell. Left: evacuated granular sample in a stable form ($\delta = 0.2$ and $\hat{x}_B = 0.23$). Right: same sample with a measured height of $\approx 95\text{mm}$. Note that the fold in the middle of the latex membrane is only on the surface and has no influence to the measurement results.

Closing the Triaxial Compression Cell

Now the triaxial compression cell can be closed by the outer plexiglas cylinder and the space between the latex membrane and the plexiglass cylinder can be filled with water (see Fig. 4.9).

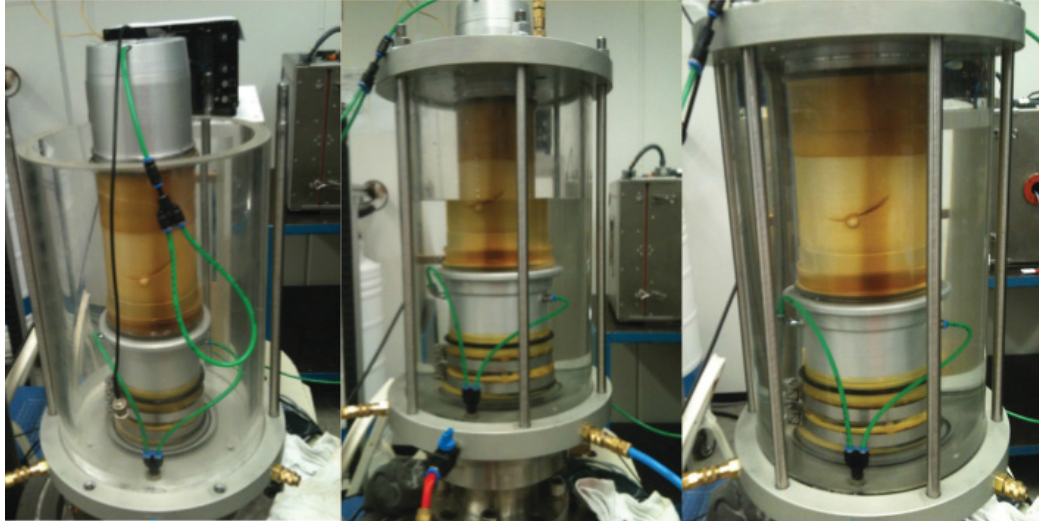


Figure 4.9: Picture series showing the water filling process. Left: installed and bottom sealed plexiglass cylinder. Middle: closed plexiglass cylinder with aluminum top plate and half filled with water. Right: fully filled triaxial compression cell.

Triaxial Compression Adjustment

First the force loading mechanism comes into contact with the ultrasonic transducer receiver (see Fig. 4.10) and we can adjust the overall force with which the sample is planned to be loaded. The force and pressure control depend on each other and have to be adjusted carefully. The decisive risk during triaxial compression is to deform the sample. For more details see [54]. After reaching a triaxial pressure of one bar the measuring procedure can start.

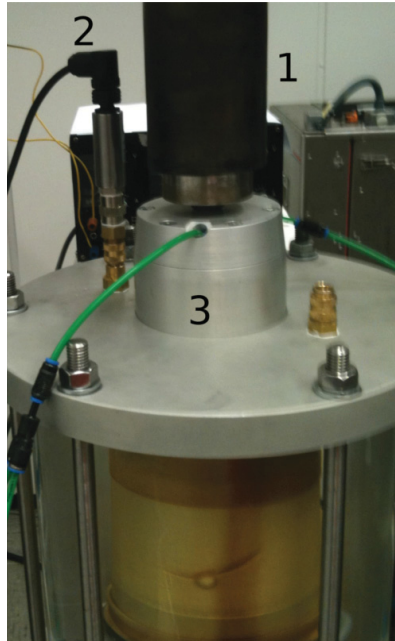


Figure 4.10: Force loading mechanism on top of the triaxial compression cell. (1) Force loading mechanism in contact with (3) the ultrasonic transducer head. A metal sphere with a diameter of $\varnothing \approx 40\text{mm}$ serves for compensating angular displacement. (2) is the pressure sensor for measuring the water pressure of the triaxial compression cell.

Measurement Parameter

The following settings are required to generate trustworthy and reproducible data and to prevent damage to the apparatus. Table 4.2 show the settings for the frequency generator.

parameter:	select:
run mode	burst mode
number of cycles	1
trigger interval	5ms
frequency	10 kHz
amplitude	$\pm 2V$
type of signal	pulse

Table 4.2: Selected parameter for the frequency generator.

The burst mode together with the number of cycles and the trigger interval control adjust the running time of the transducer so that the ul-

trasonic transducer can be effectively protected. The frequency is set to 100 kHz for all experiments. The ultrasonic transducer can work with a maximal voltage of $\pm 400V$ and the pre-amplifier intensifies the incoming signal by 200 times, hence the amplitude of the frequency generator is set to $\pm 2V$. There are several types of signals available and definable such as sinusoidal signal, Ricker signals and rectangular pulse signal. For the present experiment the rectangular pulse signal was chosen, because it generates the best Time Of Flight (TOF) measurements.

4.1.5 Time Of Flight (TOF) Measurement

The TOF for longitudinal waves have been measured in this experiment [52, 55, 51]. These waves are called P-waves and are generated and received by two ultrasonic P-wave transducers. The speed of sound is calculated by

$$c = \frac{s}{t} \quad (4.1)$$

with s = travel distance through the sample and t =TOF. The time of flight has to be corrected due to two plexiglass cover sheets on top of each ultrasonic transducer which have a thickness of 1.18 cm. With speed of sound for plexiglass $c_{plexi} = 2670 \frac{m}{s}$ (literature value) one have to subtract

$$TOF_{plexi} = \frac{2 * 0.0118m}{2670 \frac{m}{s}} = 9 \mu s \quad (4.2)$$

from the the total time of flight.

Several characteristic points are suitable for calculating TOF Fig. 4.11 show a schematic picture of a first arrival peak. The different points naturally differ for total values but deliver comparable results by using the same characteristic point for every measurement.

Three different granular systems with size ratio $\delta = 0.2$, $\delta = 0.3$ and $\delta = 0.5$ and different mixing ratios \hat{x}_B are performed experimentally (all values are listed in Table A.11 to A.13) and the measured sound transmission data show a clear first arrival peak for all experimental runs (see Fig. 4.12). In order to achieve good and comparable results the "First Maxima" is chosen for analyzing speed of sound in bidisperse granular media.

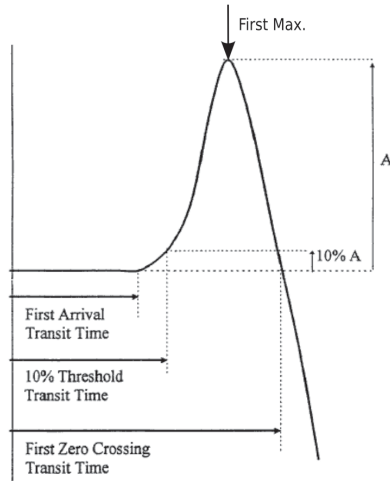


Figure 4.11: Schematic picture of a first arrival peak. Characteristic points for determine Time Of Flight (TOF): 1. First Arrival Transit Time, 2. Threshold Transit Time 10%, 3. First Maximum, 4. First Zero Crossing Transit Time

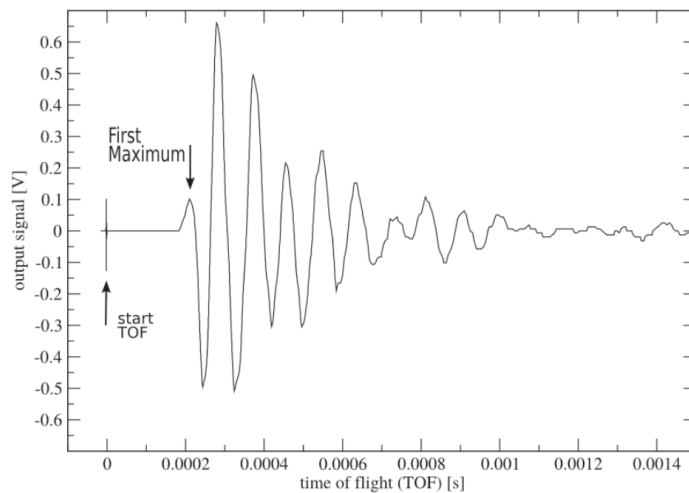


Figure 4.12: Typical sound transmission curve for a measured sound pulse in bidisperse granular media with size ration $\delta = 0.3$ and mixing ratio $\hat{x}_B = 0.13$. The packing consists of particles with $\varnothing_A = 1\text{mm}$ and $\varnothing_B = 0.3\text{mm}$. The curve show the average over 800 sound pulses measurements.

For First Maximum detection a standard peak finder tool “peakfinder.m” is used, which is written for matlab.

4.2 Sound Transmission Results

In Fig. 4.13, 4.14 and 4.15 the values for the speed of sound measurements are plotted against the mixing ratio \hat{x}_B for $\delta = 0.2$, $\delta = 0.3$ and $\delta = 0.5$ respectively.

The curve in Fig. 4.13 starts (from left to right) with a speed of sound value of $c_{packing} \approx 508 \frac{m}{s}$ at $\hat{x}_B = 0$ and until $\hat{x}_B = 0.35$ the speed of sound values are in a range of $c_{packing} = 607 \pm 15 \frac{m}{s}$. Between $\hat{x}_B = 0.35$ and $\hat{x}_B = 0.5$ a clear peak with its maximum at $\hat{x}_B = 0.42$ and $c_{packing} = 601.5 \frac{m}{s}$ is visible. From $\hat{x}_B = 0.5$ to the end of the curve the measured speed of sound levels at about the same values as measured for the mixing ratios from $\hat{x}_B = 0$ to $\hat{x}_B = 0.35$ see also table A.11).

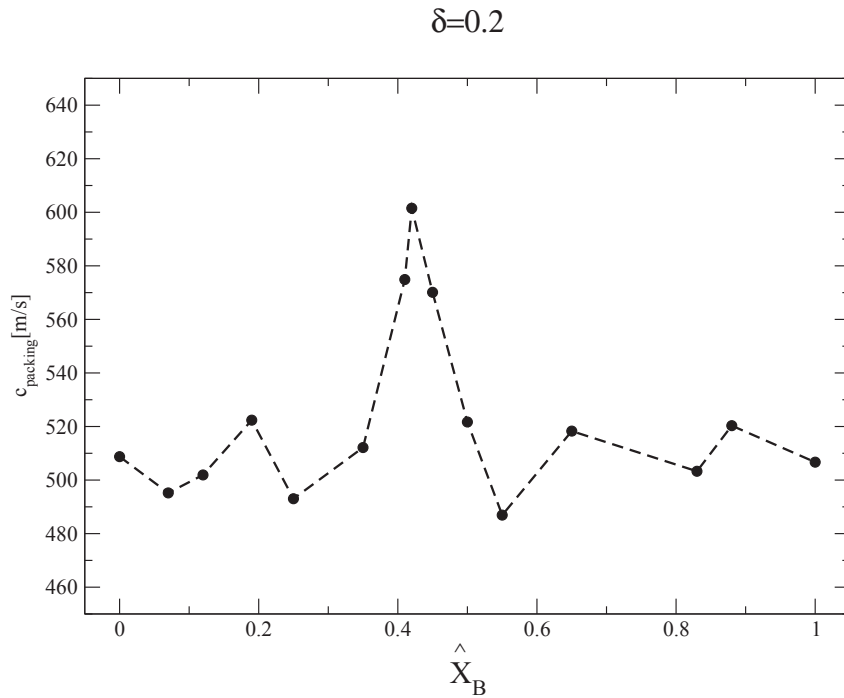


Figure 4.13: Speed of sound vs. \hat{x}_B for a granular packing with size ratio $\delta = 0.2$. The curve shows the measurement results for sound transmission speed in a bidisperse granular packing. The system consists of glass spheres with $\varnothing_A = 1\text{mm}$ and $\varnothing_B = 0.2\text{mm}$.

The curve in Fig. 4.14 increases from $c_{packing} \approx 510 \frac{m}{s}$ at $\hat{x}_B = 0$ to $c_{packing} \approx 570 \frac{m}{s}$ at $\hat{x}_B = 0.41$. The maximum appears at $\hat{x}_B = 0.47$ with $c_{packing} \approx 635 \frac{m}{s}$. From $\hat{x}_B = 0.56$ to $\hat{x}_B = 0.77$ the data show a plateau

with $c_{packing} \approx 575 \frac{m}{s}$. The last point of the curve decreases to a value of $c_{packing} \approx 520 \frac{m}{s}$. This is comparable to the measured sound transmission speed for the starting points from $\hat{x}_B = 0$ to $\hat{x}_B = 0.23$.

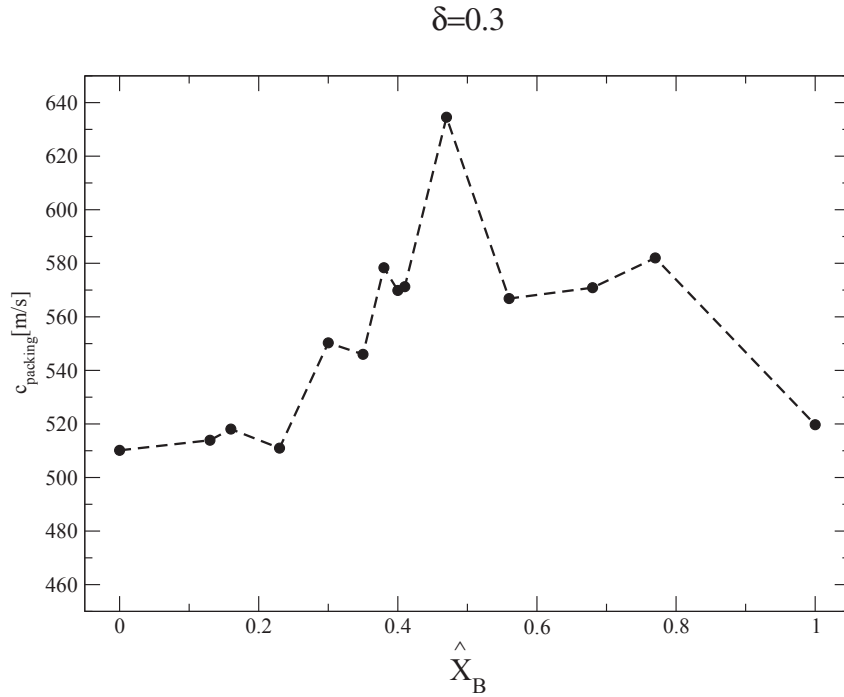


Figure 4.14: Speed of sound vs. \hat{x}_B for a granular packing with size ratio $\delta = 0.3$. The curve shows the measurement results for sound transmission speed in a bidisperse granular packing. The system consists of glass spheres with $\varnothing_A = 1\text{mm}$ and $\varnothing_B = 0.3\text{mm}$.

In Fig. 4.15 the data show no characteristic peak compared to the values shown in Fig. 4.13 and 4.14. From $\hat{x}_B = 0$ to $\hat{x}_B = 0.32$ the values increase slowly from $c_{packing} \approx 514 \frac{m}{s}$ to $c_{packing} \approx 554 \frac{m}{s}$. From $\hat{x}_B = 0.32$ to $\hat{x}_B = 0.6$ the data show a plateau with $c_{packing} \approx 550 \frac{m}{s}$ and decrease again to $c_{packing} \approx 521 \frac{m}{s}$ for $\hat{x}_B = 1$.

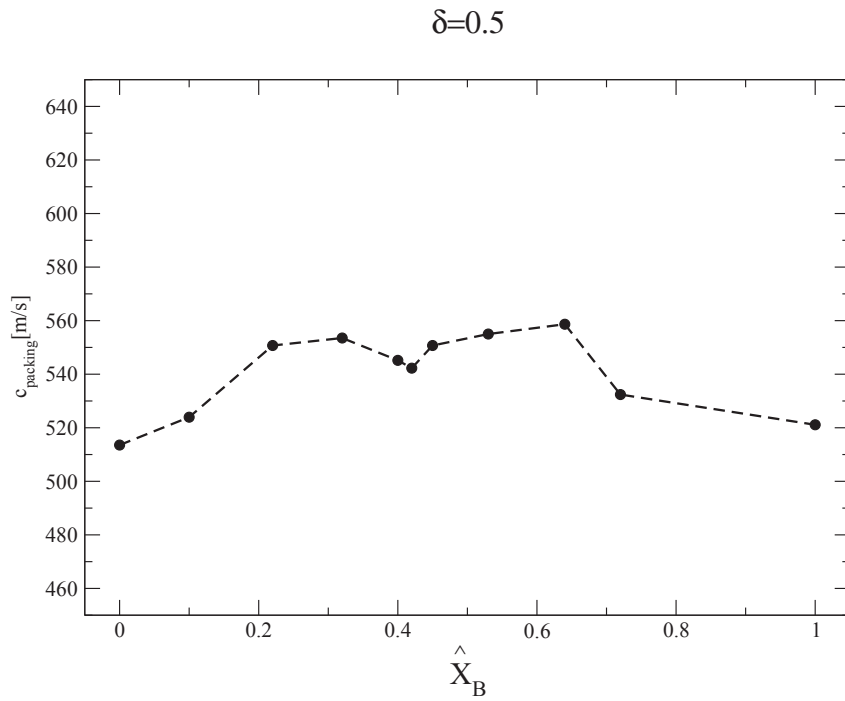


Figure 4.15: Speed of sound vs. \hat{x}_B for a granular packing with size ratio $\delta = 0.5$. The curve shows the measurement results for sound transmission speed in a bidisperse granular packing. The system consists of glass spheres with $\varnothing_A = 1\text{mm}$ and $\varnothing_B = 0.5\text{mm}$.

Chapter 5

Conclusion

An essential selection of the measurement results for glass sphere packings (see Fig. 2.18), for packings consisting of stress birefringent particles (see Fig. 3.20, 3.22, 3.24, 3.25, 3.27 and 3.29) and for sound transmission measurements (see Fig. 4.13 and 4.15) are presented in the figure on page 103. All data presented in this figure are plotted against the volume mixing ratio \hat{x}_B .

The curves in the bottom panels show the results for the density measurements of glass sphere packings with size ratio $\delta = 0.18$ (left panel) and $\delta = 0.35$ (right panel) obtained from the experiment described in section 2.6. The data for the size ratio $\delta = 0.18$ (left panel) exhibit a pronounced maximum at a mixing ratio of $\hat{x}_B \approx 0.3$. This maximum broadens for increasing size ratios which can be seen in the data for the size ratio $\delta = 0.35$ (right panel, see also Fig. 2.18.).

On top of these panels two results are shown which are based on stress birefringent measurements (see section 3.4) for packings with size ratio the $\delta = 0.18$ and $\delta = 0.4$ (see also Fig. 3.20 and 3.22). These measurements provide also information about the density of a random close packed granular system comparable to the results shown in the bottom panels. The difference is here that the obtained data are based on soft PDMS spheres (elastic modulus $E \approx 0.68$ MPa) in an liquid environment. Although friction can influence the density of granular systems [17] the measured data for size ratio $\delta = 0.35$ in the bottom panel and $\delta = 0.4$ in the panel above (right panels) show comparable results for the density values at $\hat{x}_B = 0$ and $\hat{x}_B = 1$ with $\varphi \approx 0.63$. Also comparable is the maximum density reached in both data sets with a value of $\varphi \approx 0.69$. Only the shape differs from each other. The packing of glass spheres (bottom right panel) has its maximum region between $\hat{x}_B \approx 0.25$ and $\hat{x}_B \approx 0.55$ and the packing of PDMS spheres (upper right panel) has its maximum region between $\hat{x}_B \approx 0.4$ and $\hat{x}_B \approx 0.7$. Different from the data

for the size ratios $\delta = 0.35$ and $\delta = 0.4$ the densities for the data with size ratio $\delta = 0.18$ (left bottom panel and above) show only comparable results for the densities at mixing ratios $\hat{x}_B > 0.5$ except some underestimation of the total densities for the packings with PDMS particles (upper left panel). For size ratios $\hat{x}_B < 0.5$ both data sets exhibit different evolutions. The densities for the glass sphere packing increases steeply but steady from $\hat{x}_B = 0.1$ to the maximum at $\hat{x}_B \approx 0.3$ while the densities for the PDMS spheres exhibits a jump from density $\varphi \approx 0.62$ at $\hat{x}_B = 0.4$ to $\varphi \approx 0.71$ at $\hat{x}_B = 0.5$ (note that the data points between $\hat{x}_B = 0$ and $\hat{x}_B = 0.2$ are not shown, see discussion 3.5.2). This is a surprising result because one would expect that also for concentrations $\hat{x}_B < 0.5$ both data should be comparable. One possible explanation is that in the region between $\hat{x}_B = 0$ and $\hat{x}_B = 0.5$ finite size effects dominate the packings. But K. W. Desmond et al. predicts in [48] a smooth transition from a packing influenced by finite size effects to packings which are not influenced by finite size effects which stands in contradiction to the measured data, where rather a corner than a smooth curve appears. Furthermore the data for packings with size ratio $\delta = 0.3$ consisting of PDMS particles (see Fig. 3.21 not visible in the figure on page 103) exhibits also a small jump in density at a mixing ratio of approximately 0.45. This leads to the explanation that the stress birefringent measurements are more precise and sensitive by measuring the transition from a loose to dens granular system. It also leads to the assumptions that there could be a density-density transition for close packed bidisperse granular systems, reminiscent of glass-glass transitions [56, 57, 58]. Another alternative explanation could be that the measured packings for size ratios $\delta < 0.4$ (see Fig. 3.20 and 3.21) exhibits a transition from an ordered to a disordered system. With that assumption both curves should show a clear distinction in the densities between ordered and disordered packings. Such a distinction can be interpreted in the curve for size ratio $\delta = 0.18$ where a clear jump is visible (upper left panel and Fig. 3.20). The data for packings with size ratio $\delta = 0.3$ (see Fig. 3.21) show a constantly increasing behavior between mixing ratio $\hat{x}_B = 0$ and $\hat{x}_B = 0.4$ followed by a small jump between $\hat{x}_B = 0.4$ and $\hat{x}_B = 0.45$ which stands in contradiction to the assumption.

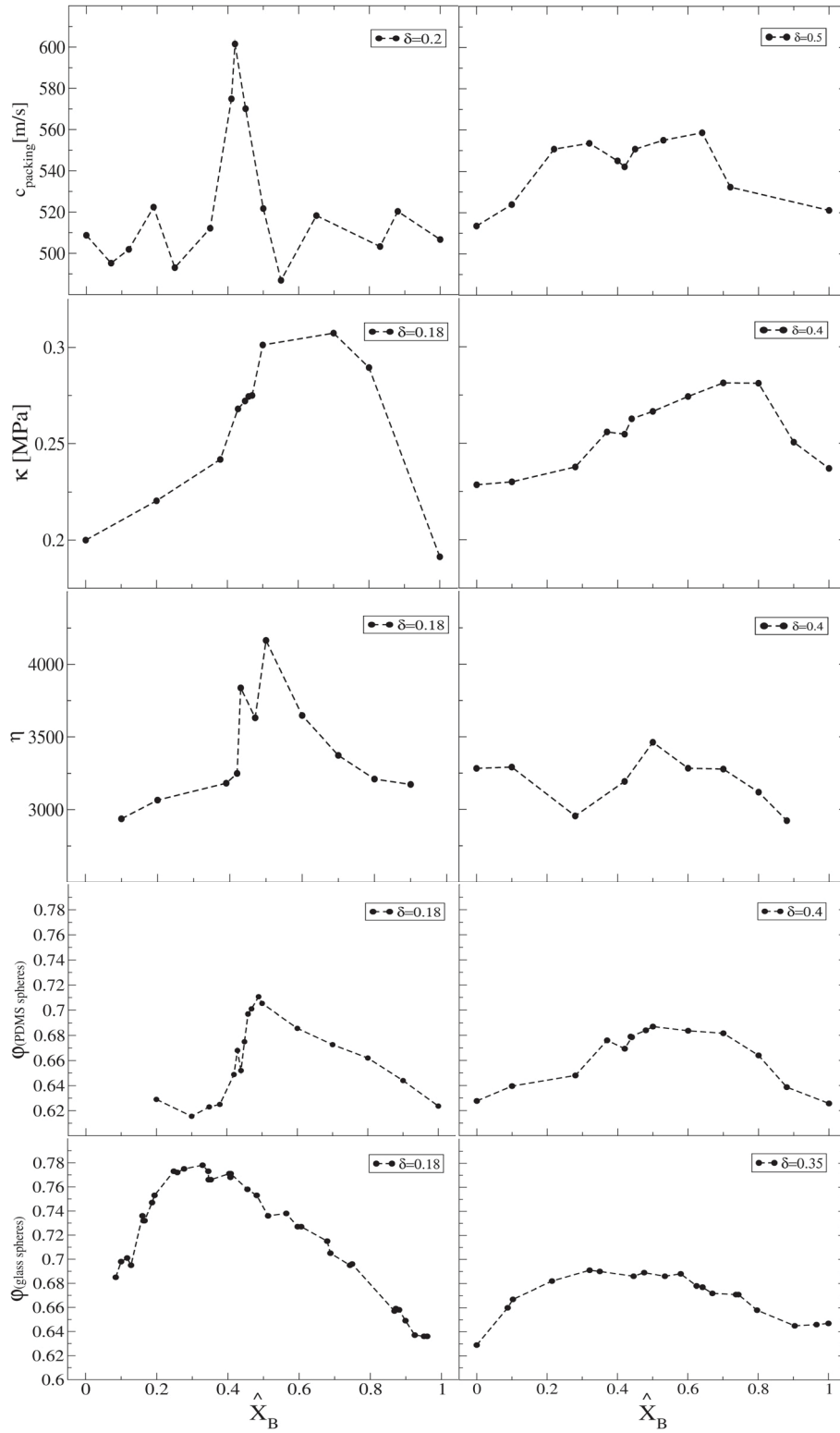
In the middle of the figure on page 103 the left and the right panel show the results for the slope η analysis (see also 3.24 and 3.25) for packings with size ratio $\delta = 0.18$ and $\delta = 0.4$, respectively. The measured packings are based on PDMS spheres and the outliers are not visible in the diagrams. These curve provide information about the inner stress states of the packing by varying the mixing ratio. The data for size ratio $\delta = 0.18$ (left panel) exhibits a pronounced maximum between $\hat{x}_B = 0.45$

and $\hat{x}_B = 0.55$. This maximum is about 30% higher than the values at both ends of the curve. In contrary to the curve for size ratio $\delta = 0.18$ the curve for size ratio $\delta = 0.4$ (right panel) show no pronounced maximum. That suggests that the inner stress states of a bidisperse granular packing depends strongly on size and mixing ratios of the system.

On top of the diagrams for the slope analysis two panels are shown which visualize the results for the bulk modulus κ analysis (see also Fig. 3.27 and 3.29). The measurements are based on packings consisting of PDMS particles with size ratios $\delta = 0.18$ and $\delta = 0.4$ (left and right panel respectively). The bulk modulus data for size ratio $\delta = 0.18$ (left panel) show a pronounced maximum region between $\hat{x}_B = 0.45$ and $\hat{x}_B = 0.8$ with a yump at $\hat{x}_B = 0.45$ (note that the data points between $\hat{x}_B = 0$ and $\hat{x}_B = 0.2$ are not shown, see discussion 3.5.2). The data for size ratio $\delta = 0.4$ (right panel) exhibits a constantly flat increasing until the maximum at $\hat{x}_B = 0.8$ is reached. The curve starts and ends at higher total values compared to the bulk modulus data for packings with size ratio $\delta = 0.18$ (left panel) and show no pronounced jump.

The top panels show the results for the sound measurements for size ratios $\delta = 0.2$ (left panel) and $\delta = 0.5$ (right panel). In the curve of the data with size ratio $\delta = 0.2$ a clear peak is visible at a mixing ratio of $\hat{x}_B \approx 0.4$ where the speed of sound jumps from $c_{packing} \approx 510[\frac{m}{s}]$ to a maximum value of $c_{packing} \approx 610[\frac{m}{s}]$. The peak vanishes in the diagram for size ratio $\delta = 0.5$ (right panel) and the range for higher speed of sound values broaden to a plateau between mixing ratio $\hat{x}_B = 0.2$ and $\hat{x}_B = 0.65$. Also the maximum speed of sound decreases to a value of $c_{packing} \approx 555[\frac{m}{s}]$.

In summary, based on all measured data in this thesis related to the mechanical properties of jammed disordered binary granular packings, it seems safe to state that for granular packings with size ratio $\delta < 0.4$ a novel transition from a loose to dense state exists which is located between mixing ratio $\hat{x}_B = 0.4$ and $\hat{x}_B = 0.5$.



Two experiments were performed on parabolic flights (DLR-13 and DLR-22) in order to get access to microgravity. The results are published in [23]. In these experiments it has been shown that stress-birefringence allows the observation of the compaction of a granular packing in microgravity. Remarkably, the conditions on parabolic flights are especially suitable to observe rattlers that are agitated by the rest-accelerations without destroying the packings. The method can identify reliably the motion of a small fraction of rattler particles among the network of particles that form the backbone of the packing. While not enough data is currently available for an elaborate analysis of rattler dynamics from 3D stress-birefringence, the results show nevertheless that microgravity experiments give access to new phenomena not observable on ground.

For the X-ray radiography data it is possible to quantify the bulk dynamics in the samples, resulting in much more reliable statistics. Using the time gradient by analyzing the difference images from the detector, a quantity $\Delta(t)$ can be obtained to characterize the motion of the particles. $\Delta(t)$ allows the distinction between agitated and arrested states. In addition, it is possible to identify a novel regime of cooling quantitatively for low rates of compaction. This is only possible in microgravity as under the dominating influence of gravity granular gases collapse quite rapidly [33]. The newly identified cooling extends over several seconds and is described reasonably well by a linear decay of $\Delta(t)$.

Chapter 6

Summary

In this thesis three independent measurement techniques are applied for investigating different properties of disordered granular packings in three dimensions. Specifically in this thesis the used techniques are X-ray radiography and tomography, stress birefringent and sound transmission. The experiments were performed on ground for bidisperse packings with a comprehensive parameter space in size δ and mixing ratio \hat{x}_B and on parabolic flights for monodisperse packings.

X-ray tomography is used to visualize bidisperse packings of glass spheres. From the obtained data the positions of the individual particles are extracted and the packing structure is analyzed by applying the pair correlation function $g(r)$ for three different size ratios $\delta = 0.35$, $\delta = 0.55$ and $\delta = 0.7$ and different mixing ratios \hat{x}_B .

For all three size ratios three clearly distinguishable peaks are observed. The heights of the peaks depends strongly on the mixing ratios of the investigated systems and give an indication of the contact probability between two spheres.

In addition a split peak with two sub peaks is found for mixing ratios close to monodisperse systems like $\hat{x}_B = 0.056$ and $\hat{x}_B = 0.937$ in the curve with size ratio $\delta = 0.7$.

For rattler detection a significant increase in $g(r)$ of $\approx 25\%$ for B-B particle contacts is found for a hard compressed sample which indicates that the rattlers loose their voids in the packing. In addition a new method is developed for detecting rattlers in a packing.

For monodisperse packings of glass spheres a novel regime of granular cooling could be observed with X-ray radiography under microgravity condition.

Stress birefringent spheres are used to visualize the inner and outer

stress of granular binary mixtures in three dimensions. In this thesis a measurement technique is developed which includes particle production, developing the experimental setup and the data analysis. The experiment is performed for packings with size ratios $\delta = 0.18$, $\delta = 0.3$, $\delta = 0.4$ and $\delta = 0.8$ and several mixing ratios. Three different packing properties are analyzed: first the transition density from loose to dense packings, second the inner stress states of the packings and third the bulk modulus of the packings. In all results it can be seen very well that there is a significant change in the packing properties by varying the size ratio δ and the mixing ratio \hat{x}_B . For size ratio $\delta < 0.4$ (except for bulk modulus $\delta = 0.3$) the data exhibits a clear visible jump whereas the values for size ratios $\delta > 0.4$ show no pronounced jump or peak. The jumps appear between $\hat{x}_B = 0.4$ and $\hat{x}_B = 0.5$ in all measurements. In addition rattler motion could be observed in a packing consisting of stress birefringent particles under microgravity condition.

Speed of sound measurements have been applied to bidisperse granular systems of glass spheres. Measurements with size ratios $\delta = 0.2$, $\delta = 0.3$, $\delta = 0.5$ and several mixing ratios \hat{x}_B were performed. The results show a significant increase in the speed of sound for packings with size ratio $\delta < 0.4$ at mixing ratios between $\hat{x}_B = 0.4$ and $\hat{x}_B = 0.5$. For packings with size ratio $\delta > 0.4$ the speed of sound values exhibits no pronounced peak.

Appendix A

A.1 Smallest Voids Between Hard Spheres

The smallest possible voids within hard spheres with a radius r is to be calculated. Assuming four hard spheres with diameter r are distributed to their closest arrangement. In such a system the spheres touch each other and have the minimum distance $2r$. The voids between the four spheres have two characteristic sizes. On the one hand the voids where a small particle with radius r_i can slip through the arrangement and on the other hand the voids where a small sphere with radius r_j touches all other spheres. These two radii r_i and r_j can be calculated as follows (see Fig. A.1).

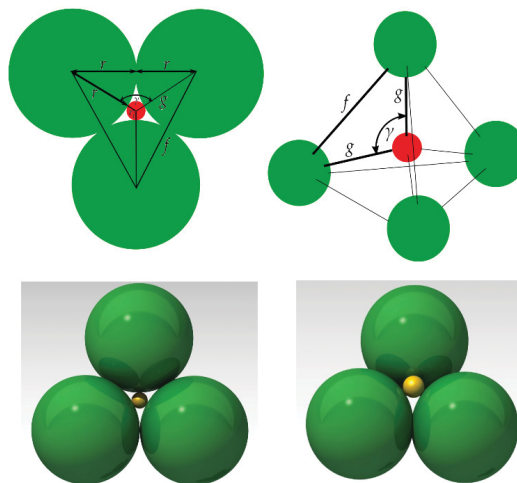


Figure A.1: The radii r_i and r_j of the largest small sphere which can fit in the two characteristic voids between an arrangement of three/four big spheres with radius r is to be calculated.

We calculate the radius r_i first: the volume of the void is used in an optimal way when the small sphere touches three of the four big spheres

(see upper left and lower left image in Fig. A.1). Hence the center of the small sphere should have the equal distance $g = r + r_i$ to the centers of the three big spheres. The center point-to-point connections of the big spheres creates an equilateral triangle with side length $f = 2r$. The length g can be calculated by the Law of Cosine:

$$f^2 = 2g^2 - 2g^2 \cos \gamma \quad (\text{A.1})$$

With $f = 2r$ and $\gamma = 120^\circ$ equation A.1 can be solved and a value $g = \frac{2}{\sqrt{3}}r$ is obtained. Now r_i can be calculated as follows:

$$r_i = g - r = r \left(\frac{2}{\sqrt{3}} - 1 \right) \approx 0.155r. \quad (\text{A.2})$$

Now we calculate r_j as follows: In an arrangement where all four big spheres with radius r touches each other, the center point-to-point connections creates a tetrahedron which is shown in Fig. A.1 (see upper right and lower right images). The edge central angle (also called tetrahedral angle) of a tetrahedron is given by $\arccos(\gamma) = \arccos(-\frac{1}{3})$. With this information r_j can be calculated with the Law of Cosine:

$$f^2 = g^2(2 - 2\cos\gamma) = \frac{8}{3}g^2 \quad (\text{A.3})$$

With $f = 2r$ equation A.3 can be solved and $g = \sqrt{\frac{3}{2}}r$ is obtained. Now r_j can be calculated:

$$r_j = g - r = r \left(\sqrt{\frac{3}{2}} - 1 \right) \approx 0.225r \quad (\text{A.4})$$

In other words: A small sphere can slip through the smallest void between three big spheres if the size ratio δ_{slip} fulfills the inequality:

$$\delta_{slip} < \frac{2}{\sqrt{3}} - 1 \approx 0.155 \quad (\text{A.5})$$

A small sphere touches all four big spheres in a tetrahedral arrangement when the size ration δ_{touch} fulfills the relation:

$$\delta_{touch} = \sqrt{\frac{3}{2}} - 1 \approx 0.225 \quad (\text{A.6})$$

A.2 Working Method for Binarisation and Position Detection of the X-ray Slice Images

A.2.1 Program Description nano

1. First slice image data are loaded in upward z-direction.

2. The histogram $h(I)$ of each image is determined ($h(I)$ means the total number of pixel h in the image with the gray value I).
3. The gray value $mx1_i$ of the global maximum $h(mx1_i)$ in the histogram is detected.
4. To find the lower maximum in the histogram two conditions have to be fulfilled
 - $h(mx2_i)$ has to be greater than the number of pixel h in the direct neighborhood of the global maximum peak at the gray value $mx1_i$.
 - The distance $d = |mx1_i - mx2_i|$ should be sufficiently large.

To fulfill both conditions in the same way $mx2_i$ is defined to maximize the expression

$$mx2_i =: |mx1_i - mx2_i| * h(mx2_i)$$

Small deviations are possible but by experience it has only negligible effects to the result.

5. Now the gray value mn_i for the minimum between the two maxima can be detected. mn_i is defined as the gray value between the two maxima at gray value $mx1_i$ and $mx2_i$ where $h(mn_i)$ has its minimum. So:

$$mn_i =: \min(I | I \in [\min(mx1_i, mx2_i) : \max(mx1_i, mx2_i)])$$

6. The slice image can now be binarized with the threshold mn_i .

This method is probably not the most comprehensive one, but it is sufficient to determine a threshold for binarization and fast. In the following it is described how the compression algorithm works:

1. A reduction factor **faktor** has to be defined.
2. The variable **sx** and **sy** has to be defined as the resolution of the slice images and **sz** as the variable for the number of slices.
3. With threshold mn_i the images are binarized and saved in an array array.
4. After all images are processed the array is reduced by the value *factor* with the IDL specific function **congrid**

The original data set is now reduced by the value *factor* from $2150 * 2150 * 2100 \approx 10^{10}$ voxel to value of $\frac{2150 * 2150 * 2100 \approx 10^{10}}{factor^3}$.

A.2.2 Program Description **dreiDposition**

dreiDposition

On the basis of the data output of the program “nano” the program **dreiDposition** is able to detect the positions of the small and big particles. **dreiDposition** outputs the position data set and a control image for each slice of the array (see Fig. 2.16).

The program works in particular as follows:

1. The data from “nano” are loaded. Furthermore the diameter of the big and small spheres da and db the thresholds $thresh_A_white$, $thresh_B_white$, $thresh_B_black$ and B_circ has to be set (described in more detail below).
2. A mask big with the diameter da (for a big sphere) is created.
3. The 3D array from **nano** is now convoluted with the mask big . This is done by a IDL routine **convol**. The result of the convolution is a new array in which every voxel has a value between zero and the total number of ones detected in the mask big within the radius da . Therefore the voxel with the highest value is the center of a big sphere and is called $avol$.
4. All voxel with a value smaller than $avol * thresh_A_white$ are set to zero. $thresh_A_white$ serves as a threshold for determining the error for calculating the maximum value in the new array.
5. Now the voxel with the highest value is saved as a center point of a big particle and all voxel within a radius of $da/2$ and the voxel itself are set to 0. This sequence is repeated until no higher values than 0 are found. Now all center points of the big particles are determined.
6. The original 3D image is loaded again and all voxel within a radius of $da/2$ around the center positions of the big spheres are set to 0. That means the big particles shall be removed and the new array is saved as $array2$.
7. The same algorithm as previous described for detecting the big particles are applied for detecting the small particles (with the associated variables).
8. After this procedure the detected particle positions are saved and outputted as a text file. For an eye based error control images are taken for each slice in the array.

A.3 Lists of Measurement Results for φ_{rcp} Densities Measured with Stress Birefringent Technique

\hat{x}_B	$\varphi_{rcp_{mean}}$	$\varphi_{rcp_{run1}}$	$\varphi_{rcp_{run2}}$	$\varphi_{rcp_{run3}}$	n_A	n_B
0	0.5416	0.552	0.538	0.534	42	0
0.1	0.5868	0.5925	0.586	0.582	42	728
0.2	0.629	0.643	0.622	0.622	39	1573
0.3	0.6155	0.621	0.61	0.615	34	2291
0.35	0.623	0.637	0.595	0.637	31	2705
0.38	0.625	0.645	0.615	0.615	30	2993
0.42	0.6488	0.647	0.647	0.6525	27	3298
0.43	0.668	0.673	0.658	0.673	27	3401
0.44	0.652	0.645	0.649	0.662	26	3427
0.45	0.675	0.71	0.663	0.652	25	3427
0.46	0.697	0.7025	0.686	0.7025	25	3516
0.47	0.701	0.715	0.715	0.673	25	3663
0.49	0.7106	0.709	0.709	0.714	24	3663
0.5	0.7053	0.703	0.71	0.703	23	3856
0.6	0.6856	0.68	0.695	0.682	18	4511
0.7	0.6726	0.675	0.668	0.675	13	5143
0.8	0.662	0.66	0.664	0.662	8	5773
0.9	0.644	0.65	0.65	0.632	3	5773
1	0.6236	0.625	0.623	0.623	0	5773

Table A.1: Data summary for the intensity measurements for size ratio $\delta = 0.18$.

\hat{x}_B	$\varphi_{rcp_{mean}}$	$\varphi_{rcp_{run1}}$	$\varphi_{rcp_{run2}}$	$\varphi_{rcp_{run3}}$	n_A	n_B
0	0.5593	0.556	0.56	0.562	42	0
0.1	0.6103	0.624	0.591	0.616	42	157
0.2	0.639	0.619	0.648	0.65	39	315
0.3	0.6856	0.667	0.7	0.69	34	472
0.35	0.694	0.712	0.692	0.678	32	581
0.38	0.7053	0.702	0.705	0.709	31	643
0.4	0.7007	0.6853	0.714	0.703	30	690
0.42	0.7165	0.72	0.713	0.7165	28	722
0.43	0.7103	0.707	0.709	0.715	28	739
0.434	0.7213	0.726	0.718	0.72	28	702
0.44	0.7183	0.723	0.715	0.717	27	739
0.45	0.7185	0.72	0.7153	0.7203	26	739
0.454	0.7186	0.7201	0.7203	0.7155	26	756
0.46	0.7202	0.7203	0.7205	0.72	26	791
0.47	0.715	0.718	0.715	0.712	25	791
0.5	0.7153	0.713	0.716	0.717	25	852
0.6	0.7136	0.7103	0.71365	0.717	19	996
0.7	0.702	0.7	0.71	0.696	15	1133
0.8	0.694	0.69	0.698	0.694	9	1252
0.9	0.661	0.668	0.658	0.659	5	1252
1	0.642	0.653	0.635	0.631	0	1252

Table A.2: Data summary for the intensity measurements for size ratio $\delta = 0.3$.

\hat{x}_B	$\varphi_{rcp_{mean}}$	$\varphi_{rcp_{run1}}$	$\varphi_{rcp_{run2}}$	$\varphi_{rcp_{run3}}$	n_A	n_B
0	0.6276	0.615	0.626	0.642	394	0
0.1	0.6395	0.64		0.639	394	582
0.28	0.648	0.663	0.65	0.631	394	1309
0.37	0.676	0.681	0.671		319	2743
0.42	0.6693	0.676	0.671	0.661	300	3066
0.437	0.6785		0.682	0.676	290	3209
0.44	0.679	0.69		0.667	290	3239
0.48	0.684	0.681	0.681	0.69	265	3496
0.5	0.687	0.69	0.681	0.69	255	3642
0.6	0.6836	0.686	0.679	0.686	206	4370
0.7	0.6816	0.683	0.683	.679	156	5088
0.8	0.664	0.671	0.675	0.646	105	5815
0.88	0.6386	0.6461	0.6314	0.6385	57	5940
1	0.6256	0.649	0.617	0.611	0	5940

Table A.3: Data summary for the intensity measurements for size ratio $\delta = 0.4$.

\hat{x}_B	$\varphi_{rcp_{mean}}$	$\varphi_{rcp_{run1}}$	$\varphi_{rcp_{run2}}$	$\varphi_{rcp_{run3}}$	n_A	n_B
0	0.6433	0.652	0.658	0.62	808	0
0.1	0.6416	0.635	0.641	0.649	723	167
0.21	0.6425	0.6457	0.638	0.644	634	339
0.31	0.648	0.65	0.642	0.65	554	498
0.41	0.6483	0.658	0.652	0.635	476	650
0.52	0.642	0.641	0.636	0.651	393	828
0.62	0.642	0.631	0.646	0.649	313	988
0.71	0.641	0.65	0.643	0.631	234	1141
0.81	0.644	0.648	0.651	0.634	154	1300
0.92	0.645	0.652	0.647	0.638	68	1473
1	0.643	0.642	0.639	0.649	0	1599

Table A.4: Data summary for the intensity measurements for size ratio $\delta = 0.8$.

A.4 Lists of Measurement Results for Slope Analysis

\hat{x}_B	$\eta_{rcp_{mean}}$	$\eta_{rcp_{run1}}$	$\eta_{rcp_{run2}}$	$\eta_{rcp_{run3}}$	n_A	n_B
0	3942.63	3865	4102.2	3860.7	42	0
0.1	2937.1	2940.3	3124.2	2746.8	42	728
0.2	3065.93	2732.9	3146.8	3318.1	39	1573
0.38	3182.53	3434	3104	3009.6	30	2993
0.42	3249.6	3060.1	3299.2	3389.5	27	3298
0.43	3837.43	4123.5	3511.1	3877.7	27	3401
0.47	3631.16	3727.7	3824	3341.8	25	3663
0.5	4164.66	3927.2	3991.4	4575.4	23	3856
0.6	3647.2	3602.7	3646.7	3692.2	18	4511
0.7	3374.36	3276.9	3432.1	3414.1	13	5143
0.8	3211.26	3374.4	2949.2	3310.2	8	5773
0.9	3173.96	3321.6	3283.1	2917.2	3	5773
1	2491.86	2495.5	2616.9	2363.2	0	5773

Table A.5: Data summary for the slope analysis for size ratio $\delta = 0.18$.

\hat{x}_B	$\varphi_{rcp_{mean}}$	$\varphi_{rcp_{run1}}$	$\varphi_{rcp_{run2}}$	$\varphi_{rcp_{run3}}$	n_A	n_B
0	3282.93	2655.7	3867.6	3550.7	394	0
0.1	3291.83	3462.3	2862.5	2826.4	394	582
0.28	2955.33	3314.3	2725.3	2826.4	394	1309
0.42	3193.26	3120.2	3273.8	3185.8	300	3066
0.5	3462.26	3149.4	3658.1	3579.3	255	3642
0.6	3283.76	3487.9	3081.3	3282.1	206	4370
0.7	3278	3255.1	3453.8	3125.1	156	5088
0.8	3119.13	3189	3530	2638.4	105	5815
0.88	2923.23	2791.1	3154.6	2824	57	5940
1	2380.13	2735.2	2082.1	2323.1	0	5940

Table A.6: Data summary for the slope analysis for size ratio $\delta = 0.4$.

A.5 Lists of Measurement Results for Bulk Modulus

\hat{x}_B	$\kappa_{mean}[Pa]$	$\kappa_{run1}[Pa]$	$\kappa_{run2}[Pa]$	$\kappa_{run3}[Pa]$	n_A	n_B
0	199964.16	172832.09	215647.92	211665.31	42	0
0.2	220415.71	154915.11	245608.3	261988.81	39	1573
0.38	241889.37	361730.4	189262.62	169765.98	30	2993
0.43	268013.43	278796.35	270885.88	254265.96	27	3401
0.45	272137.45	275872.39	288050.41	246363.67	25	3427
0.46	274491.32	285079.04	282189.59	256232.58	25	3516
0.47	275022.13	264865.05	301442.84	257299.62	25	3663
0.5	301254.93	240219.31	321153.25	342044.9	23	3856
0.7	307400.21	275072.75	329913.41	317653.25	13	5143
0.8	289505.13	324130.64	256229.03	288336.82	8	5773
1	191312.37	185112.75	194178.17	194706.81	0	5773

Table A.7: Data summary for the bulk modulus analysis for size ratio $\delta = 0.18$.

\hat{x}_B	$\kappa_{mean}[Pa]$	$\kappa_{run1}[Pa]$	$\kappa_{run2}[Pa]$	$\kappa_{run3}[Pa]$	n_A	n_B
0	235665.66	277324.98	194082.58		42	0
0.1	247129.06	281691.46	211043.83	262189.86	42	157
0.2	270255.01	203800.71	334033.11	269638.1	39	315
0.3	283756.84	261852.22	304784.64	290973.36	34	472
0.35	285963.98	261551.36	310376.6		32	581
0.38	280162.26	285602.32	274718.87		31	643
0.43	285529.76	290652.08	270525.45	291774.93	28	739
0.434	288443.2	281738.52	292983.97	290652.08	28	702
0.44	275774.38	243431.92	276550.58	307600.51	27	739
0.45	317523.67	290271.01	377295.58	284604.17	26	739
0.46	288582.04	307683.2	302857.23	254897.53	26	791
0.6	296183.36	307512.87	284956.89		19	996
0.7	252159.78	213149.31	242864.77	300061.26	15	1133
0.8	254424.3	253140.39	254428.11	255673.94	9	1252
0.9	266746.78	238781.06	313618.34	247837.53	5	1252
1	256416.96	227097.55	304495.65	236887.55	0	1252

Table A.8: Data summary for the bulk modulus analysis for size ratio $\delta = 0.3$.

\hat{x}_B	$\kappa_{mean}[Pa]$	$\kappa_{run1}[Pa]$	$\kappa_{run2}[Pa]$	$\kappa_{run3}[Pa]$	n_A	n_B
0	228476.98		219820.6	0 237253.73	394	0
0.1	230002.44	251930.09	198008.1	240017.5	394	582
0.28	237729.55	230610.75	230487.03	252360.42	394	1309
0.37	255859.82	283319.59	228279.33		319	2743
0.42	254700.19	227792.16	275909.65	260563.11	300	3066
0.44	262653.6		262341.29	262849.44	290	3239
0.5	266489.46	238394.98	281694.88	279512.82	255	3642
0.6	274210.25	301630.78	238625.79	281859.46	206	4370
0.7	281260.7	271914.59	293569.23	278271.66	156	5088
0.8	281085.79	292977.29	308590.25	239241.89	105	5815
0.9	250559.17	231888.41	272889.62	247223.68	57	5940
1	236974.3	237487.46	213226.36	259519.13	0	5940

Table A.9: Data summary for the bulk modulus analysis for size ratio $\delta = 0.4$.

\hat{x}_B	$\kappa_{mean}[Pa]$	$\kappa_{run1}[Pa]$	$\kappa_{run2}[Pa]$	$\kappa_{run3}[Pa]$	n_A	n_B
0	198842.65	198842.65	193422.29	204063.02	808	0
0.1	206290.1	202157.65	224642.47	191733.32	723	167
0.21	197790.34	190733.35	219959.42	182061.17	634	339
0.31	187376.7	172144.45	203558.23	186534.54	554	498
0.41	192889.71	203459.23	175371.1	199853.01	476	650
0.52	213401.09	240683.6	201419.15	197725.25	393	828
0.62	197386.03	187174.57	176814.11	228032.16	313	988
0.81	194395.54	207967.73	170734.25	204360.78	154	1300
0.92	211849.87	170275.22	228009.95	236577.54	68	1473
1	219589	209707.71	237810.63	211113.72	0	1599

Table A.10: Data summary for the bulk modulus analysis for size ratio $\delta = 0.8$.

A.6 Lists of Measurement Results for Sound Transmission

size ratio δ	mixing ratio \hat{x}_B	speed of sound $c_{packing} [\frac{m}{s}]$
0.2	0	508.73
	0.07	495.21
	0.12	501.9
	0.19	522.37
	0.25	493.04
	0.35	512.14
	0.41	574.89
	0.42	601.5
	0.45	570.12
	0.5	521.69
	0.55	486.9
	0.65	518.28
	0.83	503.27
	0.88	520.32
1	506.68	

Table A.11: Data summary for the speed of sound measurements for size ratio $\delta = 0.2$.

size ratio δ	mixing ratio \hat{x}_B	speed of sound $c_{packing} [\frac{m}{s}]$
0.3	0	510.13
	0.13	513.9
	0.16	518.08
	0.23	510.95
	0.3	550.27
	0.35	545.98
	0.38	578.33
	0.4	569.86
	0.41	571.25
	0.47	634.55
	0.56	566.81
	0.68	570.87
	0.77	582.01
	1	519.71

Table A.12: Data summary for the speed of sound measurements for size ratio $\delta = 0.3$.

size ratio δ	mixing ratio \hat{x}_B	speed of sound $c_{packing} [\frac{m}{s}]$
0.5	0	513.54
	0.1	523.94
	0.22	550.7
	0.32	553.52
	0.4	545.16
	0.42	542.25
	0.45	550.7
	0.53	555.01
	0.64	558.64
	0.72	532.39
	1	521.12

Table A.13: Data summary for the speed of sound measurements for size ratio $\delta = 0.5$.

A.7

Bibliography

- [1] N.V. Brilliantov and T. Pöschel, *Kinetic Theory of Granular Gases* (New York: Oxford University Press, 2004) .
- [2] Falcon, E., Wunenburger, R., Evesque, R., Fauve, R., Chabot, C., Garrabos, Y., Beysens, D.: Cluster formation in a granular medium fluidized by vibrations in low gravity. *Phys. Rev. Lett.* **83**, 440 (1999).
- [3] Bernal, J.D.: Packing of Spheres: Co-ordination of Randomly Packed Spheres. *Nature* **185**, 68 (1960).
- [4] Torquato, S., Truskett, T.M., Debenedetti, P.G.: Is Random Close Packing of Spheres Well Defined? *Phys. Rev. Lett.* **84**, 2064 (2000).
- [5] Scott, G.D., Kilgour, D.M.: The density of random close packing of spheres. *Brit. J. Appl. Phys.* **2**, 863 (1969).
- [6] A. J. Liu and S. R. Nagel, *Jamming and Rheology: Constrained Dynamics on Microscopic and Macroscopic Scales* (Taylor & Francis, New York, 2001).
- [7] Shapiro, A.P., Probst, R.F.: Random packings of spheres and fluidity limits of monodisperse and bidisperse suspensions. *Phys. Rev. Lett.* **68**, 1422 (1992).
- [8] Majmudar, S., Sperl, M., Luding, S., Behringer, R.P.: Jamming transition in granular systems. *Phys. Rev. Lett.* **98**, 058001 (2007).
- [9] Götze, W., Voignmann, T.: Effect of composition changes on the structural relaxation of a binary mixture. *Phys. Rev. E.* **67**, 021502 (2003).
- [10] Lemaignan, C.: Hard spheres simulation of the size effect in liquid and amorphous metallic alloys. *Acta Metall* **28**, 1657-1661 (1980).
- [11] Schröter, M., Ulrich, S., Kreft, J., Swift, J.B., Swinney H.L.: Mechanisms in the size segregation of a binary granular mixture. *Phys. Rev. E.* **74**, 011307 (2006).
- [12] Neudecker, M., Ulrich, S., Herminghaus, S., Schröter, M.: Jamming of frictional tetrahedra. *Phys. Rev. Lett.* **111**, 028001 (2013).

- [13] Richard, P., Philippe, P., Barbe, F., Thibault, X., Bideau, D.: Analysis by x-ray microtomography of a granular packing undergoing compaction. *Phys. Rev. E.* **68** 020301(R) (2003).
- [14] Jerkins, M., Schröter, M., Swinney, H.L., Senden, T.J., Saadatfar, M., Aste, T.: Onset of mechanical stability in random packings of frictional spheres. *Phys. Rev. Lett.* **101** 018301 (2008).
- [15] Aste, T.: Volume fluctuations and geometrical constraints in granular packs. *Phys. Rev. Lett.* **96**, 018002 (2006).
- [16] F. Natterer, *The Mathematics of Computerized Tomography* (Teubner, Stuttgart 1986).
- [17] Silbert, L.E., Ertas, D., Grest, G.S., Halsey, T.C., Levine, D.: Geometry of frictionless and frictional sphere packings. *Phys. Rev. E* **65** 031304 (2002).
- [18] Xiang, Cheng: Packing structure of a two-dimensional granular system through the jamming transition. *Soft Matter* **6**, 2931 (2010).
- [19] Silbert, L. E., Liu, A.J., Nagel, S.R.: Structural signatures of the unjamming transition at zero temperature. *Phys. Rev. E* **73** 041304 (2006).
- [20] Delaney, G. W., Matteo, T.D., Aste, T.: Combining tomographic imaging and DEM simulations to investigate the structure of experimental sphere packings. *Soft Matter* **6**, 2992-3006 (2010).
- [21] Stefan Frank-Richter, Diplomarbeit: Dichte ungeordnete Packungen in drei Dimensionen., Universität zu Köln, Mathematisch-Naturwissenschaftlichen Fakultät, Februar 2011.
- [22] Aste, T., Saadatfar, M., Sakellariou, A., Senden, T.J.: Investigating the geometrical structure of disordered sphere packings. *Physica A* **339**, 16 – 23, (2004).
- [23] Yu, P., Frank-Richter, S., Börngen, A., Sperl, M.: Monitoring Three-Dimensional Packings in Microgravity. *Granular Matter* **16** 165 (2014).
- [24] Harth, K., Kornek, U., Trittel, T., Strachauer, U., Höme, S., Will, K., Stannarius, R.: Granular gases of rod-shaped grains in microgravity. *Phys. Rev. Lett.* **110**, 144102 (2013).
- [25] Sack, A., Heckel, M., Kollmer, J.E., Zimmer, F., Pöschel, T.: 3. Energy dissipation in driven granular matter in the absence of gravity. *Phys. Rev. Lett.* **111**, 018001 (2013).
- [26] Murdoch, N., Rozitis, B., Nordstrom, K., Green, S.F., Michel, P., de Lophem, T.-L., Losert, W.: Granular convection in microgravity. *Phys. Rev. Lett.* **110**, 018307 (2013).

- [27] Murdoch, N., Rozitis, B., Green, S.F., de Lophem, T.-L., Michel, P., Losert, W.: Granular Shear Flow in Varying Gravitational Environments. *Granul. Matter* **15**, 129 (2013).
- [28] Khosropour, R., Zirinsky, J., Pak, J., Behringer, R.P.: Convection and size segregation in a Couette flow of granular material. *Phys. Rev. E* **56**, 4467 (1997).
- [29] Baxter, G.W., Behringer, R.P., Fagert, T., Johnson, G.A.: Pattern formation in flowing sand. *Phys. Rev. Lett.* **62**, 2815 (1989).
- [30] Grohse, E.W.: Analysis of gas-fluidized solid systems by x-ray absorption. *AIChE J.* **1**(3), 358–365.
- [31] Rowe, P.N., Everett, D.J.: Fluidized bed bubbles viewed by X-rays. Part 2. Transition from two- to three-dimensions of undisturbed bubbles. *Trans. I. Chem. E* **50**, 42–48 (1972).
- [32] Yates, J., Cheesman, D., Lettieri, P., Newton, D.: X-ray analysis of fluidized beds and other multiphase systems. *KONA* **20**, 133–143 (2002).
- [33] Son, R., Perez, J.A., Voth, G.A.: Experimental measurements of the collapse of a two-dimensional granular gas under gravity. *Phys. Rev. E* **78**, 041302 (2008).
- [34] M.M. Frocht *Photoelasticity* (New York: John Wiley & Sons Inc. 1941).
- [35] Wambaugh, J.F., Hartley, R.R., Behringer, R.P.: Force networks and elasticity in granular silos. *Euro. Phys. Journal E*, **32** 135-145(2010).
- [36] Majmudar, T.S., Behringer, R.P.: Contact force measurements and stress-induced anisotropy in granular materials. *Nature* **435** 1079-1082 (2005).
- [37] Liu, C., Nagel, S.R., Schechter, D.A., Coppersmith, S.N., Majumdar, S., Narayan, O., Witten, T.A.: Force fluctuations in bead packs. *Science* **269**, 513–515 (1995).
- [38] Zhang, J., Majmudar, T.S., Sperl, M., Behringer, R.P.: Jamming for a 2D granular material. *Soft Matter* **6**, 2982 (2010).
- [39] Wood, D., Lesniewska, D.: Stresses in granular materials. *Granul. Matter* **13** 395-415 (2011).
- [40] Hiramatsu, Y., Oka, Y.: Determination of the tensile strength of rock by a compression test of an irregular test piece. *Int.J. Rock Mech. Min. Sci.* Vol.3, 89-99 (1966).
- [41] H. Aben *Integrated Photoelasticity* (McGraw-Hill Inc., 1979).
- [42] Frank-Richter, S., Sperl, M., Yu.P: Verfahren zur Herstellung sphärischer, spannungsdoppelbrechender Teilchen. German patent, Application number DE102011014084A1 A1.

- [43] T. Iida and R. Guthrie, *The Physical Properties of Liquid Metals* (New York: Oxford University Press, 1988).
- [44] J. Crank, *The Mathematics of Diffusion* 2nd edn (New York: Oxford University Press, 1975).
- [45] W.M. Haynes, *CRC Handbook of Chemistry and Physics* 94th edn (Boca Raton: CRC Press, 2013-2014).
- [46] R. C. Gonzalez and R. E. Woods *Digital Image Processing* 2nd edn (Prentice-Hall, New Jersey, 2002).
- [47] Scott, G.D., Kilgour, D.M.: The density of random close packing of spheres. *Brit. J. Appl. Phys., Ser2*, vol2, 863 (1969).
- [48] Desmond, K.W., Week, E.R.: Random Close Packing of Disks and Spheres in Confined Geometries. *Phys. Rev. E* **80** 051305 (2009).
- [49] Horlück, S., van Hecke, M., Dimon P.: Shock waves in two-dimensional granular flow: Effects of rough walls and polydispersity. *Phys. Rev. E* **67** 021304 (2003).
- [50] Gomez, L.R., Turner, A. M., van Hecke, M., Vitelli, V.: Shocks near Jamming. *Phys. Rev. Lett.* **108** 058001 (2012).
- [51] Agnolin, I., Roux, J.N., Massaad, P., Jia, X., Milles P.: Sound wave velocities in dry and lubricated granular packings: numerical simulations and experiments. *Powders and Grains* 313-317 (2005).
- [52] Jia, X., Caroli, C., Velicky, B.: Ultrasound Propagation in Externally Stressed Granular Media. *Phys. Rev. Lett.* **82** (1999).
- [53] Owens, E.T., Daniels, K. E.: Sound propagation and force chains in granular materials. *EPL*, **94** 54005 (2011).
- [54] Krause M., Diplomarbeit: Experimentelle Untersuchung von Ultraschall in mono- und bidispersen granularen Medien unter triaxialer Belastung. Ruhr-Universität Bochum, Lehrstuhl für Kontinuumsmechanik, 4. September 2013.
- [55] Somfai, E., Roux, J., Snoeijer, J.H., van Hecke, M., van Saarloos, W.: Elastic wave propagation in confined granular systems. *Phys. Rev. E* **72** 021301 (2005).
- [56] Dawson, F., Fof, G., Fuchs, M., Götze, W., Sciortino, F., Sperl, M., Tartaglia, P., Voigtmann, Th., Zaccarelli.: Higher-order glass-transition singularities in colloidal systems with attractive interactions. *Phys. Rev. E* **63** 011401 (2000).
- [57] Götze, W., Sperl, M.: Higher-order glass-transition singularities in systems with short-ranged attractive potentials. *Condens. Matter* **15**, 869-879 (2003).

- [58] Voigtmann, T.: Multiple glasses in asymmetric binary hard spheres. *EPL*, **96** 36006 (2011).
- [59] O'Hern, C.S., Silbert, L.E., Liu, A.J., Nagel, S.R.: Jamming at zero temperature and zero applied stress: The epitome of disorder. *Phys. Rev. E*. **68**, 011306 (2003).

Acknowledgement

I thank Professor Stefan Egelhaaf and Professor Jürgen Horbach for supervising my thesis.

I want to thank Doctor Matthias Sperl for guiding me through my thesis and for many interesting scientific discussions.

Doctor Peidong Yu and Doctor Elmar Stärk helped me with many technical problems.

I thank Prof. Dr. Ing. Holger Steeb from “Lehrstuhl für Kontinuumsmechanik” at Ruhr-Universität Bochum who provided me the experimental setup for sound measurements. I also want to thank Dipl. Ing. Michael Krause who helped me with technical details during measurements at Ruhr-Universität Bochum.

Melissa Lückcrath helped me with producing the required PDMS spheres for the granular stress birefringent measurements and Clara Mergner who helped me perform granular stress birefringent measurements.

Finally I want to thank my family Regina and Flynn Richter for their unconditional love and also my parents who taught me to be curious and to question things.

Erklärung

Hiermit erkläre ich, dass ich die vorliegende Dissertation selbstständig verfasst habe. Dabei habe ich keine anderen als die angegebenen Quellen und Hilfsmittel benutzt, Zitate wurden kenntlich gemacht.

Köln, den 15. Mai 2014

